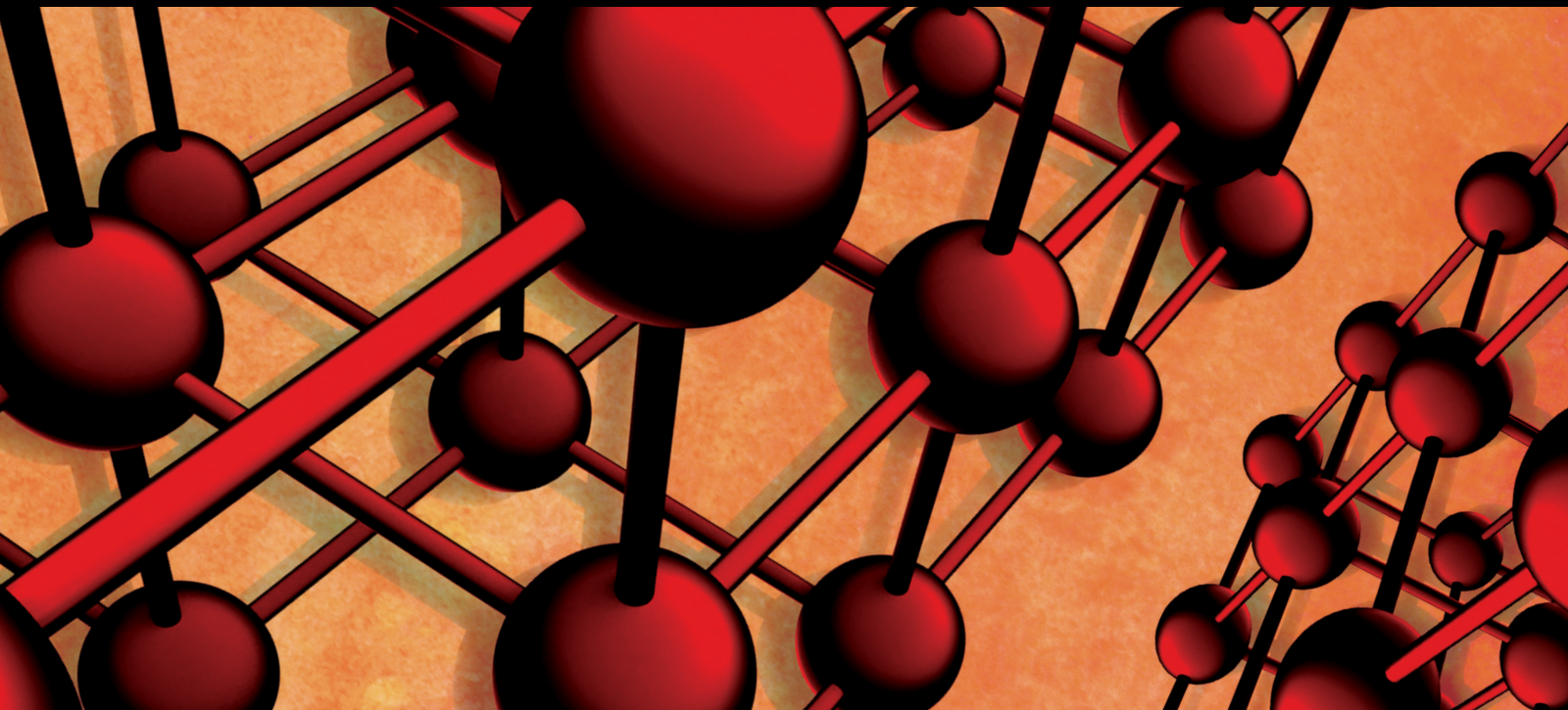


Advances in Smart Materials and Applications

Guest Editors: Kuan Yew Cheong, Kean Aw, Khasan S. Karimov, Feng Zhao,
Mohammad Mahroof-Tahir, and Rupert Schreiner





Advances in Smart Materials and Applications

Advances in Materials Science and Engineering

Advances in Smart Materials and Applications

Guest Editors: Kuan Yew Cheong, Kean Aw,
Khasan S. Karimov, Feng Zhao, Mohammad Mahroof-Tahir,
and Rupert Schreiner



Copyright © 2014 Hindawi Publishing Corporation. All rights reserved.

This is a special issue published in “Advances in Materials Science and Engineering.” All articles are open access articles distributed under the Creative Commons Attribution License, which permits unrestricted use, distribution, and reproduction in any medium, provided the original work is properly cited.

Editorial Board

K. G. Anthymidis, Greece
Robert S. Averbach, USA
Amit Bandyopadhyay, USA
Zoe Barber, UK
Yucel Birol, Turkey
Susmita Bose, USA
Steve Bull, UK
Peter Chang, Canada
Daolun Chen, Canada
Manish U. Chhowalla, USA
S. Chinnappanadar, India
Jie Dai, Singapore
Chapal K. Das, India
J. Paulo Davim, Portugal
Seshu B. Desu, USA
Yong Ding, USA
Wei Feng, China
Sergi Gallego, Spain
Lian Gao, China
Hiroki Habazaki, Japan
Richard Hennig, USA
Dachamir Hotza, Brazil
Chun-Hway Hsueh, Taiwan
Shyh-Chin Huang, Taiwan
Rui Huang, USA
Wei Huang, China
Baibiao Huang, China
Jacques Huot, Canada
Jae-Ho Kim, Korea
Jaehwan Kim, Korea
Sridhar Komarneni, USA
Hongchao Kou, China
Prashant Kumta, USA
Jui-Yang Lai, Taiwan
Pavel Lejcek, Czech Republic

Markku Leskela, Finland
Bin Li, China
Feng Li, China
Ying Li, USA
Hai Lin, China
Yuanhua Lin, China
Zhimin Liu, China
Ying Liu, USA
Yuan Liu, China
Gang Liu, China
Tao Liu, China
Jun Liu, China
Meilin Liu, Georgia
Wei Liu, France
Yunqi Liu, China
Maria A. Loi, The Netherlands
Hai Lu, China
Peter Majewski, Australia
Shuichi Miyazaki, Japan
Paul Munroe, Australia
Ali Nazari, Iran
Luigi Nicolais, Italy
Tsutomu Ohzuku, Japan
Xiaoqing Pan, USA
Ganapathiraman Ramanath, USA
Raju V. Ramanujan, Singapore
Manijeh Razeghi, USA
Mohd Sapuan Salit, Malaysia
Jainagesh A. Sekhar, USA
Jiangbo Sha, China
Liyuan Sheng, China
You Song, China
Aloysius Soon, Korea
Charles C. Sorrell, Australia
Steven L. Suib, USA

Sam-Shajing Sun, USA
Weihua Tang, China
Somchai Thongtem, Thailand
Achim Trampert, Germany
Vladimir Tsukruk, USA
Krystyn Van Vliet, USA
Rui Vilar, Portugal
Min Wang, China
Hao Wang, China
Qiang Wang, China
Rui Wang, China
Rong Wang, USA
Lu Wei, China
Jrg M K Wiezorek, USA
Wei Wu, USA
Gongnan Xie, China
Aiguo Xu, China
Hemmige S. Yathirajan, India
Jianqiao Ye, UK
Wenbin Yi, China
Jinghuai Zhang, China
Jing Zhang, China
Li Zhang, China
Tao Zhang, China
Bin Zhang, China
Jian Zhang, Singapore
Jun Zhang, China
Yufeng Zhang, China
Kai Zhang, China
Kai Zhang, China
Rui Zhang, China
Ming-Xing Zhang, Australia
Wei Zhou, China

Contents

Advances in Smart Materials and Applications, Kuan Yew Cheong, Kean Aw, Khasan S. Karimov, Feng Zhao, Mohammad Mahroof-Tahir, and Rupert Schreiner
Volume 2014, Article ID 517342, 1 page

Improvement of Homogeneity and Aspect Ratio of Silicon Tips for Field Emission by Reactive-Ion Etching, Robert Damian Lawrowski, Christian Prommesberger, Christoph Langer, Florian Dams, and Rupert Schreiner
Volume 2014, Article ID 948708, 6 pages

Effect of Laser Welding Parameters on Formation of NiTi Shape Memory Alloy Welds, Wei Wang, Xiaohong Yang, Hongguang Li, Fuzhong Cong, and Yongbing Liu
Volume 2014, Article ID 494851, 8 pages

NiTi Intermetallic Surface Coatings by Laser Metal Deposition for Improving Wear Properties of Ti-6Al-4V Substrates, Mokgadi Nomsa Mokgalaka, Sisa Lesley Pityana, Patricia Abimbola Idowu Popoola, and Tebogo Mathebula
Volume 2014, Article ID 363917, 8 pages

Influence of Ultrafine Natural Steatite Powder on Setting Time and Strength Development of Cement, K. Sudalaimani and M. Shanmugasundaram
Volume 2014, Article ID 532746, 6 pages

Structure and Physical Properties of PZT-PMnN-PSN Ceramics Near the Morphological Phase Boundary, Nguyen Dinh Tung Luan, Le Dai Vuong, Truong Van Chuong, and Nguyen Truong Tho
Volume 2014, Article ID 821404, 8 pages

Nonlinear-Electronic Transport in Fe₂O₃ Thin-Films Grown from Grain-Oriented Iron Foils, Roberto Baca Arroyo
Volume 2013, Article ID 987572, 8 pages

Application of Macrofiber Composite for Smart Transducer of Lamb Wave Inspection, Gang Ren and Kyung-Young Jhang
Volume 2013, Article ID 281575, 5 pages

Effect of Magnesium Sulphate on Self-Compacting Concrete Containing Supplementary Cementitious Materials, Aiad Hassan, Hilmi Bin Mahmud, Mohd. Zamin Jumaat, Belal ALsubari, and Aziz Abdulla
Volume 2013, Article ID 232371, 8 pages

Electromechanical Characterization and Locomotion Control of IPMC BioMicroRobot, Martin J.-D. Otis
Volume 2013, Article ID 683041, 17 pages

Editorial

Advances in Smart Materials and Applications

**Kuan Yew Cheong,¹ Kean Aw,² Khasan S. Karimov,³ Feng Zhao,⁴
Mohammad Mahroof-Tahir,⁵ and Rupert Schreiner⁶**

¹ School of Materials & Mineral Resources Engineering, Universiti Sains Malaysia, Malaysia

² Department of Mechanical Engineering, University of Auckland, New Zealand

³ Faculty of Electronic Engineering of GIK Institute, Pakistan

⁴ Department of Electrical Engineering, Washington State University, Vancouver, WA 98686, USA

⁵ Department of Chemistry and Earth Sciences, Qatar University, Qatar

⁶ Faculty of General Studies & Microsystems, Regensburg University of Applied Sciences, Germany

Correspondence should be addressed to Kuan Yew Cheong; srcheong@usm.my

Received 1 April 2014; Accepted 1 April 2014; Published 15 April 2014

Copyright © 2014 Kuan Yew Cheong et al. This is an open access article distributed under the Creative Commons Attribution License, which permits unrestricted use, distribution, and reproduction in any medium, provided the original work is properly cited.

This is one of a series of special issues published in *Advances in Materials Science and Engineering*, focusing on the latest advances of smart materials and their applications.

Evolution of engineering materials is strongly depending on the growing transformation of complexity in engineering products. New materials being designed are required to provide specific properties and demonstrate certain functional characteristics by manipulating their dimension, chemistry, and structure through various advanced technologies. Therefore, “smartness” of a material has become the topic of interest. Properties of smart materials may change accordingly to the applied external stimuli.

Under the direction of the editorial team, we showcase advances of organic and inorganic based smart materials and their applications in areas of specific interest such as energy, environment, and health. A total of 9 articles are published in this special issue. Six articles are focused on production, synthesis, and optimization of smart materials; and the remaining are dedicated to application of smart materials.

Acknowledgments

We would like to express our sincere thanks to all the contributing authors for sharing their research outputs and time, thus enabling the successful accomplishment of this issue.

*Kuan Yew Cheong
Kean Aw*

*Khasan S. Karimov
Feng Zhao
Mohammad Mahroof-Tahir
Rupert Schreiner*

Research Article

Improvement of Homogeneity and Aspect Ratio of Silicon Tips for Field Emission by Reactive-Ion Etching

Robert Damian Lawrowski, Christian Prommesberger, Christoph Langer, Florian Dams, and Rupert Schreiner

Faculty of General Sciences and Microsystems Technology, OTH Regensburg, 93053 Regensburg, Bavaria, Germany

Correspondence should be addressed to Robert Damian Lawrowski; robert.lawrowski@oth-regensburg.de

Received 16 February 2014; Accepted 9 March 2014; Published 6 April 2014

Academic Editor: Feng Zhao

Copyright © 2014 Robert Damian Lawrowski et al. This is an open access article distributed under the Creative Commons Attribution License, which permits unrestricted use, distribution, and reproduction in any medium, provided the original work is properly cited.

The homogeneity of emitters is very important for the performance of field emission (FE) devices. Reactive-ion etching (RIE) and oxidation have significant influences on the geometry of silicon tips. The RIE influences mainly the anisotropy of the emitters. Pressure has a strong impact on the anisotropic factor. Reducing the pressure results in a higher anisotropy, but the etch rate is also lower. A longer time of etching compensates this effect. Furthermore an improvement of homogeneity was observed. The impact of uprating is quite low for the anisotropic factor, but significant for the homogeneity. At low power the height and undercut of the emitters are more constant over the whole wafer. The oxidation itself is very homogeneous and has no observable effect on further variation of the homogeneity. This modified fabrication process allows solving the problem of inhomogeneity of previous field emission arrays.

1. Introduction

In vacuum microelectronic devices the field emission (FE) electron sources have advantages compared to classical thermionic cathodes. They offer no dissipation of energy in the medium (vacuum) and high radiation tolerance and work with high operation frequency [1]. The electron sources could be used in sensor systems, miniaturized microwave amplifier tubes, cathodes in electron optic systems (e.g., scanning electron microscope (SEM), scanning tunneling microscope (STM), transmission electron microscopy (TEM)), and high power THz sources as well as compact and fast-switching X-ray sources [2]. The cathode of the electron source is the most important and critical component of such devices. Small variation in emitter geometry leads to an inhomogeneity of emission. The field emission characteristics depend especially on the width of the potential barrier at the electrically conductive surface, which the electrons must tunnel through [3]. High electric fields reduce the width of this barrier (Figure 1). Nanostructures allow delivering these required fields microscopically, due to the locally enhanced field at the tip of the emitter. The field enhancement factor β

(1) which is defined by the ratio of microscopic E_{micro} to macroscopic field E_{macro} describes this relation [4]. Therefore, lower macroscopic field is necessary for tunneling:

$$\beta = \frac{E_{\text{micro}}}{E_{\text{macro}}} \approx \frac{h}{r}. \quad (1)$$

A possible approximation for β is the ratio of height h of the emitter to the radius r of the tip. Consequently, fluctuations in height and tip radius vary strongly the β -factor. Further enhanced fabrication techniques are required to replace typical cathodes in actual applications and allow novel vacuum devices.

By investigation of the influence of RIE parameters (pressure and power) on the geometry and aspect ratio of silicon emitter a chance of homogeneity can be observed.

2. Materials and Methods

2.1. Fabrication Process. Isotropic wet or dry and anisotropic dry etching are usual fabrication techniques for silicon (Si) microstructures. For reproducible emitters with high β -factor

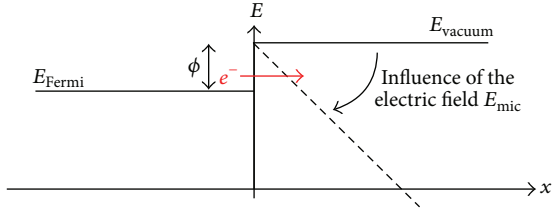


FIGURE 1: Influence of an enhanced electric field E_{micro} on the surface barrier and the tunneling of electrons.

and current carrying capacity, we use an anisotropic dry etching followed by a wet thermal oxidation [5] (Figure 2).

As bulk material 100 mm p-type silicon wafers with (100) orientation, boron doping, and a resistivity of 3.7–4.2 Ωcm are used. P-doped Si-FE-cathodes show FE-current saturation, which leads to very good current stabilization [6]. For masking a wet thermal oxide of 700 nm is grown on the substrate at 1000°C (Figure 2(a)). The position of the tips is defined by a photolithographic transfer of disks with a 3 μm diameter and triangular pitch of 20 μm into a photoresist (AZ5214) (Figure 2(b)). Anisotropic reactive-ion etching in an Oxford Plasmalab 80Plus transfers this adjustment to the SiO_2 layer (Figure 2(c)). It uses CHF_3 and O_2 as process gases. To achieve the requested shape of the emitter another RIE process step is necessary. A mixture of SF_6 and O_2 etches bulk Si with the SiO_2 discs as mask (Figure 2(d)). The anisotropy and so the geometry can be adjusted by the gas flows, chamber pressure, and RF power [7]. The remaining Si is oxidized thermally at 940°C for the final sharpening of the emitters (Figure 2(e)). The entire SiO_2 is removed in the last step by wet chemical etching with a HF mixture (BOE 7:1) (Figure 2(f)).

To get significant investigation on the homogeneity each of the twelve chips on a wafer contains six arrays with a different number of tips (1, 7, 91, 271, 547, and 1141).

2.2. Measurement Techniques and Experimental Design. For the investigation of the influence of individual fabrication steps on the emitter, after each process step, some selected tips were observed by a SEM (JEOL 6510) (Figure 3). For a significant conclusion of the homogeneity eight tips on each array were scanned on every corner of the hexagonal layout and two in the middle of the array (Figure 4(a)). Two of three chips on each quarter of a wafer were investigated (Figure 4(b)).

The undercut r_{\parallel} of the SiO_2 -mask, due to the RIE step, was determined by SEM. The etch depth r_{\perp} was measured with a KLA Tencor P16 profilometer. By this way, the anisotropic factor (2), which impacts the homogeneity and geometry of the emitters, was determined for diverse powers and pressures at the RIE step:

$$f = 1 - \frac{r_{\parallel}}{r_{\perp}}. \quad (2)$$

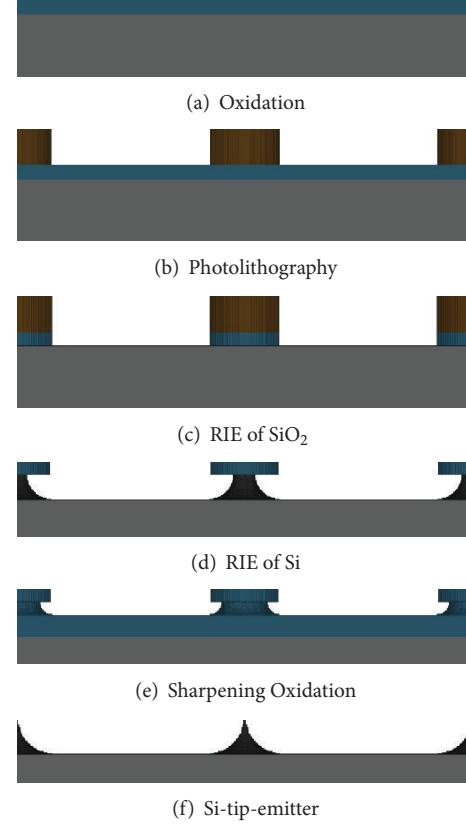


FIGURE 2: Schematic of the structured cathode fabrication process (simulated with IntelliSuite). (a) Thermal growth of SiO_2 layer. (b) Photolithography with AZ5214. (c) Transferring of the structures into SiO_2 by reactive-ion etching. (d) Reactive-ion etching of the bulk Si. (e) Sharpening of the tips by wet thermal oxidation. (f) Wet chemical removal of SiO_2 .

TABLE 1: Anisotropy factor f depending on the etching parameters (pressure and power). Symbols in brackets belong to Figure 6.

	50 mTorr	70 mTorr	90 mTorr
90 W	0.58 (○)	0.55 (□)	0.43 (◇)
120 W	0.61 (△)	0.53 (▽)	—
150 W	0.65 (▷)	0.51 (◁)	—

3. Results and Discussion

The power of plasma is varied from 90 to 150 W and the pressure from 50 to 90 mTorr, resulting in 9 several parameter sets (Table 1) with different anisotropy (Figure 5). The etching time amounts to 60 s. A full undercut of the SiO_2 disks is caused by a pressure of 90 mTorr at high power (120 W or 150 W).

3.1. Effect of RIE Parameters on the Geometry. The pressure has a strong effect on the factor of anisotropy. The reduction of pressure increases significantly the anisotropic factor (Figure 6(a)). Lower pressure causes fewer ions in the plasma, which are able to collide with each other at the same power in the chamber. Hence the ions are more directed perpendicular

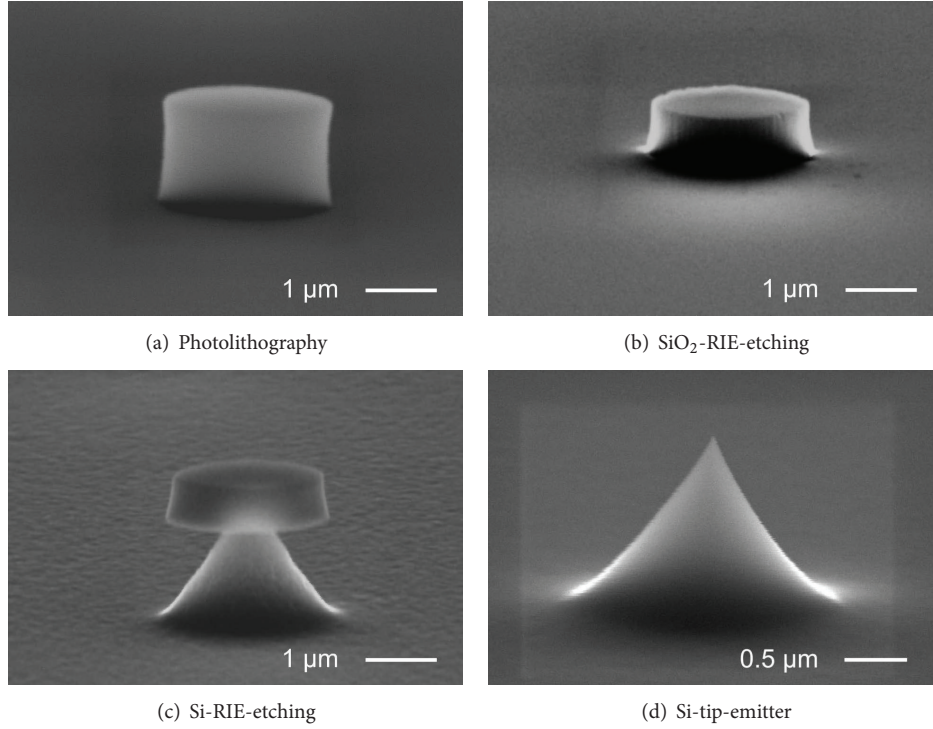


FIGURE 3: SEM images of the structured cathode fabrication process. (a) Developed photoresist. (b) Patterned SiO₂ disks. (c) Etched bulk Si. (d) Final emitter.

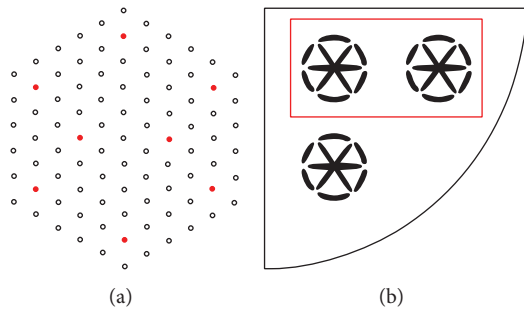


FIGURE 4: Schematic position of the investigated (a) tips in an array (8 of 91) and (b) chips on each quarter (2 of 3)

to the target. Therefore the anisotropic factor is high at low pressures and vice versa.

By increasing the power, the energy of the ions in the chamber is rising. At low pressure (blue line in Figure 6(b)) they are more able to impact the target without other hits. The anisotropic factor is rising, too. The higher the pressure is, the more reactive the molecules SF₆ are in the plasma. That means that there are more possible collisions on the way, because of the higher number of ions in the chamber. Moreover the effect of the chemical reaction is stronger and the directions of the impacting ions are more distributed, so the etching result is less anisotropic. This results in a lower anisotropy factor, while energy is higher (green line in Figure 6(b)).

Due to a higher anisotropy of etching, the aspect ratio of the tip can be maximized. This causes a larger β -factor.

3.2. Investigation on Homogeneity and Measurement Results. Changing power and pressure causes a variation of etch rates within the radius of the wafer, which is the homogeneity of the unit (Figure 7). SEM images are shown in Figure 8. Furthermore, low pressure (50 mTorr) results in quite homogeneous etching, regarding height of emitters and undercut of disks (Figures 7(c) and 7(d)). There are fewer ions in the plasma, due to low pressure in the chamber. The scattering of the ions on other particles and SiO₂ disks on the wafer is lower, leading to a more controlled and homogeneous process. However the etch rate is lower. This effect can be compensated by a longer time (1.5x–2.0x) of etching.

The final oxidation thickness is dependent on the remaining diameter of the Si under the SiO₂. The thermal wet oxidation is very homogeneous (a variation of less than 4% over the whole wafer). They have no observable effect on further differences of the homogeneity of the etched emitters.

Hence, with a lower pressure, it is possible to produce quite homogeneous cathodes with a high anisotropic factor across the wafer (Figures 8(c) and 8(d)).

FE measurements were performed on tip arrays, which were etched at low pressure (50 mTorr) and with an increased power of 120 W in order to get a high anisotropy factor (Figure 6). The height was around 1 μm with a radius of <40 nm and a tip-to-tip distance of 20 μm (Figure 9).

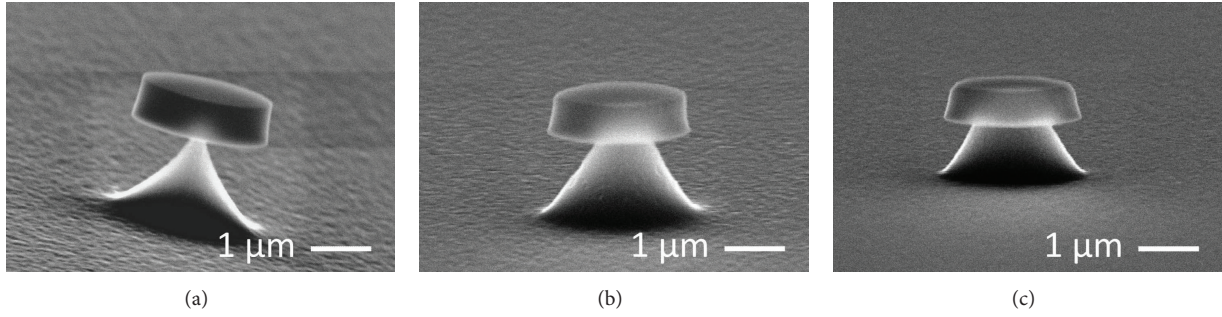


FIGURE 5: SEM images of tips after the Si etching with three different anisotropy factors: (a) $f = 0.4$, (b) $f = 0.5$, and (c) $f = 0.6$.

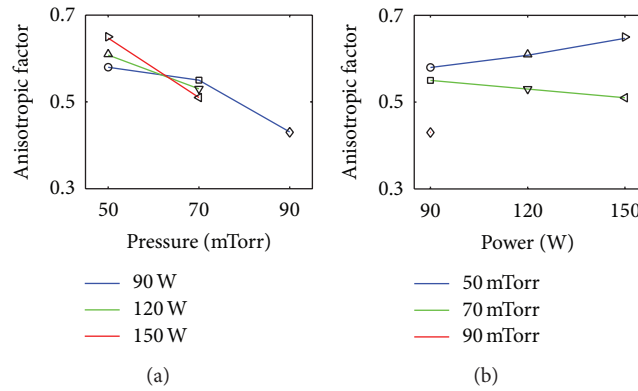


FIGURE 6: Dependence of the anisotropic factor on pressure (a) and power (b).

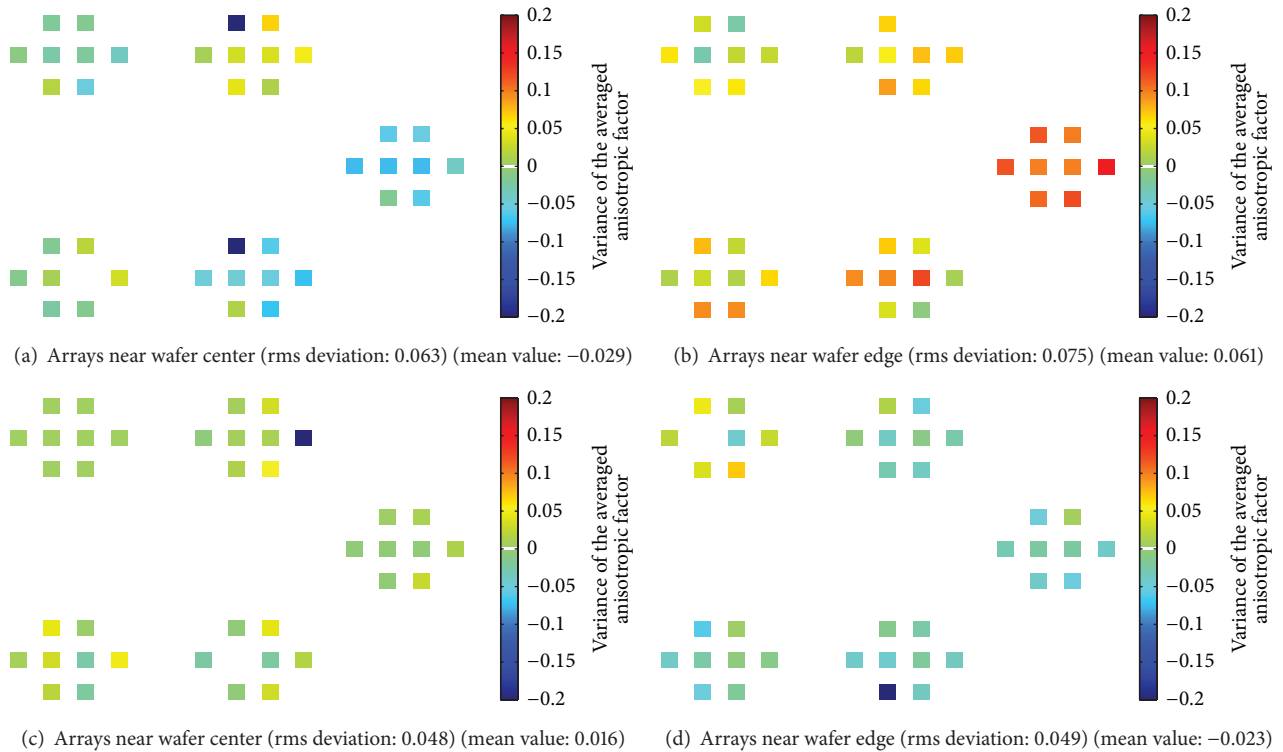


FIGURE 7: Variation of the anisotropic factor from the averaged value of anisotropy on the quarter at different etch parameters: (a) and (b) 90 mTorr, 60 s, 90 W, (c) and (d) 50 mTorr, 90 s, 90 W. Values in brackets are the root mean square deviation and the arithmetic mean of the variation.

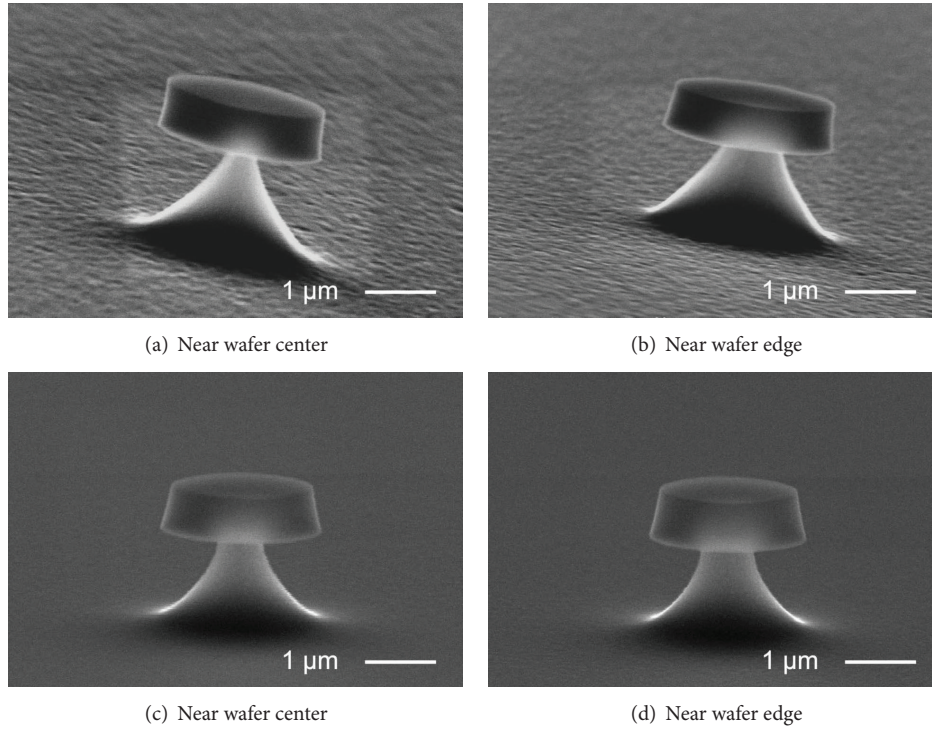


FIGURE 8: SEM images of the emitters after RIE of Si at different etching parameters: (a) and (b) 90 mTorr, 60 s, 90 W, (c) and (d) 50 mTorr, 90 s, 90 W.

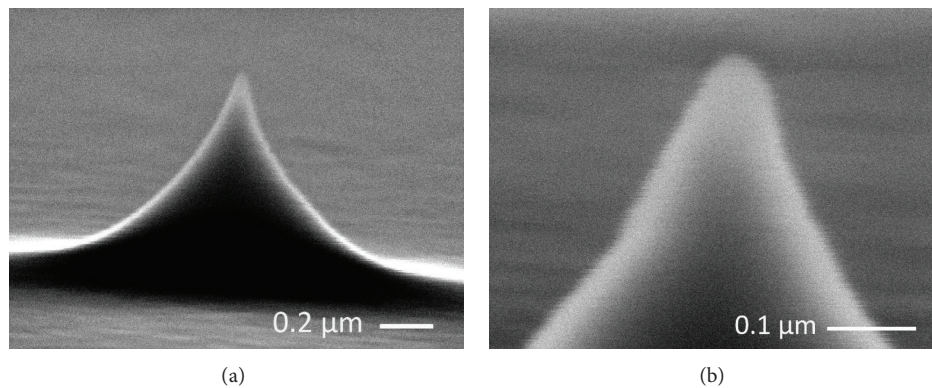


FIGURE 9: SEM images of emitters measured at the investigation: (a) with a height of $0.9 \mu\text{m}$ and (b) with a radius of 40 nm .

A comprehensive investigation of the field emission properties of these structures is given in [6]. The array with 547 emitters showed an integral FE-current up to 10^{-7} A at an electric field of $50 \text{ V}/\mu\text{m}$. An on-set-field of around $40 \text{ V}/\mu\text{m}$ for a FE-current of 1 nA was measured. Furthermore the optimization in the RIE process results in a homogeneous emission over the entire array with almost 99% efficiency [6].

The investigation of the anisotropy over the wafer (part 3.2) proves that a low pressure of around 50 mTorr results in a good homogeneity of the emitters over the complete wafer area. The FE measurement showed a good homogeneity of all individual emitters within an array, too.

4. Conclusion and Outlook

The dependence of anisotropy on the etching parameters (pressure and power) of RIE was investigated. Higher pressure increases the lateral etching rate and results in lower anisotropy. The influence of power on the anisotropic factor depends on the pressure. Low pressure causes higher anisotropy with a less scattering of the anisotropic factor. The homogeneity over the entire wafer was improved and due to the higher anisotropy a high aspect ratio of the tips was realized. With adjusted power an optimized etching step was achieved. The field emission investigation shows

homogeneous emission of the emitters, which were fabricated with this enhanced process. This opens the possibility to build homogeneous cathodes, which are able to carry stable current for advanced vacuum microelectronic devices.

Conflict of Interests

The authors declare that there is no conflict of interests regarding the publication of this paper.

Acknowledgments

The underlying project was founded by the German Federal Ministry of Education and Research with sponsorship-number 03FH004PX2. The authors of this paper assume responsibility for its content. The authors would like to thank the team for the support.

References

- [1] R. Schreiner, F. Dams, C. Prommesberger et al., "Silicon-based integrated field emission electron sources for sensor application," in *Proceedings of the 24th International Vacuum Nanoelectronics Conference (IVNC '11)*, pp. 19–20, July 2011.
- [2] R. Schreiner, C. Prommesberger, C. Langer et al., "Highly uniform and stable electron field emission from b-doped si-tip arrays for applications in integrated vacuum microelectronic devices," in *Proceedings of the 25th International Vacuum Nanoelectronics Conference (IVNC '12)*, pp. 1–2, 2012.
- [3] R. H. Fowler and L. Nordheim, "Electron emission in intense electric fields," *Proceedings of the Royal Society of London A*, vol. 119, no. 781, pp. 173–181, 1928.
- [4] C. Langer, C. Prommesberger, F. Dams, and R. Schreiner, "Theoretical investigations into the field enhancement factor of Silicon structures," in *Proceedings of the 25th International Vacuum Nanoelectronics Conference (IVNC '12)*, pp. 148–149, July 2012.
- [5] F. Dams, A. Navitski, C. Prommesberger et al., "Homogeneous field emission cathodes with precisely adjustable geometry fabricated by Silicon technology," *IEEE Transactions on Electron Devices*, vol. 59, no. 10, pp. 2832–2837, 2012.
- [6] P. Serbun, B. Bornmann, A. Navitski et al., "Stable field emission of single b-doped si tips and linear current scaling of uniform tip arrays for integrated vacuum microelectronic devices," *Journal of Vacuum Science & Technology B: Microelectronics and Nanometer Structures*, vol. 31, no. 2, Article ID 02B101, 2013.
- [7] R. Legtenberg, H. Jansen, M. de Boer, and M. Elwenspoek, "Anisotropic reactive ion etching of Silicon using SF₆/O₂/CHF₃ gas mixtures," *Journal of the Electrochemical Society*, vol. 142, no. 6, pp. 2020–2028, 1995.

Research Article

Effect of Laser Welding Parameters on Formation of NiTi Shape Memory Alloy Welds

Wei Wang,^{1,2} Xiaohong Yang,¹ Hongguang Li,² Fuzhong Cong,² and Yongbing Liu¹

¹ College of Materials Science and Engineering, Jilin University, Changchun 130012, China

² Aviation University of Air Force, Changchun 130022, China

Correspondence should be addressed to Yongbing Liu; yongb.liu@163.com

Received 30 December 2013; Revised 11 March 2014; Accepted 13 March 2014; Published 3 April 2014

Academic Editor: Kean Aw

Copyright © 2014 Wei Wang et al. This is an open access article distributed under the Creative Commons Attribution License, which permits unrestricted use, distribution, and reproduction in any medium, provided the original work is properly cited.

In this work experimental trials of welding of NiTi flat plates with 2.0 mm thickness were conducted using a 4.5 kW continuous wave (CW) Nd:YAG laser. The influences of laser output power, welding speed, defocus amount and side-blow shielding gas flow rate on the morphology, welding depth and width, and quality of the welded seam were investigated. Meanwhile, the effects of heat input on the mechanical and functional properties of welded joints were studied. The results show that laser welding can take better formation in NiTi alloys. The matching curves with laser power and welding speed affecting different formation of welds were experimentally acquired, which can provide references for laser welding and engineering application of NiTi alloy. The heat input has obvious effects on the ultimate tensile strength (UTS) and shape memory behavior of the welded joints.

1. Introduction

NiTi shape memory alloys (SMA) can offer the best combination of functional properties in several shape memory effects (SME) and pseudoelasticity (PE) applications [1]. Due to the low formability alloys, a suitable joining technique must be found to obtain devices and components with complex geometries. Only a few welding techniques for joining NiTi alloys are reported in the literature [2–5]. In recent years the laser has been successfully introduced as a suitable joining technique for NiTi plates. In particular, the Nd:YAG source is suitable for welding low thickness components due to its high precision and reduced HAZ [4]. Moreover, appropriate control of the process parameters can ensure good reproducibility of the results [6].

The effects introduced by the weld on the martensitic transformation will depend both on the microstructure of the reference material and on the welding process parameters. Before the laser welding technology is widely used for NiTi shape memory alloy (SMA), a deeper understanding needs more data on welding process parameters and unfortunately very few experimental comparisons on the welding process

parameters are reported [4, 6–9]. A large number of experiments on the welding process parameters would need to be measured to generalize regularities.

In this paper, 2.0 mm thickness NiTi flat plates have been tested for butt welding by Nd:YAG laser. The aim of this experimental work is to explore the possibility of welding of NiTi SMA with different welding process parameters, accumulate database, and enlarge the application scope of laser-welding technology. Meanwhile, the laser welding for other SMA materials would benefit from the process regularities acquired through the experiments.

2. Experimental Details

Ti-50.9at.%Ni sheets about 2 mm in thickness were used throughout this investigation. The sheets were produced by cold rolling and successive ageing by heat treatment at 850°C for 30 minutes in pure argon atmosphere.

Before welding, any oxide layers and contamination were removed from the surfaces of the plates. In particular, the surfaces for welding were cleaned with acetone and ethanol

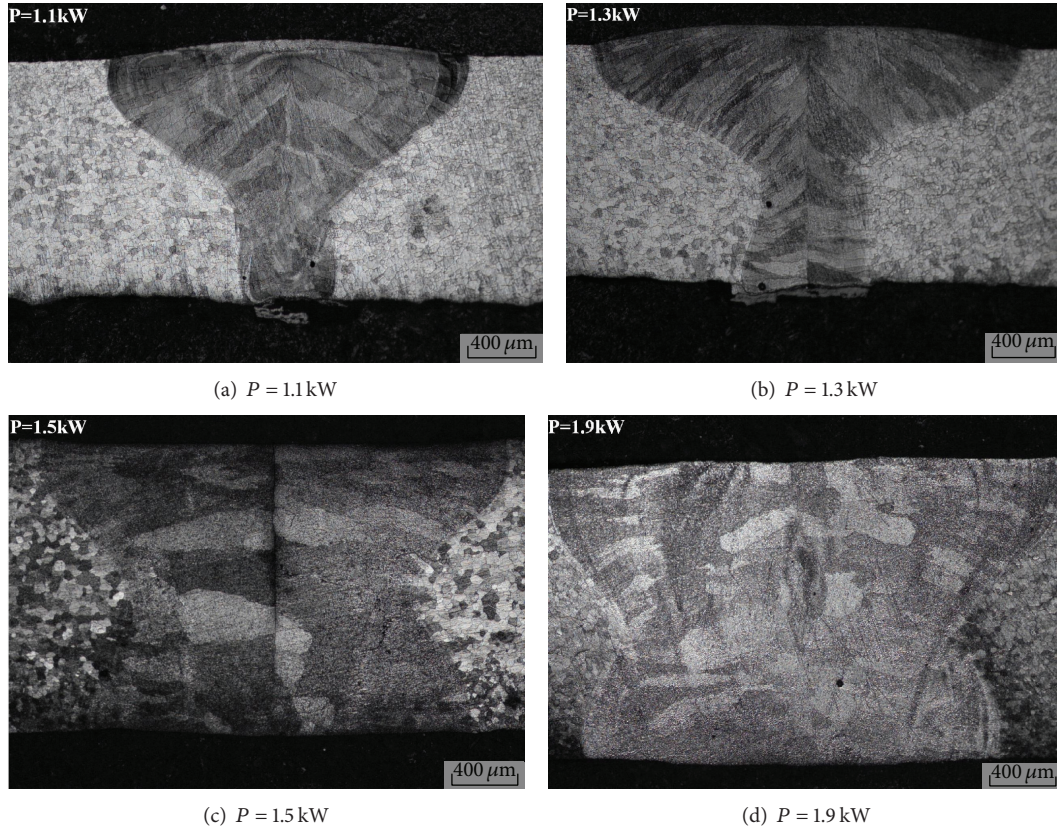


FIGURE 1: Influence of laser output power on cross-section morphologies of welded seam. ($\Delta Z = 0$ mm; $V = 1.5$ m/min; $U_f = 15$ L/min).

and then dried. The welding process was carried out using a Nd:YAG laser source (Gsi Lumonics AM356, 4.5 kW) operating in continuous wave (CW). One kind of special shielding equipment, made of copper, was prepared to protect the welding zone against possible reaction between the molten metals and ambient air and to avoid the material overheating. Flow of high-purity argon gas can pass through the molten pool from top, back, and lateral sides. Metallographic sample of the welded seam was prepared using standard mechanical polishing procedures and etched in $\text{HF} : \text{HNO}_3 : \text{H}_2\text{O}$ solution in volume ratio of 1 : 3 : 10. Microstructure of the welded seam was characterized by Olympus optical microscopy.

The employed parameters were optimized based on our experimental work; that is, laser output power was varied between 1 kW and 3.5 kW, laser beam scanning velocity varied between 0.9 m/min and 3 m/min, and direction of the side-blow shielding gas was pointed to the opposite welding direction, with an angle of 35° to the horizon plane, flow rate of side-blow shielding gas of 5~25 L/min, and defocus amount of $-3\sim 2$ mm. If the focus point is above the surface of the workpiece, the defocus amount is positive; if below, the defocus amount is negative.

The experiments were designed to study the influences of each parameter on the weld quality when other parameters were kept constant. Using the experiments we can acquire the optimized parameters for high quality full penetration welded joint.

Besides the above, we defined the laser output power as P , welding speed as V , side-blow shielding gas flow rate as U_f , defocus amount as ΔZ , the cap width as W_u , the root width as W_b , and the weld penetration as H_p , respectively.

In order to study the effects of heat input on the mechanical and functional properties of welded joints, stress-strain behavior and shape memory behavior were evaluated by uniaxial quasistatic tensile tests and mechanical cycles, which were carried out in the following way: (a) strain controlled uniaxial loading at a strain rate of 0.04/min up to a total strain $\varepsilon_t = 8\%$; (b) complete unloading at the same rate and recording the permanent strain ε_p .

3. Results and Discussions

3.1. Influence of Laser Output Power. Experimental observation showed that the morphology of the cross sections of the welded seams was asymmetric and changing from T shape and V shape to X shape with the increasing of the output power of laser. Different morphologies can be seen clearly in Figure 1.

Figure 2 indicated that both depth and width increased with the increasing of laser output power. A higher output power was naturally expected to increase the input energy imposed on the welded seam, hence causing a comparatively large amount of melted or vaporized metal [10, 11]. By observing the cross section of the welded seam, it was clear

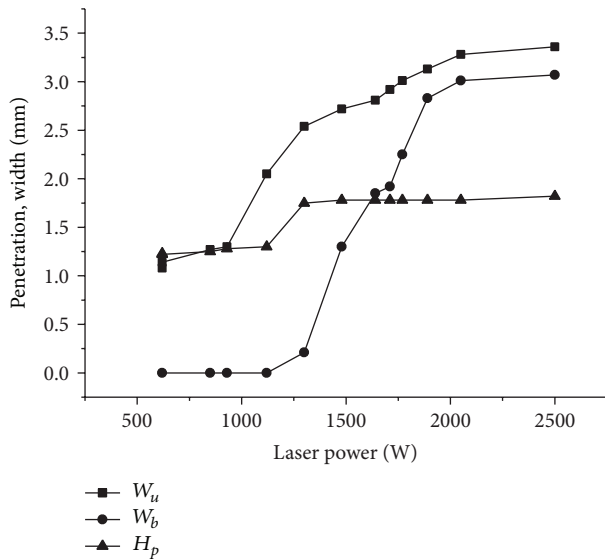


FIGURE 2: Influence of laser output power on width and penetration of welded seam. ($\Delta Z = 0$ mm; $V = 1.5$ m/min; $U_f = 15$ L/min).

that full penetration welding occurred within the laser output power range of 1.5~1.9 kW, while partial fusion occurred within the range of 1.1~1.5 kW and with welding speed of 1.5 m/min.

3.2. Influence of Welding Speed. Experimental observation showed that the cross-section morphology of welded seams was asymmetric and changing from T shape and V shape to X shape with the decreasing of the laser scan speed, which changed with the decreasing of the laser scan speed. Different morphologies can be seen clearly in Figure 3.

Figure 4 expressed that welding depth and width change with the laser scan speed. It was noted that the welding depth and width were decreased with the increase of the laser scan speed. Because the welding speed matches opposite with the heat input, the increase of welding speed means the decrease of input energy per unit weld length exerted on the welding line, producing a small amount of intermixed melt and finally a thinner welding depth and narrower width [12].

Through observing the cross section of the welded seam, a full penetration welding occurred within the speed range of 1.8~1.2 m/min, while partial fusion occurred in the range of 2.1~3 m/min and with laser output power of 1.5 kW.

3.3. Influence of Defocus Amount. Experimental observation showed that the cross-section morphology of welded seams was asymmetric and changing from T shape and X shape to T shape with the defocus amount variation. Different morphologies can be seen clearly in Figure 5.

Figure 6 indicated that the welding depth and width varied with defocus amount. Power density exerted on the workpiece depends on both the laser beam's power density and the relative amount between the surface of the workpiece and the focus plane. Of course, different defocus amount represents different power density exerted on the workpiece

by laser. As shown in Figure 6, full penetration occurred under the defocus amount range of $-2 \sim -3$ mm, while partial fusion occurred for $-3 \sim -2$ mm and $+3$ mm. The welding width increased with the decreasing of absolute value of defocus amount. Based on the laser beam transfer characteristics, it is known that the laser spot is the smallest in the focus plane and the power density is the largest. The laser beam gradually diverged away from the focus point. For the positive defocus amount, the laser beam enters the keyhole diverged gradually and induces decreased power density and welding depth, while for the negative defocus amount, the laser beam enters the keyhole converged gradually to the focus point and imposes higher power density than that of the surface of the workpiece, favoring more strong melting and vaporization, facilitating the transfer of the laser energy to more depth, and thus deeper welding depth. Nevertheless, the dimension of the laser spot increases sharply, changing the space distribution of the laser power density, thus decreasing the welding depth. With the increase of positive and negative defocus amount, the spot area irradiated on the facade side of the welding seam increased, inducing the increase of melted metal.

3.4. Influence of Side-Blow Shielding Gas Flow Rate. Experimental observation showed asymmetric welded seams and reflected the influence of side-blow shielding gas flow rate on formation of welded seam. According to the various side-blow shielding gas flow rate, different morphologies can be seen clearly in Figure 7.

Figure 8 showed that the welding depth and width change with various side-blow shielding gas flow rates. The gas flow rates from left to right are 25 L/min, 20 L/min, 15 L/min, 10 L/min, and 5 L/min. When the gas flow rate was below 5 L/min, the weld metal became oxidized and the protection effect was bad; when it was over 10 L/min, the surface of weld appeared silvery white and the protective effectiveness was very good. With the increase of the side-blow shielding gas flow rate, the weld width was a little narrowed down and the roughened surface and uneven formation were shown. The protective effectiveness and the weld formation was the best as side-blow shielding gas flow rate was 15 L~20 L/min. The above-mentioned considerations underline that the shielding gas plays an important role on the formation of weld. On the other hand, the experiments demonstrate that high gas flow rates yield progressively unstable laser arc; in particular, they do not affect significantly bead geometry and bead depths.

3.5. Effect of Laser Power and Welding Speed on Formation of Weld. Figure 9 showed the effect of two main welding parameters, laser power and welding speed, on the formation of the weld. With the laser power increasing, the type of weld formation changed from partial fusion to full penetration and to excessive penetration finally. With a certain laser power different welding speed can lead to different formation of the weld. Among three types of weld formation, partial fusion and excessive penetration are undesired in practical application. The matching curves were experimentally acquired, which can provide references for laser welding and engineering application of NiTi alloy.

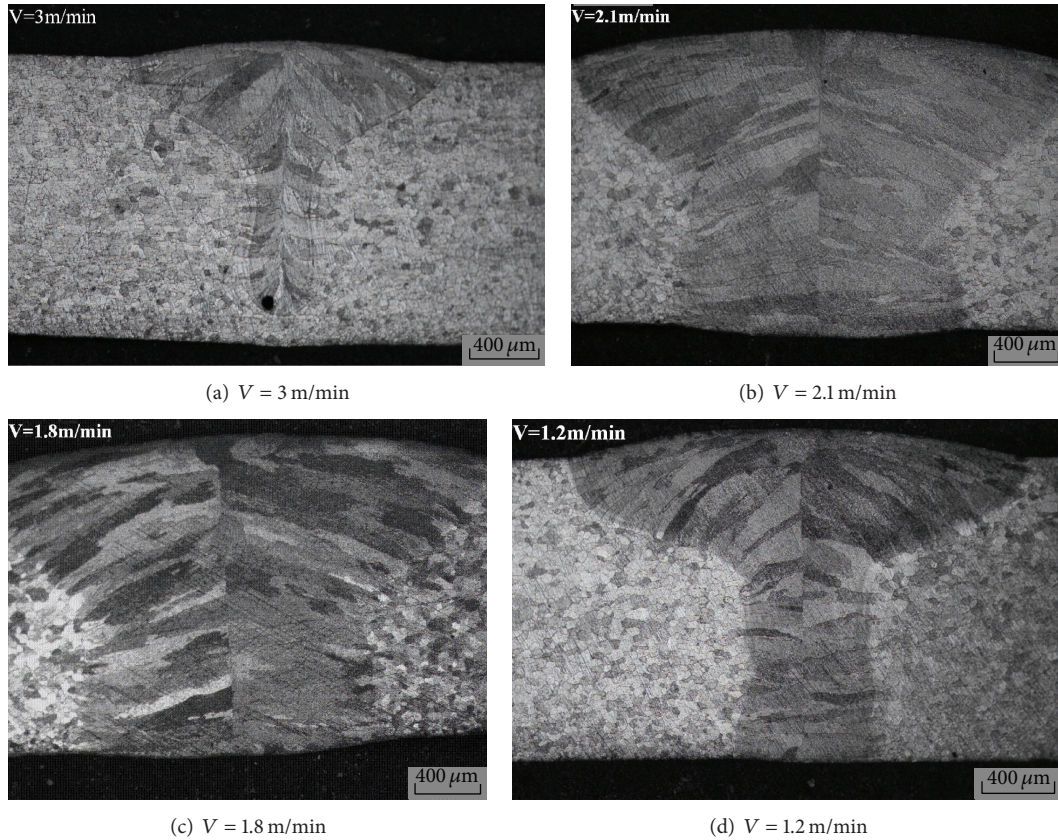


FIGURE 3: Influence of welding speed on cross-section morphologies of welded seam. ($\Delta Z = 0$ mm; $P = 1.5$ kW; $U_f = 15$ L/min).

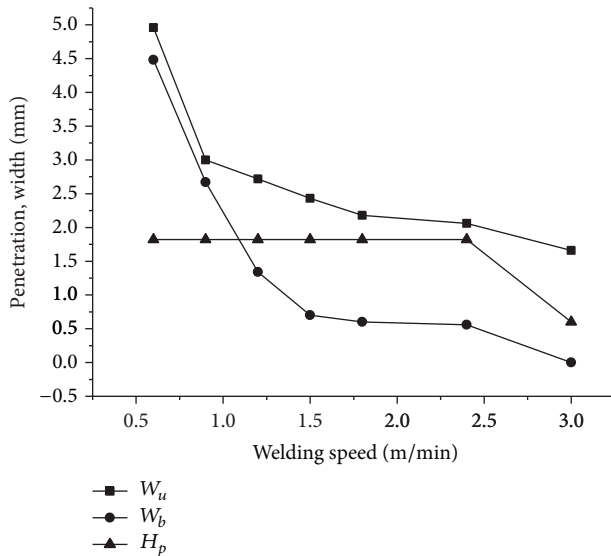


FIGURE 4: Influence of welding speed on width and penetration of welded seam. ($\Delta Z = 0$ mm; $P = 1.5$ kW; $U_f = 15$ L/min).

3.6. Effect of Heat Input on Tensile Properties. The heat input is directly related to the laser power, welding speed, and welding efficiency. It can be calculated from heat input $E = (P/V) \times \eta$, where η is the welding efficiency. For the same material and

welding process, the efficiency will not change. For simplicity, η can be assumed as a constant of approximate value 1. So, it is clear that if the P increases or V decreases, the weld heat input will increase. That is to say, the heat input can be adjusted with the change of the laser power or welding speed. In order to evaluate the modification caused by welding in the stress-strain behavior of the material, standard tensile tests were carried out for full penetration samples.

Table 1 and Figure 10 showed that the tensile properties of the welded joints had a little difference with different heat input. The reason might be that welded joints have different microstructure. When the heat input is high, welding area melts completely. The grains are uniform and fine. So the tensile properties are relatively high. When the heat input is medium, the grains in the welding zone are columnar grains and exhibit poor strength. When the heat input is low, the fusion method belongs to heat conduction. So the strength is better than coarse columnar grains. Because the weld metal has a typical cast structure, its strength and elongation are much lower than that of the rolled base metal. Based on the above analyses, it can be concluded that the larger the heat input, provided that full penetration occurs, the higher the tensile properties of welded joints.

3.7. Effect of Heat Input on Functional Properties. Figure 11 showed the mechanical cycles up to 8% in terms of stress-strain curves for the three full penetration samples. By

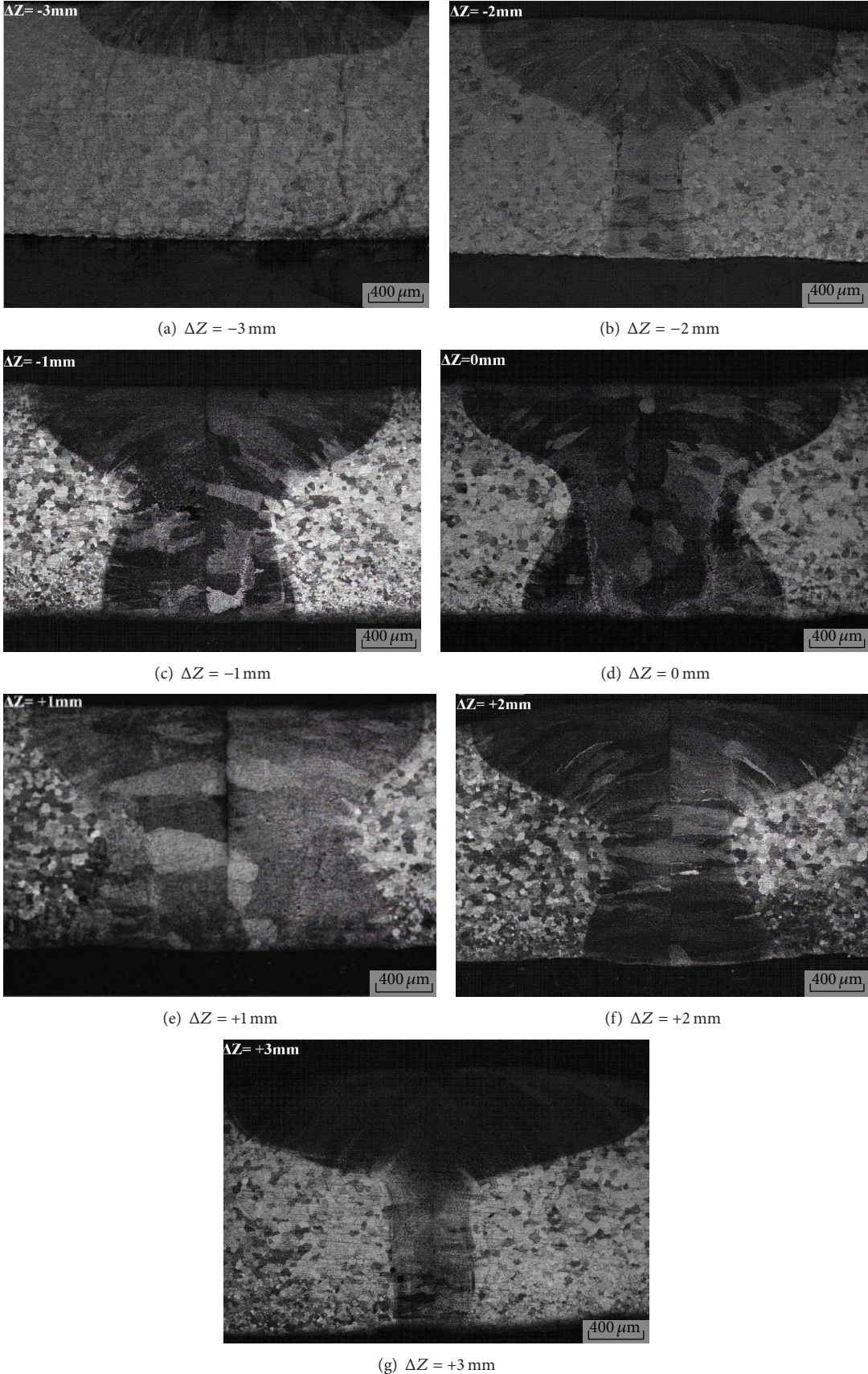


FIGURE 5: Influence of defocus amount on cross-section morphologies of welded seam. ($P = 1610\text{ W}$; $V = 1.5\text{ m/min}$; $U_f = 15\text{ L/min}$).

TABLE 1: UTS and elongation of the welded joints.

Full penetration samples number	Sample 1	Sample 2	Sample 3	Base material
Heat input (J/mm)	54.8	64	70.4	
UTS (MPa)	503	450	531	1100
Elongation (%)	4.1	5.1	4.9	7.1

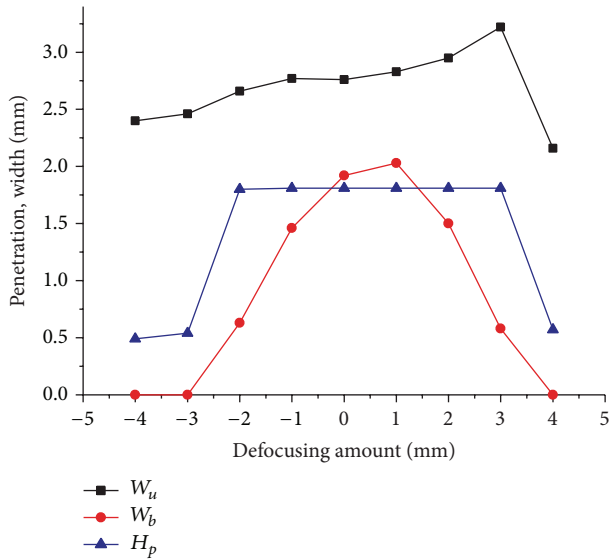


FIGURE 6: Influence of defocus amount on width and penetration of welded seam. ($P = 1610$ W; $V = 1.5$ m/min; $U_f = 15$ L/min).

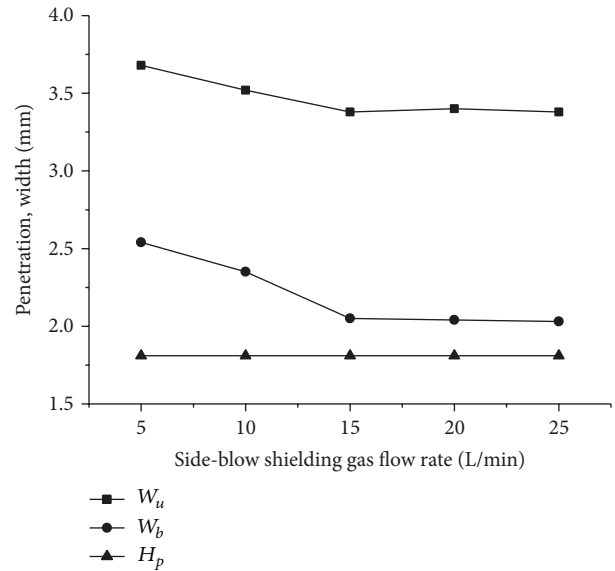


FIGURE 8: Influence of side-blow shielding gas flow rate on width and penetration of welded seam. ($P = 1.5$ kW; $V = 0.9$ m/min; $\Delta Z = 0$ mm).

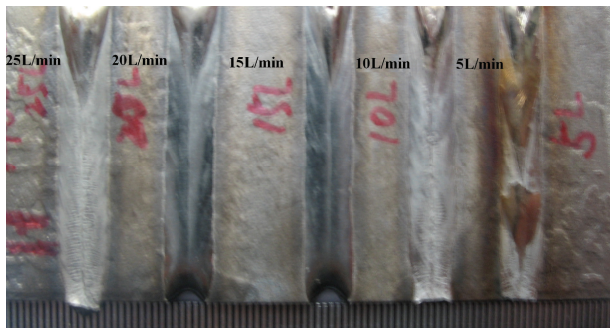


FIGURE 7: Influence of side-blow shielding gas flow rate on formation of welded seam. ($P = 1.5$ kW; $V = 0.9$ m/min; $\Delta Z = 0$ mm).

comparing the stress-strain measurements of the weld, the permanent deformation value of the weld was recorded. The ϵ_p value of sample 3 with high heat input is 1.92%. The ϵ_p value of sample 2 with medium heat input is 3.02%. The ϵ_p value of sample 1 with low heat input is 2.42%. The trends of the strain recovered for SME and permanent deformation for three welded samples indicated that high heat input led to smaller residual deformation. The reason for that might be the same with the effects of heat input on tensile properties.

4. Conclusions

In order to obtain a stable and efficient NiTi laser welding process, the effects of welding parameters including laser

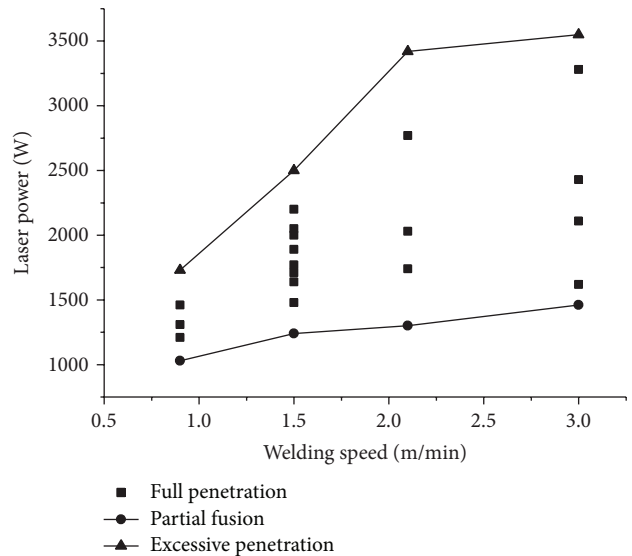


FIGURE 9: Influence of laser power and welding speed on formation of weld. ($P = 1030\sim 3550$ W; $V = 0.9\sim 3$ m/min; $\Delta Z = 0$ mm; $U_f = 15$ L/min).

power, welding speed, defocus amount, and gas-assisting blowing on weld shaping have been taken into consideration. In addition, the effects of heat input on mechanical and shape memory behavior of the Ti-50.9at.%Ni alloy were

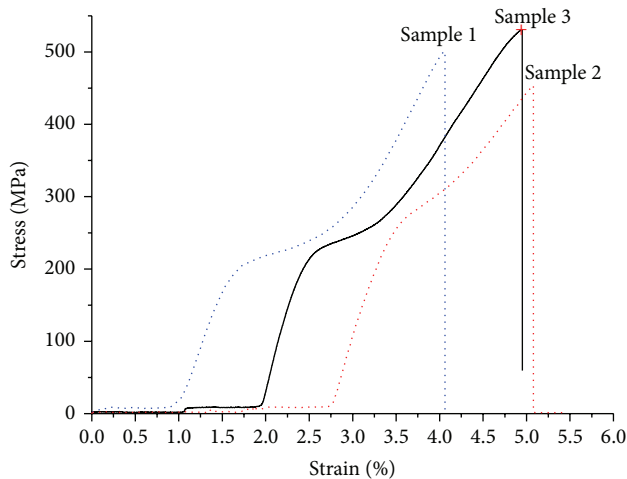


FIGURE 10: Stress-strain curves of the welded material for different heat input.

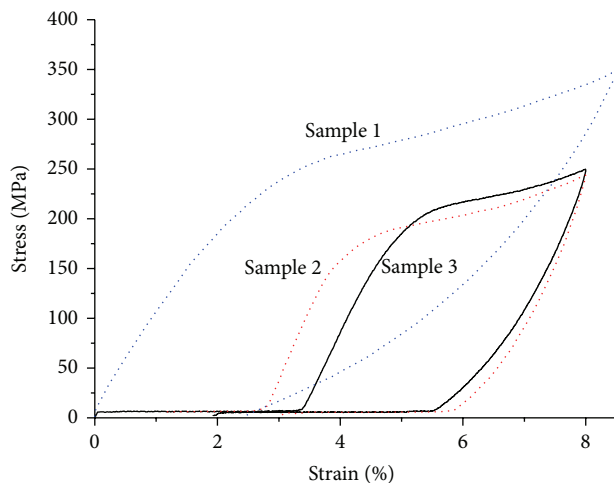


FIGURE 11: Stress-strain cycles with ϵ_t of about 8% for different heat input.

investigated. The appropriate matching of main welding parameters is the key to realize the better weld formation.

The defocus amount around $-2\sim 3$ mm level can lead to full penetration for 2 mm thick tapes of NiTi alloys. The defocus amount of $0\sim 1$ mm can obtain optimal formation of the weld.

The protective effectiveness and the weld formation are the best when side-blow shielding gas flow rate keeps at $15\sim 20$ L/min.

The matching curves with laser power and welding speed affecting different formation of welds were experimentally acquired, which can provide references for laser welding and engineering application of NiTi alloy. The heat input of $54.8\sim 70.4$ J/mm can acquire optimal formation of the weld.

For full penetration welded joints, the larger the heat input, the higher the tensile properties and the smaller permanent deformation in strain recovering process. The results showed an obvious reduction in the ultimate tensile

strength of the welded material together with a reduction of the elongation to fracture. However, shape memory behavior of the welded joints remains acceptable.

The laser welding can take better formation in NiTi alloys. In the area of thin SMA materials, as well as the materials that are difficult to weld by conventional welding methods, laser welding would play a big role in the future.

Conflict of Interests

The authors declare that there is no conflict of interests regarding the publication of this paper.

Acknowledgments

The authors would like to acknowledge the financial support of the Jilin Provincial Science and Technology Department Project (20130101077)JC), the Jilin Provincial Science and Technology Department Project (201205009), and the Jilin Provincial Education Department Project (2010015).

References

- [1] C.-W. Chan, *Laser micro-welding of a NiTi shape memory alloy for biomedical applications [Ph.D. dissertations]*, The Hong Kong Polytechnic University, 2008.
- [2] A. Tuissi, S. Besseghini, T. Ranucci, F. Squatrito, and M. Pozzi, "Effect of Nd-YAG laser welding on the functional properties of the Ni-49.6at.%Ti," *Materials Science and Engineering A*, vol. 273-275, pp. 813-817, 1999.
- [3] A. Falvo, F. M. Furgiuele, and C. Maletta, "Laser welding of a NiTi alloy: mechanical and shape memory behaviour," *Materials Science and Engineering A*, vol. 412, no. 1-2, pp. 235-240, 2005.
- [4] X. Zhao, W. Wang, L. Chen et al., "Two-stage superelasticity of a Ce-added laser-welded TiNi alloy," *Materials Letters*, vol. 62, no. 20, pp. 3539-3541, 2008.
- [5] C. van der Eijk, H. Fostervoll, Z. K. Sallom, and O. M. Akselsen, "Joining of Specialty Materials," in *ASM Materials Solutions Conference & Exposition*, ASM International, Pittsburgh, Pa, USA, 2003.
- [6] X. Zhao, W. Wang, L. Chen, F. Liu, J. Huang, and H. Zhang, "Microstructures of cerium added laser weld of a TiNi alloy," *Materials Letters*, vol. 62, no. 10-11, pp. 1551-1553, 2008.
- [7] H. Gugel, A. Schuermann, and W. Theisen, "Laser welding of NiTi wires," *Materials Science and Engineering A*, vol. 273-275, pp. 149-160, 1999.
- [8] H. Rosner, A. V. Shelyakov, A. M. Glezer, and P. Schlobmacher, "On the origin of the two-stage behavior of the martensitic transformation of Ti50Ni25Cu25 shape memory melt-spun ribbons," *Materials Science and Engineering A*, vol. 307, no. 1-2, pp. 188-189, 2001.
- [9] Y. G. Song, W. S. Li, L. Li, and Y. F. Zheng, "The influence of laser welding parameters on the microstructure and mechanical property of the as-jointed NiTi alloy wires," *Materials Letters*, vol. 62, no. 15, pp. 2325-2328, 2008.
- [10] T. Y. Kuo and H. C. Lin, "Effects of pulse level of Nd-YAG laser on tensile properties and formability of laser weldments in automotive aluminum alloys," *Materials Science and Engineering A*, vol. 416, no. 1-2, pp. 281-289, 2006.

- [11] X.-B. Liu, M. Pang, Z.-G. Zhang, W.-J. Ning, C.-Y. Zheng, and G. Yu, "Characteristics of deep penetration laser welding of dissimilar metal Ni-based cast superalloy K418 and alloy steel 42CrMo," *Optics and Lasers in Engineering*, vol. 45, no. 9, pp. 929–934, 2007.
- [12] W. Chunming, H. Lunji, and H. Xiyuan, "The relationship between plasma optic signal and penetration depth during partial-penetration laser welding," *Laser Technology*, vol. 30, pp. 23–26, 2006.

Research Article

NiTi Intermetallic Surface Coatings by Laser Metal Deposition for Improving Wear Properties of Ti-6Al-4V Substrates

Mokgadi Nomsa Mokgalaka,^{1,2} Sisa Lesley Pityana,^{1,2}
Patricia Abimbola Idowu Popoola,² and Tebogo Mathebula¹

¹ Council of Scientific and Industrial Research, National Laser Centre, Building 46F, P.O. Box 395, Pretoria 0001, South Africa

² Department of Chemical, Metallurgical and Materials Engineering, Tshwane University of Technology, PMB X680, Pretoria 0001, South Africa

Correspondence should be addressed to Sisa Lesley Pityana; spityana@csir.co.za and Patricia Abimbola Idowu Popoola; popoolaapi@tut.ac.za

Received 24 October 2013; Accepted 4 February 2014; Published 17 March 2014

Academic Editor: Feng Zhao

Copyright © 2014 Mokgadi Nomsa Mokgalaka et al. This is an open access article distributed under the Creative Commons Attribution License, which permits unrestricted use, distribution, and reproduction in any medium, provided the original work is properly cited.

The NiTi intermetallic possesses a number of good properties, such as high wear, oxidation, and corrosion resistance. This paper focuses on the deposition of NiTi intermetallic coatings on Ti6Al4V substrate by laser melting of Ti and Ni elemental powder mixtures. The effect of varying the Ti content in the NiTi composition on the microstructure and wear properties of the coatings was investigated. The microstructure of the NiTi intermetallic coatings were characterized by the scanning electron microscope (SEM) equipped with Energy Dispersive Spectroscopy (EDS). The wear properties of the coatings were performed under accelerated dry sliding wear tests. The results obtained from the SEM/EDS analysis; show that the coatings consist of Ni and Ti elements from the feedstock, and the NiTi, NiTi₂, and NiTi₃, intermetallic phases. Dry sliding wear analysis revealed that there is correlation between the hardness and the wear rate. The coatings displayed significant improvement in wear resistance up to 80% compared to the substrate.

1. Introduction

Titanium alloys have low hardness values, poor resistance to wear, and oxidation at high temperatures [1]. These limitations can be overcome by changing the nature of the surface of titanium alloys using different surface engineering techniques. Methods such as nitriding, thermal spraying, and chemical or physical vapour deposition (CVD or PVD) have been well-known technologies that improve the surface properties of titanium and titanium alloys. However, these methods have limitations such as a long processing time, easy deformation, and limited bond strength between the coating and the substrate [2]. Laser processing techniques have been found to be free from these shortcomings and can be used to enhance the surface properties of ferrous and nonferrous metal surfaces [3–6].

As a flexible process, laser processing can be used in the deposition of different coatings either to improve the surface

properties or to refurbish worn-out parts [7]. Amongst the many benefits of the laser surface coating methods, laser deposition is the preferred method because of the novel microstructures and phases that can be formed due to rapid cooling and solidification rates associated with the processing technique [8]. Coatings generally have such microstructures that cannot be easily obtained by conventional techniques. One of the advantages of laser surface coating is that quite a number of metallic powders can be used to form intermetallic compounds exhibiting excellent wear resistance, good corrosion, and oxidation properties.

The Ti-Ni coatings have been a subject of great interest and have been widely exploited for a range of applications including aerospace, biomedical engineering, and microelectrochemical system due to the above-mentioned advantageous properties [9–13]. Stainless steel surfaces were coated with NiTi to enhance mechanical properties and corrosion resistance using different deposition techniques, including plasma

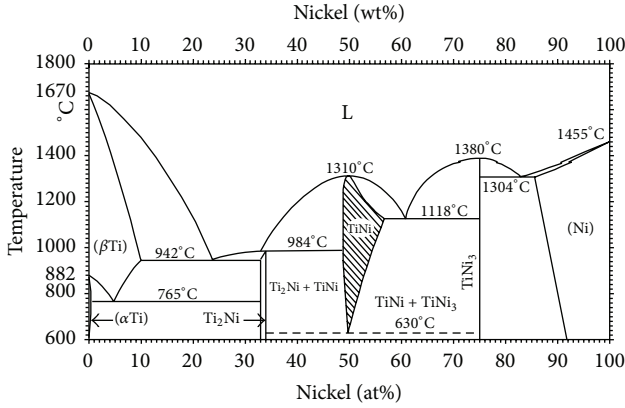


FIGURE 1: Equilibrium Ni-Ti phase diagram [20].

transfer arc (PTA), plasma welding, plasma spray coating, and sputtering process, all with different degrees of success [14–17].

Ozel et al. [18] studied microstructure characteristic of NiTi coating on stainless steel by transferred arc process. When the arc current was at 90–100 A, the amount of NiTi phase decreased and high dilution was observed. The coatings produced had a magnitude between 1 and 1.4 mm with the highest hardness values between 500 and 550 HVN. Van der Eijk et al. [19] studied plasma welding of NiTi to NiTi, stainless steel, and Hastelloy C276. The microstructure produced as a result of welding NiTi to NiTi had defects such as cracking, Ti carbides, and high volume of NiTi₂ phase. The strength of the weld was found to be less than that of the base material. Microstructure produced from the NiTi stainless steel weld had large cracks propagating from the NiTi side of the weld. This was attributed to the amount of NiTi melting larger than stainless steel which results in absorption of elements from the steel into NiTi.

The Ti-Ni binary phase diagram is shown in Figure 1 [20]. It indicates that this system contains the stable NiTi, Ni₃Ti, and NiTi₂ phases. The good toughness and ductility and the exhibited NiTi phase make it an ideal candidate for wear resistant application. The Ti₂Ni and Ni₃Ti are regarded as suitable particles for metal matrix reinforcements.

In this study, mechanically alloyed Ti and Ni elemental powders will be used to form *in situ* NiTi intermetallic thin surface coatings on the Ti6Al4V substrate. The laser metal deposition technique will be employed to melt powders of different compositions: Ti50Ni50, Ti45Ni55, and Ti55Ni45. The microstructure, phase composition, and microhardness of the coatings will be investigated.

2. Experimental Procedure

2.1. Materials. The materials used in the experiment are elemental nickel and titanium powders with the particle size fraction within the range of +45 microns and –63 microns. Prior to milling, the powders were weighed and mixed together to give nominal compositions of Ti55Ni45, Ti50Ni50, and Ti45Ni55 in weight%. The initially mixed

TABLE 1: Chemical composition of titanium alloy Ti6Al4V.

Element	Al	V	C	Fe	Cr	N	O	Ti
wt.%	6.11	4.17	0.083	0.083	0.001	0.014	0.02	Bal.

TABLE 2: Experimental process parameters for depositing the NiTi intermetallic coatings.

Sample	Process parameter	Values
Ti50Ni50	Laser power	800 W
	Beam spot diameter	2 mm
Ti55Ni45	Scanning speed	8 mm/s
	Powder feed rate	3 g/min
Ti45Ni55	Gas shielding and carrier	Argon
	Gas flow rate	5 L/min

powders were mechanically alloyed in a planetary ball mill by subjecting the particles to repeated welding, fracturing, and rewelding from the collision of the particles and the grinding medium. The milling was performed for two hours to allow the powders to reach a steady state where homogeneous NiTi powder was produced. The ball to powder ratio was kept uniform at 10:1 and the rotation speed of 300 rpm. After milling, the powder mixture was analysed by scanning electron microscopy to determine the change in morphology and the particle size.

2.2. Laser Surface Coating. The substrate material used was Ti6Al4V plate, with 72 × 72 × 5 mm³ dimensions. The plates were sandblasted and cleaned with acetone prior to the laser coating process. Table 1 shows the chemical composition of the titanium alloy Ti6Al4V. The NiTi prealloyed powders were free flowing. The powders were fed through a three-way nozzle with argon shielding gas stream. The argon gas flow rate was 5 L/min. The laser deposition process was carried out using a CW 4.4 kW Rofin Sinar Nd:YAG laser operating with 1.064 μm wavelength. The beam spot on the target was 2 mm in diameter. The scanning speed, laser power, and the powder flow rate were kept constant. Table 2 shows the experimental parameters used for depositing the NiTi intermetallic coatings.

2.3. Materials Characterization. Metallographic samples were sectioned with a Corundum L205 cut-off wheel using a Struers Discotom-2 cutting machine. After sectioning, the specimens were hot mounted in clear thermosetting Bakelite resin. The specimens were then ground and polished to a 0.04-micron (OP-S suspension) surface finish with a Struers TegraForce-5 auto/manual polisher and etched in Kroll's reagent by immersing the samples for approximately 10 seconds. Microstructure was characterized on Olympus BX51 M Optical Microscope (OM) and Jeol JSM 6510 Scanning Electron microscopy (SEM) built with Energy Dispersive Spectroscopy (EDS). X-ray diffraction (XRD) was conducted using the Rigaku/Dmax 2200 pc automatic X-ray diffractometer with Cu target Ka radiation to identify the phase constitution.

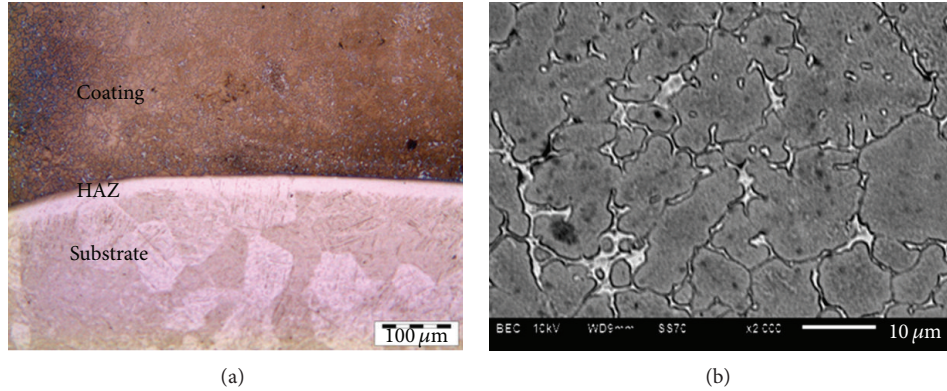
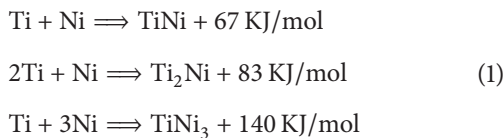


FIGURE 2: Micrographs of the laser deposited Ti50Ni50 coating; (a) optical image showing the interface of the coating and substrate; (b) SEM image of the coating.

3. Results and Discussion

3.1. Microstructural and X-Ray Diffraction Analysis

3.1.1. Ti50Ni50 Coating. As the Ni and Ti powder particles were scanned by the laser beam along with the substrate, the molten particles reacted with each other and with substrate forming a melt pool. The melt pool rapidly solidified as the laser beam was moved across the substrate forming a clad track on the titanium substrate. Due to the rapid nonequilibrium solidification, the NiTi intermetallic compounds precipitated on the substrate. The possible exothermic chemical reactions and products of the powders are [21]



The microstructural images of the cross section of the deposited coatings were taken at different places of interest on the coating to understand the morphology of the microstructure and the distribution of nickel-titanium within the coating. Typical optical and SEM micrographs of the laser deposited coatings are shown in Figure 2.

Figure 2(a) shows the cross section of the laser deposited Ti50Ni50 coating on the Ti6Al4V substrate with a thickness of 550 μm and dilution rate of 6.3%. There were no cracks or pores observed within the coating, and most significantly good bonding between the substrate and the coating was achieved. SEM image of the coating showing distribution of the phases is presented in Figure 2(b). The contrast of the image indicates the presence of different phases. Elemental analysis performed on the coating revealed that the grey structures are a matrix consisting of TiNi phase and the light phases around the grain boundaries are TiNi₂ and TiNi₃ phases.

XRD results recorded for the Ti50Ni50 coating, in the range 2θ from 20° to 90°, are shown in Figure 3. There are four intermetallic phases identified in the coating, martensite NiTi (B19'), austenite NiTi (B2), NiTi₂, and Ni₃Ti, together with the main peaks of Ti. The elemental Ni peaks were not

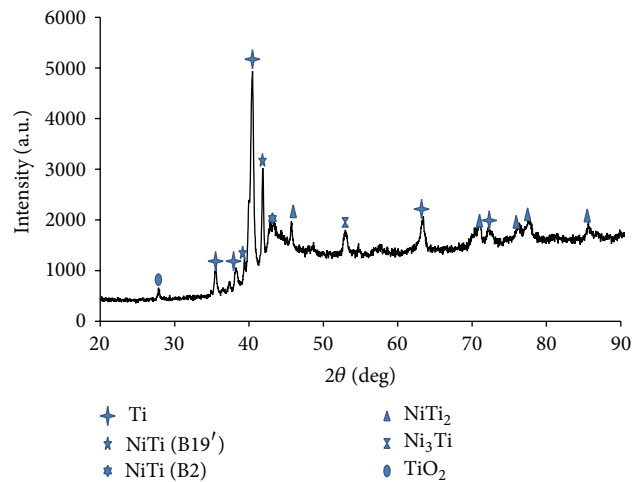


FIGURE 3: XRD patterns of Ti50Ni50 coating.

observed indicating that the Ni and Ti powders reacted with each other to form *in situ* Ni-Ti intermetallic phases. The existence of the Ti peaks is attributed to the abundance of Ti as the substrate and the added Ti powder. The main peaks for the NiTi (B19') phase occur at $2\theta = (38.25^\circ, 39.49^\circ, 41.85^\circ, 44.0^\circ, \text{ and } 45.2^\circ)$. A broad peak at $2\theta = 42.7^\circ$ is identified as the NiTi (B2) phase. The Ti-rich NiTi₂ phase occurs at $2\theta = (45.7^\circ, 70.98^\circ, 72.18^\circ, 76.63^\circ, 77.65^\circ, \text{ and } 85.65^\circ)$. The Ni-rich TiNi₃ phase has weak peaks at $2\theta = (43.7^\circ \text{ and } 52.96^\circ)$. The Ti peaks occur at $2\theta = (35^\circ, 38^\circ, 40^\circ, \text{ and } 63.44^\circ)$. Some traces of TiO₂ were detected at $2\theta = 27.96^\circ$. The volume of the martensite to austenite content in the coating could not be determined from the XRD data.

3.1.2. Ti55Ni45 Coating. Ti55Ni45 coatings deposited from processing parameters similarly as in the previous case are presented in Figure 4. Coatings with a layer thickness of 500 μm and dilution rate of 6.9% were obtained. The sample was slightly overetched in order to enhance the grain boundaries. Figure 4(a) shows the optical micrographs of the coating comprised of three phases, brown structures surrounded

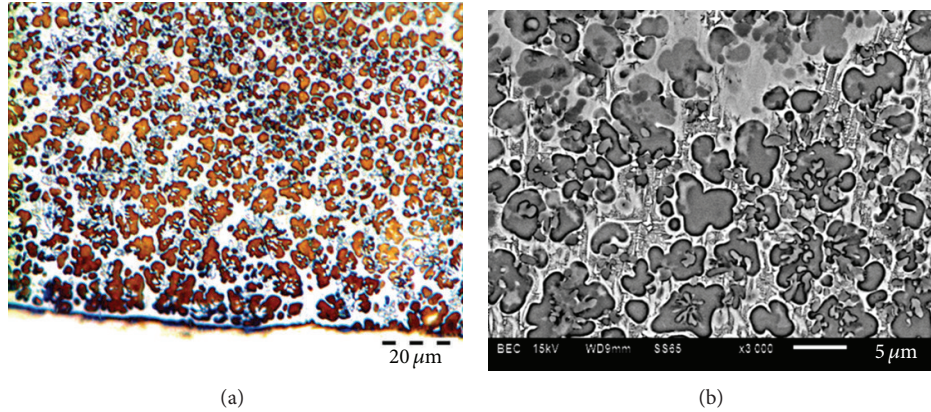


FIGURE 4: Micrographs of the laser deposited Ti55Ni45 coating; (a) optical image indicating different phases within the coating; (b) SEM image showing high magnification of the coating.

by bright/white structures and white phase occurring at the centre of the brown structures. The brown structures were identified as TiNi phase, with the bright/white identified as Ti₂Ni, while the white structures occurring mostly at the centre of the TiNi phase were identified as the Ti phase. It is observed that the Ti-rich phase occurs with two different morphologies, flower-like structures and spherical-like structures uniformly distributed within the coating. The occurrence of this phase in two morphologies was attributed to the excess Ti that did not react with the molten Ni causing it to remelt on its own forming Ti particles, while the flower-like structures are the titanium that fully reacted with nickel forming NiTi intermetallics. High magnification of SEM image of the coating is revealed in Figure 4(b) showing uniform distribution of the phases that formed during melting.

The XRD phase analysis of the Ti55Ni45 coating is presented in Figure 5; the results indicate that the coating consists of the NiTi (B19') martensite and NiTi (B2') austenite phases in accordance with the OM and SEM micrographs. The NiTi₂ phase is also detected along with the pure Ti peaks. For this coating no Ni-rich phases were detected by the XRD. The overall major peaks are NiTi martensite B19 and austenite B2, NiTi₂, and Ti as it is in abundance. There are no Ni₃Ti, Ni₄Ti₃, and TiO₂ traces observed as seen with other compositions.

3.1.3. Ti45Ni55 Coating. Optical micrograph and SEM image of the laser deposited Ni55Ti45 coating with a thickness of 550 μm and dilution rate of 6.5% are presented in Figure 6. The microstructure revealed good homogeneity and uniformity with equiaxed grains and a dendritic structure. The coating consists of dark brown structures reported to be NiTi and light white structures with a flower-like morphology identified as Ti-rich phase as observed in Figure 6(a). The light white structure occurring between the NiTi phases observed previously is also present; however, in this coating they appear as interconnected matrix throughout the coating. Figure 6(b) shows a SEM image at a high magnification indicating the interconnected matrix in the coating.

Figure 7 reports the XRD results recorded for the Ti45Ni55 laser coating in the 2θ range from 20° to 80°. Three

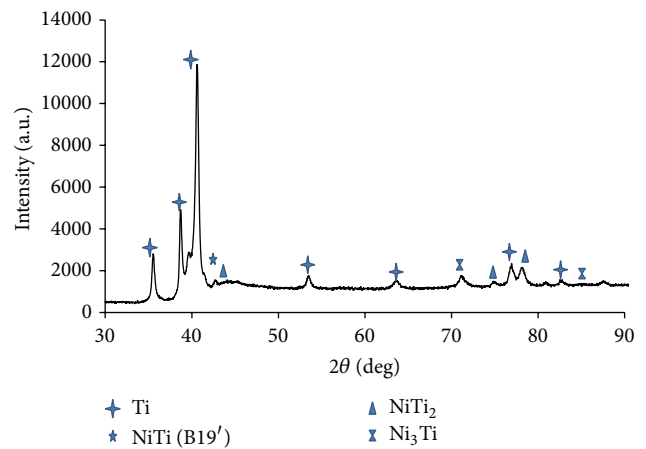


FIGURE 5: XRD patterns of Ti55Ni45 coating.

intermetallic phases NiTi austenite, NiTi₂, and Ni₃Ti were identified in the coating. The occurrence of the Ti peaks in abundance was attributed to the Ti6Al4V substrate that is used and the added Ti powder as seen in the previous results. Major peaks observed were Ni₃Ti and NiTi₂ with Ti overlapping each other at some peaks. Few peaks of Ni₃Ti phase occur at 2θ = (42.74°, 47.94°, and 82.97°). Weak peaks of NiTi₂ which overlapped with some Ti peaks occur at 2θ = (38.78°, 53.61°, 71.26°, and 77.06°), while Ti phase is occurring at 2θ = (36.62°, 38.78°, 40.67°, 53.61°, 63.7°, 71.26°, and 77.06°). NiTi austenite phase has weak peak at 2θ = (42.74°) and martensite phase was not observed, but some traces of TiO₂ were observed at 2θ = (44.08°).

3.2. Microhardness Analysis. Hardness profile across the depth of the NiTi metallic coating was measured by the Matsuzawa Seiki hardness tester at a load of 100 g, spacing of 50 μm, and dwell time of 15 seconds. Hardness profile of the deposited NiTi showing the hardness values in the coating, heat affected zone, and the substrate is presented in Figure 8. Experimental results indicate that the surface hardness of the laser deposited NiTi coatings had an increased hardness value compared to the parent material Ti-6Al-4V alloy. High

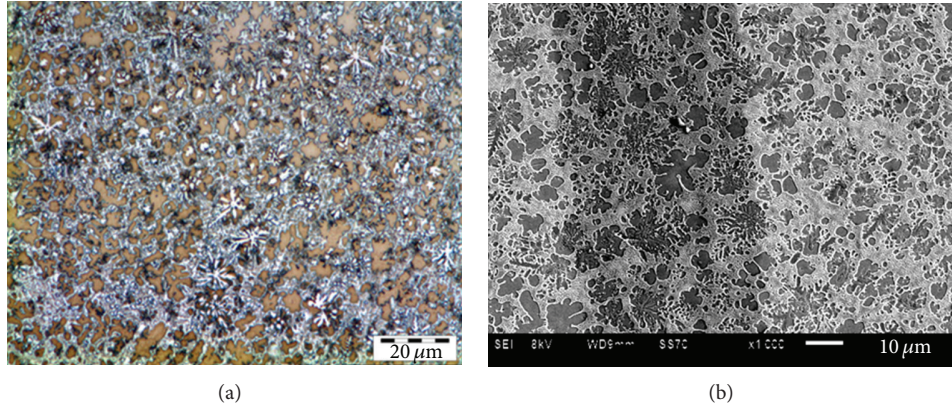


FIGURE 6: Micrographs of the laser deposited Ti45Ni55 coating; (a) optical image showing distribution of the phase in the coating; (b) SEM image showing a high magnification of the coating.

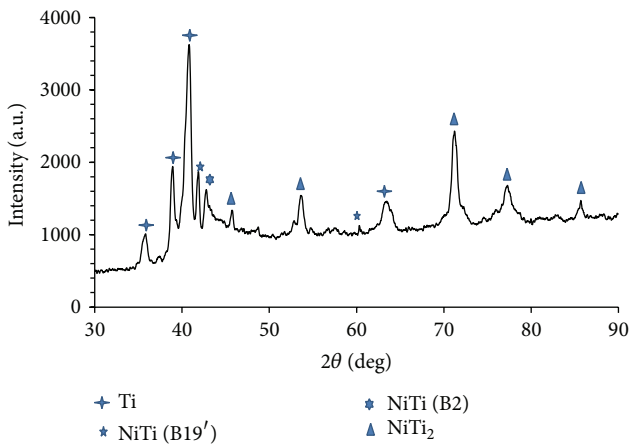


FIGURE 7: XRD patterns of Ti45Ni55 coating.

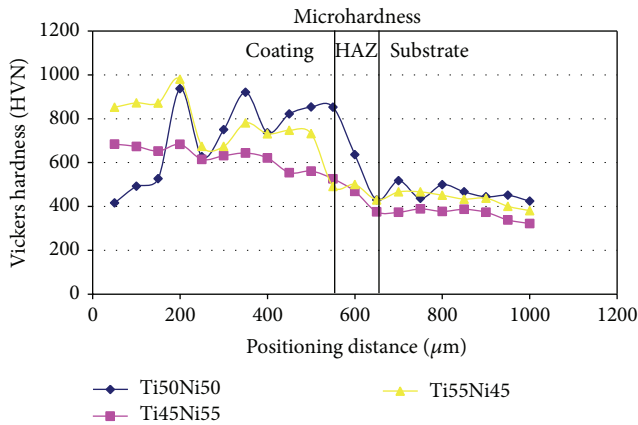
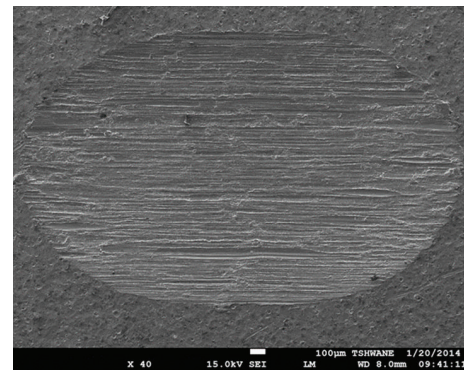
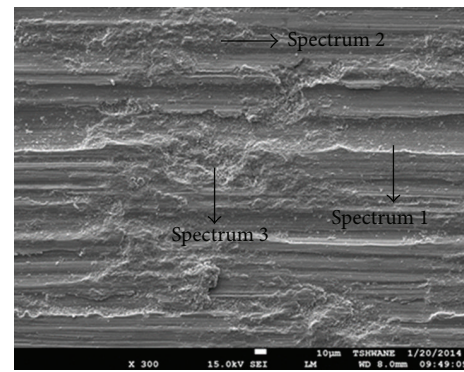


FIGURE 8: Microhardness measurement of laser deposited coatings.

hardness in the deposited layer is attributed to the formation of the fine grained microstructure produced during melting and formation of the hard intermetallic phases. The Ti55Ni45 coating had high hardness values compared to Ti45Ni55 and Ti50Ni50 coatings with the average value of 430 HV higher than that of Ti-6Al-4V (380 HV) substrate. The high hardness



(a)



Element (wt.%)	C	N	O	Al	Ti	V
Spectrum 1	2.63	-	-	7.51	88.44	1.42
Spectrum 2	1.60	1.01	14.34	3.26	75.37	3.15
Spectrum 3	3.52	1.83	28.82	4.73	58.86	2.24

(b)

FIGURE 9: Wear track of the Ti-6Al-4V substrate after sliding against a tungsten carbide ball.

displayed by the coating (742 HV) is a result of excessive amount of Ti elemental powder that was well dispersed within the coating resulting in increased volume of inert

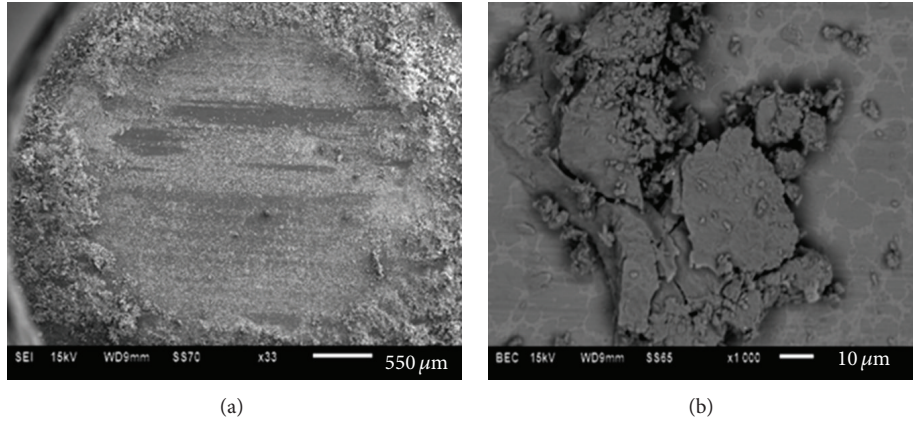


FIGURE 10: Wear track of the laser deposited Ni50Ti50 after sliding against a tungsten carbide ball.

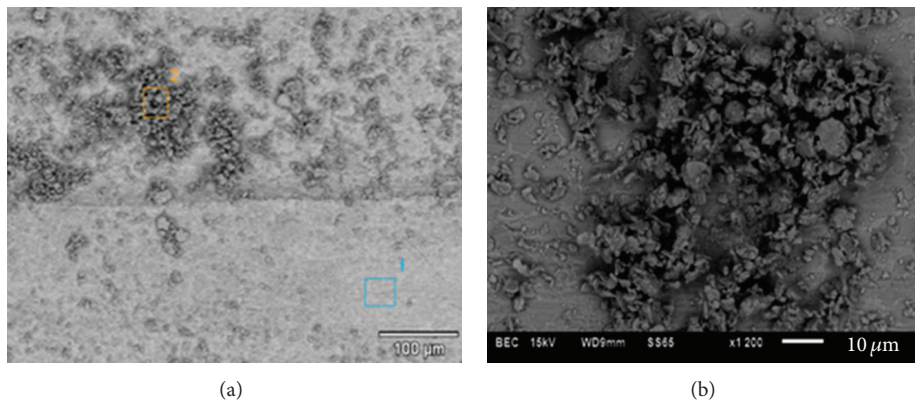


FIGURE 11: Wear track of the laser deposited Ni55Ti45 after sliding against a tungsten carbide ball.

secondary phase NiTi_2 known for high hardness but with brittle microstructure.

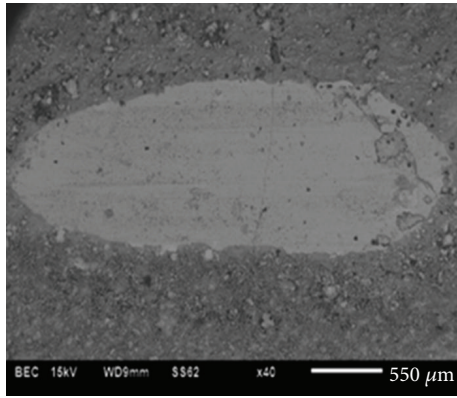
3.3. Wear Measurement. The deposited NiTi coatings were subjected to wear testing using a tungsten carbide (WC) ball at a load of 20 N for 17 minutes. Figure 9(a) displays the wear track of the Ti-6Al-4V substrate subjected to abrasive wear. The examined worn surface presented in Figure 9(b) indicated the presence of wear debris, large pits, and deep grooves on the surface of the material. Severe degree of plastic deformation was evident on the worn surface demonstrating that the mechanism is adhesion and abrasive wear.

The wear track of the laser deposited Ti50Ni50 coating is presented in Figure 10(a), showing ploughing mechanism experienced by the coating. Wear debris that detached from the surface stuck together forming cluster that rewelded to the surface of the coating. Alternatively, these clusters remain trapped between the sliding surfaces and spread onto wear track forming an oxide layer presented in Figure 10(b). Plastic deformation and shallow plough grooves on the worn surface of the NiTi show that the coating suffers from nonsevere abrasive and adhesive wear from the hard tungsten carbide ball.

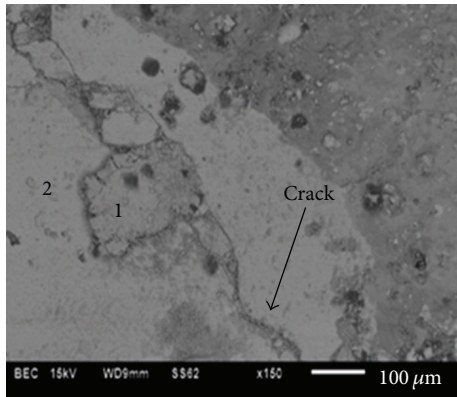
Figure 11(a) displays the wear track of the laser deposited Ni55Ti45 after sliding against a tungsten carbide ball for 17

minutes under dry conditions. It was observed that the wear debris formed consists of loose powder particles that were not compact with the surface of the coating as observed in Figure 11(b). Elemental analysis taken from wear debris demonstrates that the debris formed are a mixture of oxides from oxidation during wear and processing, carbon from the tungsten carbide ball, and nickel-titanium from the surface of the coating. The wear debris were smeared on the tribolayer and further oxidised due to effect of friction and mechanical cavitation as a result of contact between the ball and surface during sliding.

The SEM images of the laser deposited Ni45Ti55 coating after wear tests are presented Figure 12. It can be observed from Figure 12(a) that the debris formed in the coating are in small quantity compared to the coatings fabricated with a composition of Ni50Ti50 and Ni55Ti45. As a result of high content of Ti in the Ni45Ti55, an increased volume of Ti dendrite phase is produced. The Ti dendrites with a hard phase effectively carry the load, because they are formed *in situ*. The interfacial bonding between the NiTi matrix and the Ti dendrites tends to be stronger, and hence the clad layers exhibit better wear resistance than the other coatings. However, cracks expansion on the oxide layer which is believed to be the brittle NiTi_2 phase was observed in Figure 12(b). The formation of oxide layer and subsequent



(a)



(b)

Element (wt.%)	Ti	Ni	Al	C	O	N
Area 1	58.00	16.60	2.22	4.88	12.09	3.78
Area 2	73.85	20.57	1.61	1.64	0.00	0.00

FIGURE 12: Wear track of the laser deposited Ni45Ti55 after sliding against a tungsten carbide ball under dry conditions.

compacting as a solid lubricant have been reported to cause a transition from a more to a less severe wear. The results obtained in the analysis of the wear track and the debris from the three coatings are almost the same, and hence it can be concluded that the dominant wear mechanisms (oxidation and abrasive) are the same in all coatings. In comparison with Ti6Al4V alloy, the deposited NiTi coatings presented less degree of deformation. Their worn surfaces clearly signify better wear resistance under dry sliding conditions and room temperature.

From the results obtained in graph presented in Figure 13, low wear rate is notable in coatings fabricated from the Ti55Ni45 composition; these are attributed to the high hardness values and the NiTi (B2), NiTi₂, and Ti phases formed during processing. NiTi B2' experience elastic deformation stress induced martensitic transformation leading to pseudoplastic effect which is accommodated deformation during wear; hence less wear is experienced by the coating. These were not achievable in Ti50Ni50 coating as a result of the high volume of NiTi (B19'). The Ti45Ni55 presented

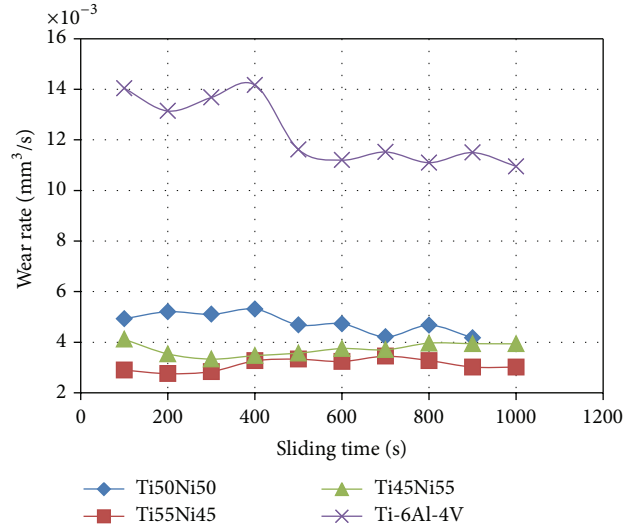


FIGURE 13: Wear rate analysis of laser deposited coating.

better wear rate compared to the former due to presence of B2 and an increased volume of NiTi₂ phase. These is a result of the combination of intermetallic properties of NiTi₂ (high hardness and good ductility) and excellent ductility and toughness of NiTi.

4. Conclusions

Surface modification of Ti6Al4 was successfully achieved by fabricating NiTi coatings using laser metal deposition. The coatings produced were metallurgically bonded to the surface without defects such as pores and cracks with minimal dilution between the substrate and the coating. The microstructure of NiTi/Ti6AlV4 coating produced consisted of intermetallic TiNi-NiTi₂ alloy. The highest hardness value 742 HV was displayed by Ti55Ni45 coating, with an average value of 430 HV higher than that of Ti6Al4V (380 HV) substrate. The wear resistance was significantly improved with more than five orders of magnitude than that of the substrate. Enhancement of the wear resistance of the coating was achieved as a result of the combination of high hardness, excellent ductility, and toughness exhibited by NiTi. Wear mechanism of the NiTi coating under dry sliding condition is governed by nonsevere abrasive and adhesive wear. Ti dendrites formed during solidification played a major role in improving the properties of the coating as it acted as the reinforcement, strengthening the deposited coating.

Conflict of Interests

The authors declare that there is no conflict of interests regarding the publication of this paper.

Acknowledgments

This material is based on work supported financially by the National Research Foundation. The National Laser Centre,

CSIR, Pretoria, is appreciated for laser facility and financial support. Appreciation goes to Tshwane University of Technology and Mr. Lucas Mokwena.

References

- [1] J. J. Polmear, "Titanium alloys," in *Light Alloys*, Edward Arnold, London, UK, 1981.
- [2] Y. S. Tian, C. Z. Chen, D. Y. Wang, and T. Q. Lei, "Laser surface modification of titanium alloys—a review," *Surface Review and Letters*, vol. 12, no. 1, article 123, 2005.
- [3] M. J. Dutta and I. Manna, "Laser material processing," *International Materials Reviews*, vol. 56, no. 5-6, pp. 341–388, 2011.
- [4] J. J. Dai and S. Q. Hou, "Laser gas nitriding of titanium and titanium alloys," *Surface Review and Letters*, vol. 16, no. 6, pp. 789–796, 2009.
- [5] A. P. I. Popoola, S. L. Pityana, and O. M. Popoola, "Laser deposition of (Cu + Mo) alloying reinforcements on AA1200 substrate for corrosion improvement," *International Journal of Electrochemical Science*, vol. 6, no. 10, pp. 5038–5051, 2011.
- [6] M. Rakhes, E. Koroleva, and Z. Liu, "Improvement of corrosion performance of HVOF MMC coatings by laser surface treatment," *Surface Engineering*, vol. 27, no. 10, pp. 729–733, 2011.
- [7] Y. Sun and M. Hao, "Statistical analysis and optimization of process parameters in Ti6Al4V laser cladding using Nd:YAG laser," *Optics and Lasers in Engineering*, vol. 50, no. 7, pp. 985–995, 2012.
- [8] E. Yoyserkani, A. Khajerour, and S. Corbin, *Laser Cladding*, CRC Press, Washington, DC, USA, 2005.
- [9] S. Sun, Y. Durandet, and M. Brandt, "Parametric investigation of pulsed Nd:YAG laser cladding of stellite 6 on stainless steel," *Surface and Coatings Technology*, vol. 194, no. 2-3, pp. 225–231, 2005.
- [10] U. K. Mudali, R. Kaul, S. Ningshen et al., "Influence of laser surface alloying with chromium and nickel on corrosion resistance of type 3041 stainless steel," *Materials Science and Technology*, vol. 22, no. 10, pp. 1185–1192, 2006.
- [11] H. Hiraga, T. Inoue, H. Shimura, and A. Matsunawa, "Cavitation erosion mechanism of NiTi coatings made by laser plasma hybrid spraying," *Wear*, vol. 231, no. 2, pp. 272–278, 1999.
- [12] M. Salehi, F. Karimzadeh, and A. Tahvilian, "Formation of Ti-Ni intermetallic coatings on carbon tool steel by a duplex process," *Surface and Coatings Technology*, vol. 148, no. 1, pp. 55–60, 2001.
- [13] K. Allafi, X. Ren, and G. Eggeler, "The mechanism of multistage martensitic transformations in aged Ni-rich NiTi shape memory alloys," *Acta Materialia*, vol. 50, no. 4, pp. 793–803, 2002.
- [14] J. C. Schauer and J. Winter, "Plasma deposition of elastic wear resistant Si-C coatings on nickel-titanium for biomedical applications," *Journal of Applied Physics*, vol. 103, no. 11, Article ID 113302, 2008.
- [15] L. Gerke, J. Stella, J. C. Schauer, M. Pohl, and J. Winter, "Cavitation erosion resistance of a-C:H coatings produced by PECVD on stainless steel and NiTi substrates," *Surface and Coatings Technology*, vol. 204, no. 21-22, pp. 3418–3424, 2010.
- [16] T. Abubakar, M. Rahman, D. P. Dowling, J. Stokes, and M. S. J. Hashmi, "Adhesion performance of TiN coating with amorphous NiTi alloy interlayer onto 316L stainless biosteel deposited by sputtering process," *Surface Engineering*, vol. 26, no. 7, pp. 499–505, 2010.
- [17] M. Bram, A. Ahmad-Khanlou, H. P. Buchkremer, and D. Stöver, "Vacuum plasma spraying of NiTi protection layers," *Materials Letters*, vol. 57, no. 3, pp. 647–651, 2002.
- [18] S. Ozel, B. Kurt, I. Somunkiran, and N. Orhan, "Microstructural characteristic of NiTi coating on stainless steel by plasma transferred arc process," *Surface and Coatings Technology*, vol. 202, no. 15, pp. 3633–3637, 2008.
- [19] C. van der Eijk, H. Fostervoll, Z. K. Sallom, and O. M. Akselsen, "Plasma welding of NiTi to NiTi, stainless steel and hastelloy C276," in *Proceedings of the ASM Materials Solutions Conference*, pp. 125–129, Pittsburgh, Pa, USA, 2003.
- [20] T. B. Massalski, H. Okamoto, P. R. Subramanian, and L. Kacprzak, *Binary Alloy Phase Diagrams*, vol. 3, ASM International, Materials Park, Ohio, USA, 2nd edition, 1990.
- [21] C. Zhang, Y. Yang, and W. Xu, "In situ synthesis of titanium-nickel intermetallic compounds layer and TiN coating by laser cladding," *OME Information*, no. 5, pp. 33–39, 2006.

Research Article

Influence of Ultrafine Natural Steatite Powder on Setting Time and Strength Development of Cement

K. Sudalaimani¹ and M. Shanmugasundaram²

¹ Department of Civil Engineering, Thiagarajar College of Engineering, Thiruparankundram, Madurai, Tamilnadu 625015, India

² Department of Civil Engineering, Vickram College of Engineering, Madurai, Tamilnadu 630561, India

Correspondence should be addressed to M. Shanmugasundaram; shanmugaresearch@gmail.com

Received 16 November 2013; Revised 29 January 2014; Accepted 9 February 2014; Published 11 March 2014

Academic Editor: Mohammad Mahroof-Tahir

Copyright © 2014 K. Sudalaimani and M. Shanmugasundaram. This is an open access article distributed under the Creative Commons Attribution License, which permits unrestricted use, distribution, and reproduction in any medium, provided the original work is properly cited.

This paper deals with the setting time and pozzolanic activity of cement when ultra fine natural steatite powder (UFNSP) is used as replacement for cement. Initial setting time, final setting time, and mortar cube strength were studied, due to the replacement of ultra fine natural steatite powder with cement at 5%, 10%, 15%, 20%, and 25% by mass of cement. The setting time of fresh cement-binder paste and compressive strength of mortar cubes are observed. Scanning electron microscopy (SEM) and X-ray diffraction (XRD) were applied to investigate the microstructural behaviour and chemical element distribution inside cement-binder matrix. Results indicate that the length of dormant period is shortened. The replacement of ultra fine natural steatite powder with cement reduces initial setting time, and final setting time and increases mortar cube compressive strength.

1. Introduction

Steatite is a type of metamorphic rock, largely composed of talc ore, rich in magnesium. It is composed of hydrated magnesium silicate: $Mg_3Si_4O_{10}(OH)_2$. Steatite is the softest known mineral and listed as 1 on the Mohs hardness scale. It is already used in paint industry, particularly in marine paints and protective coatings. This is used in ceramics due to its high resistivity, very low dielectric loss factor, and good mechanical strength. Addition of steatite powder increases the viscosity and mechanical properties of feed stock. The thermal properties of steatite are also good [1]. Massive steatite cut into panels is used for switchboards, for acid proof tabletops in laboratory, laundry, and kitchen sinks, and in tubs and tanks, as well as for lining alkali tanks in paper industry. Due to its high melting point (1630°C) [2], steatite can be used in refractory and fire places. It is also quite useful in sculpturing. When fabricated by a combined method of high energy ball milling, cold pressing, and sintering, it improves thermal properties of ceramics [3, 4]. Cement mortars prepared with steatite particles have been investigated

for restoration of sculptures and other craftworks. It was observed that the highest compressive strength (43 MPa) and lowest apparent porosity (0.19%) are achieved when steatite particles are coarser (ranging from 1.41 mm to 0.42 mm), and 40% of polymeric phase is employed [5]. A special cement-based mortar containing additions of fine powder waste from mineral extraction of steatite has been developed in Brazil, as a composite material for restoration of steatite elements [6]. The steatite is mostly used in electrotechnics. Stabilization of protoenstatite in steatite body is achievable by the development of small crystals [7]. Improper selection of parameters led to undesired problems such as separation of the powder-binder mixture and formation of collapses and cracks on the structure of the moulded parts. The optimum moulding parameters of the feed stocks for the zigzag shaped mold are determined to be at an injection pressure of 80 to 140 MPa at barrel temperature of 190 to 230°C [8]. When a property of powder injection moulded steatites is investigated, sintered at 1300°C for 4 hours, a theoretical density of 98%-99% is achieved. Three-point bending and tensile test was performed on the samples sintered at 1200°C to 1300°C. The maximum

three-point bending and tensile strength values are found to be 154 MPa and 47 Mpa, respectively [9]. Indian steatite, mined in Rajasthan and Andhra Pradesh, is comparable with the best quality available in other countries. The steatite mined in India, with more than 92% brightness, less than 1% Fe_2O_3 , and less than 1.5% CaCO_3 , is preferred for exports [2]. Indian steatite is considered to be the second best in the world next to "Italian steatite." The UFSP used in this experiment develops M-S-H gel; hence the comparative study of C-S-H and M-S-H is vital. On account of the basic structural difference between the two gel types, M-S-H and C-S-H are essentially immiscible [10]. Magnesium hydroxide ($\text{Mg}(\text{OH})_2$ aka brucite) is a good starting point for the development of low pH cements. pH value of excess brucite in equilibrium with water is calculated to be around pH 10.5 [11]. Hence, in principle, cement based on the hydration of MgO powder, calcined at low temperature to ensure fast hydration, should yield the desirable pH. According to Zhang et al. [11] high MgO contents do not affect the pH, whereas high silica fume content results in a pH closer to 9.5. Both MgO and silica fume composition have potential applications for the encapsulation of wastes containing heavy metals [11]. In the present research work, effect of UFNSP powder on setting time and strength development on cement is investigated.

2. Materials and Experimental Methods

2.1. Raw Materials

Cement. Ordinary portland cement conforming to IS: 8112-1989 (Indian Standard Designation, IS: 8112-1989) is used for mortar mixtures; the cement used in this study belongs to type I of ASTM. The physical and chemical properties are given in Table 1.

Fine Aggregates. Standard natural sand having hard, clean, strong, durable, uncoated particles and meeting the requirements of the specifications (ASTM C144-11) with specific gravity of 2.65 is used as fine aggregate.

Water. In the present investigation, potable water is used for mixing and curing.

Mineral Admixture. UFNSP obtained from UltraFine Mineral Pvt. Ltd., India, is used as natural admixture. UFNSP is manufactured by using high quality crushers and superfine grinders. UFNSP is finer than cement. The physical and chemical properties are given in Table 1.

2.2. Consistency of Cement. The basic aim is to find out the water content required to produce a cement paste of standard consistency as specified by the IS: 4031 (Part 4)-1988. The principle is that standard consistency of cement is that consistency at which the Vicat plunger penetrates to a point 5–7 mm from the bottom of Vicat apparatus, conforming to IS: 5513-1976. Approximately 400 g of cement is mixed with a weighed quantity of water. The time of gauging should be between 3 and 5 minutes. Fill the Vicat mould with paste and level it with a trowel. Lower the plunger gently till it

touches the cement surface. Then release the plunger to sink into the paste. Note the reading on the gauge and repeat the above procedure taking fresh samples of cement and different quantities of water until the reading on the gauge is 5 to 7 mm.

2.3. Initial and Final Setting Time (IST and FST). How to calculate the initial and final setting time as per IS: 4031 (Part 5)-1988 by Vicat apparatus conforming to IS: 5513-1976? Prepare a cement paste by gauging the cement with 0.85 times the water required to give a paste of standard consistency. Start a stopwatch the moment water is added to the cement. Fill the Vicat mould completely with the cement paste gauged as above. With the mould resting on a nonporous plate, smooth off the surface of the paste making it level with the top of the mould. The cement block thus prepared in the mould is the test block.

Determining Initial Setting Time (IST). Place the test block under the rod bearing the needle. Lower the needle gently in order to make contact with the surface of the cement paste. Release quickly, allowing it to penetrate the test block. Repeat the procedure till the needle fails to pierce the test block to a point 5.0 ± 0.5 mm measured from the bottom of the mould. Initial setting time is the period elapsing when water is added to the cement and the needle fails to pierce the test block by 5.0 ± 0.5 mm measured from the bottom of the mould.

Final Setting Time (FST). Replace the above needle by the one with an annular attachment. The cement is considered to finally set, when the gentle application of the needle makes an impression therein, while the attachment fails to do so. Final setting time is the period elapsing when water is added and the needle makes an impression on the surface of the test block.

2.4. Compressive Strength on Mortar Cubes. Mortar cubes used in this investigation were $70.6 \text{ mm} \times 70.6 \text{ mm} \times 70.6 \text{ mm}$ conforming to IS 10080-1982. The specimens were prepared in ratio of cement : sand as 1:3 and W/B ratio as 0.47. These specimens are cast in three layers, in accordance to IS 10080-1982. Each layer is well compacted by a tamping rod of 12 mm diameter. After the compaction the top surface is leveled using a trowel and left for 24 hours to dry in room temperature of 28°C with 60% humidity. On the next day, at room temperature of 29°C and 54% humidity, the mortar cubes are kept inside a curing tank filled with potable water. The specimens are tested with a 2000 kN capacity hydraulic compression testing machine, as per IS: 4031-1982 (Part 6). Altogether 108 mortar cubes (6 Mix IDs \times 18 specimens) were cast and were tested for compressive strength.

2.5. Scanning Electron Microscopy and X-Ray Diffraction Studies. The specimen is studied by Scanning Electron Microscopy and XRD Patterns. Samples for scanning electron microscopy (SEM) analysis are taken near the surface (0–1 mm depth) of specimens. Micro structural studies utilized SEM (HITACHI S-3000H, Japan) equipped with EDAX analyzer for micro structural observations of the surfaces, which

TABLE 1: Physical and chemical properties of cement and UFNSP.

	Cement	UFNSP
Physical properties		
Blaine surface area (m ² /Kg)	380	750
Particle mean dia. (μ m)	<32	<5
Density	3.1	2.7
Loss of ignition	2%	3.33%
Chemical properties		
SiO ₂	23%	62.67%
Al ₂ O ₃	4.20%	0.24%
MgO	0.20%	33.26%
Fe ₂ O ₃	1.20%	0.30%
CaO	63%	0.20%

is coated with evaporated copper for examination. SEM analyses is done at a maximum magnification of 20,000 x with energy 15 keV and a high resolution of 3.5 nm. For this analysis, samples of size 10 mm cubes are cut with a saw cutter on 28th day. The XRD analysis is carried out with a Siemens D-5000 X-ray diffractometer with Cu K-beta radiation and 2θ scanning with a step size of 0.02° and a measuring time of 10.00 Deg/minute. A voltage of 40 kV and current of 15 Ma is used. Samples are collected from the cubes after 28 days of water curing and powdered in ball mills to pass through the sieve size of 90μ .

3. Results and Discussions

3.1. Consistency of Cement. From Table 2 the consistency of binder material is observed. The consistency is found to continuously increase as the percentage replacement of cement with UFNSP increases. The water consistency increases for C5, C10, C15, C20 and C25 at 4%, 5%, 7%, 10%, 13% when compared with C0. This may be due to higher fineness of UFNSP and higher water absorption property.

3.2. Setting Time. From the experimental design, the maximum, minimum and average values of IST and FST are shown in Table 2, together with the main effects and UFNSP interactions. The values are reported as relative values with respect to ordinary Portland cement paste, 30 and 360 minutes for IST and FST respectively. The IST for C5, C10, C15 and C20 decreases by 5 minutes, 10 minutes, 10 minutes, and 5 minutes respectively and for C25 IST increases by 10 minutes when compared with C0 mix. Similarly the FST for C5, C10, C15 and C20 decreases by 30 minutes, 60 minutes, 60 minutes, and 30 minutes respectively and for C25 FST increases by 90 minutes when compared with C0 mix. From the above results it is observed that IST and FST decreases when percentage of UFNSP replacement increases up to 20%, but there is a sudden increase in IST and FST on C25 specimen which may be due to excess UFNSP.

3.3. Compressive Strength of Mortar Cubes. The strength attained during 3 days, 7 days and 28 days on mortar cubes are

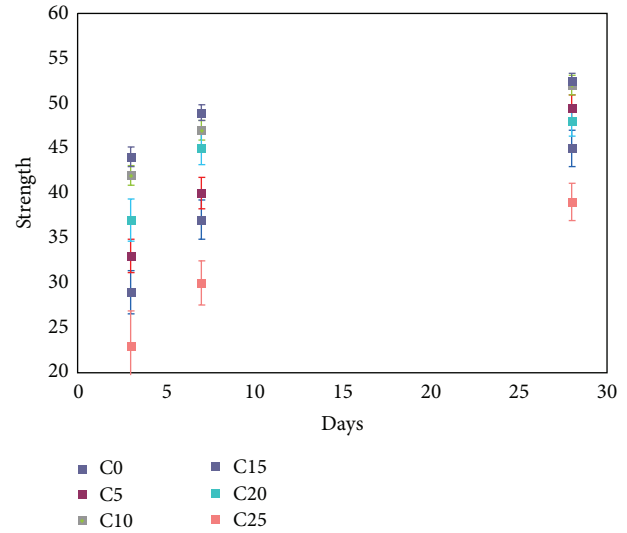


FIGURE 1: Scatter plot on strength of mortar cubes with standard deviation.

experimentally tested for 6 specimens on each age and their average results are shown in Table 3 and Figure 1. The strength of mortar cubes of C5, C10, C15, C20 and C25 are compared with C0 mix. The compressive strength on 3 days for C5, C10, C15 and C20 increases by 13.8%, 44.8%, 51.7% and 27.5%. The strength of C25 decreases by 20.7%. On the 7th day for C5, C10, C15 and C20 increase by 8.1%, 27.02%, 32.43% and 21.6%. The strength of C25 decreases by 18.9% and on the 28th day for C5, C10, C15 and C20 increases by 10%, 15.6%, 16.7% and 6.7%. The strength of C25 decreases by 13.3%. Thus the above results show the Mix C5, C10, C15 has a considerable increase in terms of strength and also the strength is easily attained on its early ages like 3 days and 7 days. Data on the variation in compressive strength of mortar cubes is shown in Table 3 and Figure 1. The Standard Deviation (SD) and Coefficient of Variation (CO-VAR) of the compressive strength on 3 days, 7 days and 28 days shows decrease in SD and CO-VAR with increase in ages. The maximum SD is observed in C25, the lowest SD is observed at C10 and C15. The SD for C0 and C20 shows almost equal values. C5 shows lesser SD than C0 but more than C10 on all age. The CO-VAR fell from maximum value on 3 days to the lowest on 28 days for all specimens. The data shows that C15 is the specimen having Lowest SD and CO-VAR, with maximum strength, which also ensures that C15 mix is the most reliable of all mix IDs. The C25 specimens have highest SD and CO-VAR and lowest strength and are identified as the inferior specimen of all other specimen.

3.4. Microstructural Analysis. The results obtained in SEM and XRD analysis are shown in Figures 2 and 3.

The analysis shows that the best results are obtained from adding 15% of UFNSP. The images obtained in SEM are shown in Figure 2. Figure 2(a) shows the micrograph of C0; it consists of fine particles, which appear to have agglomerated into larger groups of particles. Figure 2(b) shows the micrograph of C5 specimen; the extent of coverage is substantial but not

TABLE 2: Consistency, IST, and FST.

S. number	Mix IDs	% replacement of UFNSP	% consistency of water for binder	IST in minutes	FST in minutes
1	C0	0	24	30	360
2	C5	5	28	25	330
3	C10	10	29	20	300
4	C15	15	31	20	300
5	C20	20	34	25	330
6	C25	25	37	40	450

TABLE 3: Compressive strength of mortar cubes.

S. number	Mix IDs	3-day strength in MPa	SD in MPa	CO-VAR in %	7-day strength in MPa	SD in MPa	CO-VAR in %	28-day strength in MPa	SD in MPa	CO-VAR in %
1	C0	29.00	2.39	8.23	37.00	2.19	5.92	45.00	2.00	4.44
2	C5	33.00	1.90	5.75	40.00	1.79	4.47	49.50	1.38	2.78
3	C10	42.00	1.10	2.61	47.00	1.10	2.33	52.00	1.10	2.11
4	C15	44.00	1.10	2.49	49.00	0.89	1.83	52.50	0.84	1.59
5	C20	37.00	2.37	6.40	45.00	1.79	3.98	48.00	1.67	3.49
6	C25	23.00	3.90	16.95	30.00	2.45	8.16	39.00	2.10	5.38

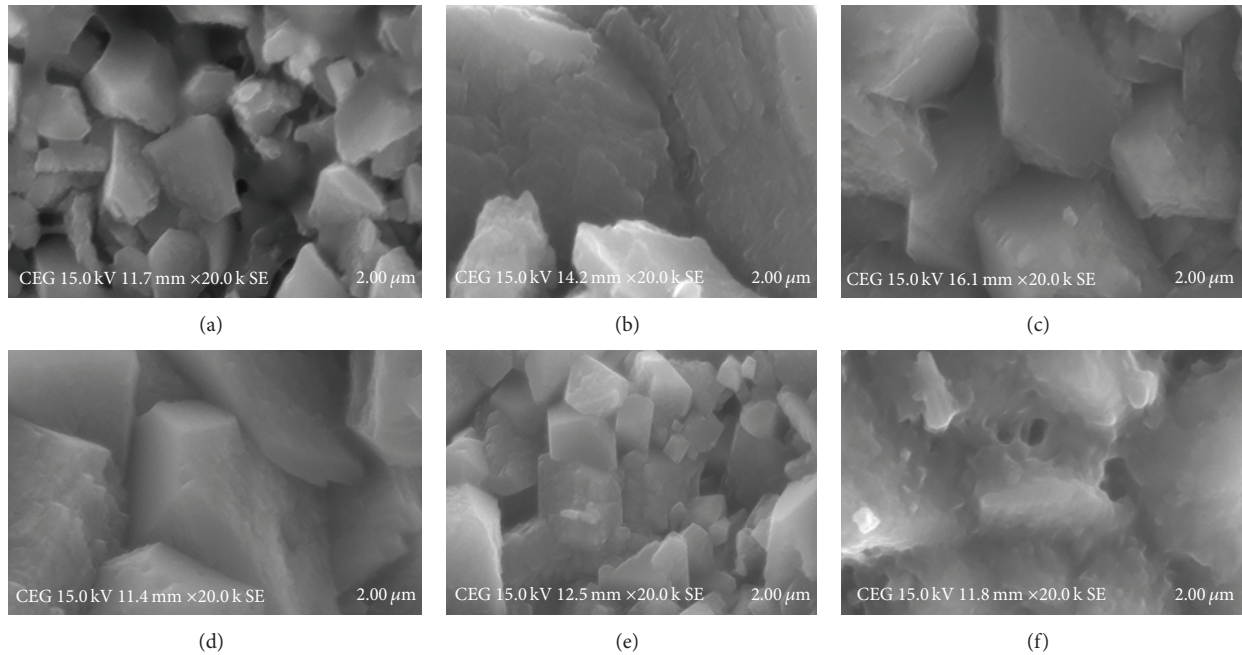


FIGURE 2: SEM images of specimens with 20000 x magnification: (a) C0 specimen, (b) C5 specimen, (c) C10 specimen, (d) C15 specimen, (e) C20 specimen, and (f) C25 specimen.

enough material has formed to create a continuous film on the surface of the particle. Some regions show the traces of no hydration products and absence of deposition of hydration products. Figures 2(c) and 2(d) show the micrograph of C10 and C15 specimens, respectively. This shows that due to the abundance of the hydration products the appearance has changed from small isolated particles to tangled web of flake-like crystals. The hydration products consist of a mixture of phases as is typical for portland cement. For

example, portlandite is visible at some regions, intermixed with reticulated C-S-H (or) M-S-H gel. Figure 2(e) shows the micrograph of C20; it is similar to that of C0; but there are no empty regions without hydration products, and hence this C20 specimen mechanical behaviour is similar to that of C0. Figure 2(f) shows the micrograph of C25 specimen; this shows that the flake-like crystals start disappearing and form into cloudy disintegrated form. This also confirms the loss in bonding effect. A study on microstructure of samples

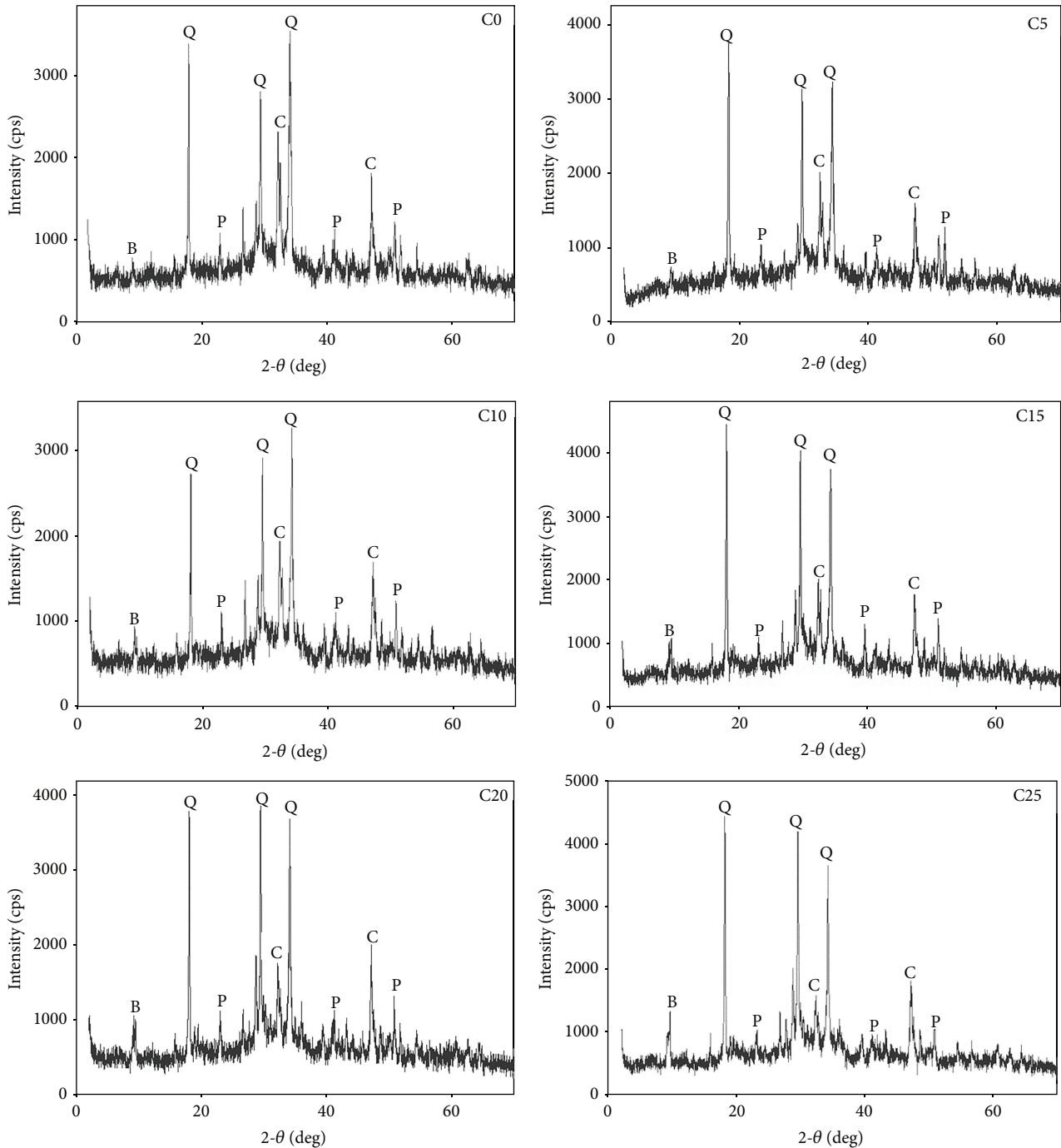


FIGURE 3: XRD patterns of C0, C5, C10, C15, C20, and C25 mortars. Q: quartz; C: calcite; P: portlandite; B: brucite.

C0, C5, C10, C15, C20, and C25 is made. The results show that the UFNSP particles have been covered in a continuous pattern for C5, C10, and C15 specimens and pattern of very small particles is identified for C20 and C25 specimens. The patterns for C20 specimen are similar to C0 specimen. The C25 specimen shows lack of bonding and formation of independent particles without bond, which may be the cause of reduction in strength.

Figure 3 shows the X-ray diffractograms of C0, C5, C10, C15, C20, and C25 mortars, respectively. The main compounds are quartz (SiO_2), calcite (CaCO_3), portlandite (Ca(OH)_2), and brucite (Mg(OH)_2). The X-ray diffractograms show increase in quartz when UFNSP is added. The calcite is similar in all specimens. The intensity of brucite increases as percentage replacement of UFNSP increases. The peaks for all specimens indicate the presence of quartz, calcite, and portlandite and

very small quantity of brucite. The intensity of portlandite peak is slightly higher in C10 and C15 when compared to other specimens.

The increase in C15 strength is due to the right combination of portlandite, calcite, and brucite. The SEM image and X-ray diffractograms (Figures 2(d) and 3) of C15 show the wider presence of dense portlandite and brucite which supports faster hydration reaction. The reduction in calcite leads to decrease in carbonation process. Hence maximum strength is attained in C15. Figure 3 shows that the intensity of portlandite is very low for C25. The increase of brucite ($\text{Mg}(\text{OH})_2$) in combination with reduction of portlandite leads to the conclusion that portlandite most probably reacted with magnesium. The very low solubility of brucite favours the consumption of calcium hydroxide ($\text{Ca}(\text{OH})_2$) [12]. The reduction in strength of C25 specimen is attributed to the pozzolanic activity and pore structure. Since replacement of UFNSP reduces the content of portlandite, the hydration reaction and pozzolanic activity decreases. Hence the strength contribution from this process is lower than C0.

4. Conclusion

From the present study it can be concluded that replacement of UFNSP with cement results in decrease of IST and FST, but the consistency of binding material increases. This shows the increase in requirement of water to produce cement paste. The compressive strength of mortar cube increases during its early stages. The maximum compressive strength in 3, 7, and 28 days is observed at C15. The improvement in strength in C5, C10, C15, and C20 is nominal at all stages and normalizes in 28 days. The C25 shows decrease in strength and increase in IST and FST. It is also observed that replacing UFNSP with cement results in improvement of microstructure of cement mortar. The C5, C10, and C15 specimens show denser microstructural bond when compared to other specimens. The availability of denser hydration product (portlandite) in C15 specimen is identified. The C20 specimen shows micro structural similarity to control specimen. The reduction in strength of C25 specimen is attributed to the pozzolanic activity and pore structure. C25 shows disintegrated microstructure and very low intensity of portlandite. From all the above discussion it is concluded that the suitable UFNSP replacement percentage should not exceed 20%.

Conflict of Interests

The authors declare that there is no conflict of interests regarding the publication of this paper.

Acknowledgments

The authors of this paper express their gratitude to the management of Thiagarajar College of Engineering (TCE). The authors wish to express their thanks to the department for facilitating this work.

References

- [1] C. Karatas, A. Kocer, H. I. Ünal, and S. Saritas, "Rheological properties of feedstocks prepared with steatite powder and polyethylene-based thermoplastic binders," *Journal of Materials Processing Technology*, vol. 152, no. 1, pp. 77–83, 2004.
- [2] Ministry of mines, Indian Bureau of Mines, *Indian Mineral Year Book*, 2011.
- [3] H. Gökçe, D. Ağaogullari, M. L. Öveçoğlu, I. Duman, and T. Boyraz, "Characterization of microstructural and thermal properties of steatite/cordierite ceramics prepared by using natural raw materials," *Journal of the European Ceramic Society*, vol. 31, no. 14, pp. 2741–2747, 2011.
- [4] P. Rohan, K. Neufuss, J. Matějček, J. Dubský, L. Prchlík, and C. Holzgartner, "Thermal and mechanical properties of cordierite, mullite and steatite produced by plasma spraying," *Ceramics International*, vol. 30, no. 4, pp. 597–603, 2004.
- [5] F. P. Cota, R. A. A. Alves, T. H. Panzera, K. Strecker, A. L. Christoforo, and P. H. R. Borges, "Physical properties and microstructure of ceramic-polymer composites for restoration works," *Materials Science and Engineering A*, vol. 531, pp. 28–34, 2012.
- [6] T. H. Panzera, K. Strecker, J. D. S. Miranda, A. L. Christoforo, and P. H. R. Borges, "Cement—steatite composites reinforced with carbon fibres: an alternative for restoration of Brazilian historical buildings," *Materials Research*, vol. 14, no. 1, pp. 118–123, 2011.
- [7] W. Mielcarek, D. Nowak-Woźny, and K. Prociów, "Correlation between MgSiO_3 phases and mechanical durability of steatite ceramics," *Journal of the European Ceramic Society*, vol. 24, no. 15–16, pp. 3817–3821, 2004.
- [8] S. Erguney, C. Karatas, H. I. Unal, and S. Saritas, "Investigation of the moldability parameters of PEG based steatite feedstocks by powder injection molding," *International Polymer Processing*, vol. 26, no. 2, pp. 143–149, 2011.
- [9] L. Urtekin, I. Uslan, and B. Tuc, "Investigation of properties of powder injection-molded steatites," *Journal of Materials Engineering and Performance*, vol. 21, no. 3, pp. 358–365, 2012.
- [10] D. R. M. Brew and F. P. Glasser, "Synthesis and characterisation of magnesium silicate hydrate gels," *Cement and Concrete Research*, vol. 35, no. 1, pp. 85–98, 2005.
- [11] T. Zhang, C. R. Cheeseman, and L. J. Vandeperre, "Development of low pH cement systems forming magnesium silicate hydrate (M-S-H)," *Cement and Concrete Research*, vol. 41, no. 4, pp. 439–442, 2011.
- [12] Y. Senhadji, M. Mouli, H. Khelafi, and A. S. Benosman, "Sulfate attack of Algerian cement-based material with crushed limestone filler cured at different temperatures," *Turkish Journal of Engineering and Environmental Sciences*, vol. 34, no. 2, pp. 131–143, 2010.

Research Article

Structure and Physical Properties of PZT-PMnN-PSN Ceramics Near the Morphological Phase Boundary

Nguyen Dinh Tung Luan,¹ Le Dai Vuong,^{1,2} Truong Van Chuong,²
and Nguyen Truong Tho²

¹ The Fundamental Science Department, Hue Industry College, Hue City, Vietnam

² Department of Physics, College of Sciences, Hue University, Hue City, Vietnam

Correspondence should be addressed to Nguyen Dinh Tung Luan; ntungluan@yahoo.com

Received 1 August 2013; Accepted 11 December 2013; Published 20 January 2014

Academic Editor: Mohammad Mahroof-Tahir

Copyright © 2014 Nguyen Dinh Tung Luan et al. This is an open access article distributed under the Creative Commons Attribution License, which permits unrestricted use, distribution, and reproduction in any medium, provided the original work is properly cited.

The $0.9\text{Pb}(\text{Zr}_x\text{Ti}_{1-x})\text{O}_3-0.07\text{Pb}(\text{Mn}_{1/3}\text{Nb}_{2/3})\text{O}_3-0.03\text{Pb}(\text{Sb}_{1/2}\text{Nb}_{1/2})\text{O}_3$ (PZT-PMnN-PSN) ceramics were prepared by columbite method. The phase structure of the ceramic samples was analyzed. Results show that the pure perovskite phase is in all ceramics specimens. The effect of the Zr/Ti ratio on the region of morphotropic phase boundary for PZT-PMnN-PSN ceramics was studied. Experimental results show that the phase structure of ceramics changes from tetragonal to rhombohedral with the increase of the content of Zr/Ti ratio in the system. The composition of PZT-PMnN-PSN ceramics near the morphotropic phase boundary obtained is the ratio of Zr/Ti: 49/51. At this ratio, the ceramic has the optimal electromechanical properties: the $k_p = 0.61$, the $\epsilon_{\max} = 29520$, the $d_{31} = -236$ pC/N, the $Q_m = 2400$, high remanent polarization ($P_r = 49.2$ $\mu\text{C}\cdot\text{cm}^{-2}$), and low coercive field $E_c = 10.28$ kV $\cdot\text{cm}^{-1}$.

1. Introduction

Lead zirconate titanate (PZT) is one of the most commonly used ferroelectric ceramic materials. The material has been studied intensively since discovery of the miscibility of lead titanate and lead zirconate in the 1950s [1–5]. Due to their excellent dielectric, pyroelectric, piezoelectric, and electrooptic properties, they have a variety of applications in high energy capacitors, nonvolatile memories (FRAM), ultrasonic sensors, infrared detectors, electrooptic devices, and step-down multilayer piezoelectric transformers for AC-DC converter applications [5, 6]. Until now, many ternary and quaternary systems, such as $\text{Pb}(\text{Ni}_{1/3}\text{Nb}_{2/3})\text{O}_3$ -PZT, $\text{Pb}(\text{Y}_{2/3}\text{W}_{1/3})\text{O}_3$ -PZT, $\text{Pb}(\text{Mn}_{1/3}\text{Sb}_{2/3})\text{O}_3$ -PZT, $\text{Pb}(\text{Mg}_{1/3}\text{Nb}_{2/3})\text{O}_3$ - $\text{Pb}(\text{Ni}_{1/3}\text{Nb}_{2/3})\text{O}_3$ -PZT, $\text{Pb}(\text{Ni}_{1/2}\text{W}_{1/2})\text{O}_3$ - $\text{Pb}(\text{Mn}_{1/3}\text{Nb}_{2/3})\text{O}_3$ -PZT, and PZT-PMnSbN, [4, 5, 7–11] have been synthesized by modifications or substitutions to satisfy

the requirements of practical applications of piezoelectric transformer.

In ceramics manufacturing technology, piezoelectric PZT system ceramics compositions are mostly near the tetragonal-rhombohedral (T-R) morphotropic phase boundary (MPB). The electromechanical response of these ceramics is known to be most pronounced at the MPB. So, there have been many investigations on the coexistence of two phases near MPB in PZT system [3]. The reports suggested the existence of a range of compositions where both tetragonal and rhombohedral phases are thermodynamically stable [7, 12].

In this study, $0.9\text{Pb}(\text{Zr}_x\text{Ti}_{1-x})\text{O}_3-0.07\text{Pb}(\text{Mn}_{1/3}\text{Nb}_{2/3})\text{O}_3-0.03\text{Pb}(\text{Sb}_{1/2}\text{Nb}_{1/2})\text{O}_3$ (PZT-PMnN-PSN) ceramics in the vicinity of MPB were investigated according to the Zr/Ti ratio content. The purpose of this work is to study structure and ferroelectric and piezoelectric properties in the vicinity of the MPB in detail. Furthermore, the width of coexistence of

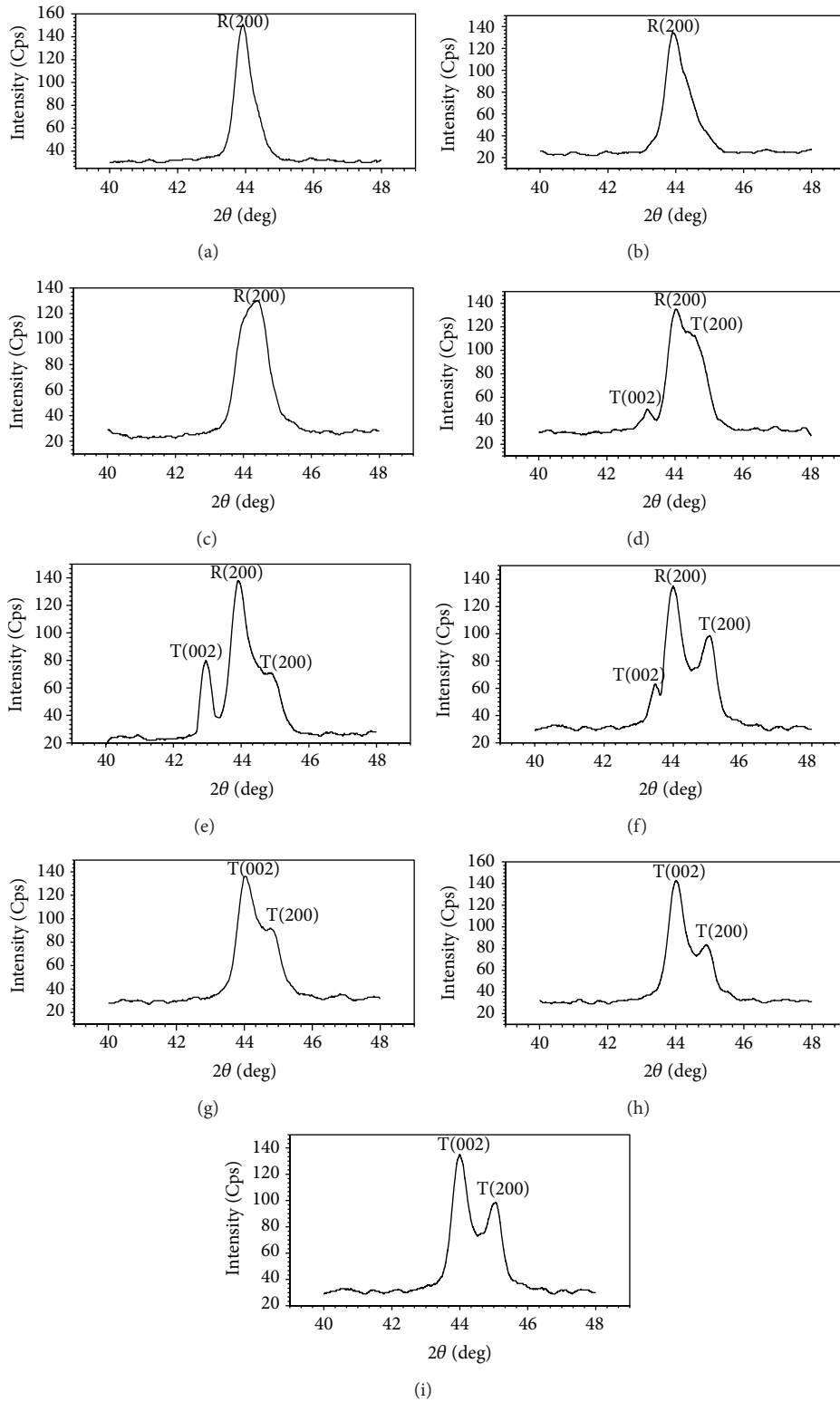


FIGURE 1: XRD patterns for compositions at (a) 54/46; (b) 53/47; (c) 52/48; (d) 51/49; (e) 50/50; (f) 49/51; (g) 48/52; (h) 47/53; (i) 46/54.

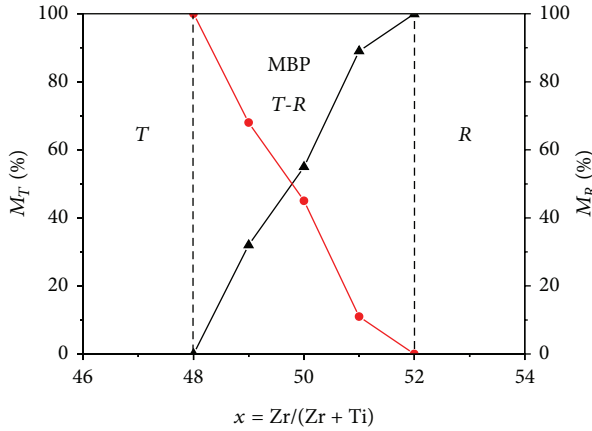


FIGURE 2: Variations of relative content of the tetragonal and rhombohedra phases with Zr/Ti ratio.

tetragonal and rhombohedra phases and the exact composition of the MPB in chemically homogeneous PZT-PMnN-PSN ceramics were determined.

2. Experimentals

The polycrystalline samples of PZT-PMnN-PSN were synthesized by columbite precursor method. The raw materials including powders (high purity) of PbO (99%), ZrO₂ (99.9%), TiO₂ (99%), MnCO₃ (99%), Sb₂O₃ (99%), and Nb₂O₅ (99.9%) for the given composition were weighted by mole ratio. First, the finely mixed powder of MnCO₃ and Nb₂O₅; Sb₂O₃ and Nb₂O₅ are mixed in a Teflon-mortar for about 10 h in an acetone medium and then calcined at 1200°C in an alumina crucible for 3 h. The calcined powder was then grinded and mixed by mortar again with PbO, ZrO₂ and TiO₂ for 30 h. The finely mixed powder was calcined at 850°C for 2 h.

The ground materials were pressed into disk 12 mm in diameter and 1.5 mm in thickness under 100 MPa. The samples were sintered in a sealed alumina crucible with PbZrO₃ coated powder at temperature 1150°C for 2 h. Scanning electron micrograph of the sample was taken at room temperature. The sintered pellet was polished and silver electroded and connected to an LCR meter (Hioki, Japan) for dielectric measurement. The frequency dependence of dielectric constant and loss tangent were obtained using the LCR meter in the frequency range from 0.1 kHz to 500 kHz. The polarization-electric field (*P-E*) hysteresis loops were measured by a Sawyer-Tower circuit at 50 Hz.

As-sintered samples were ground and polished to remove the surface layer for X-ray diffraction (XRD, D/MAX-RB, Rigaku, Japan). Cu K α radiation with a step of 0.01 s was used. The microstructure of the samples was examined by using a scanning electron microscope (SEM). The electromechanical coupling factor (k_p), mechanical quality factor (Q_m), and piezoelectric coefficient (d_{31}) were calculated by using the resonance-antiresonance method. The dielectric constant

was calculated from the capacitance and the dimension of the samples.

3. Results and Discussion

3.1. Structure and Microstructure. It is reported that tetragonal, rhombohedra, and T-R phases were identified by an analysis of the peaks (002 (tetragonal), 200 (tetragonal), and 200 (rhomboheda)) in the 2θ range 43°–47°. The splitting of (002) and (200) peaks indicates that they are the ferroelectric tetragonal phase (FT), while the single (200) peak shows the ferroelectric rhombohedra phase (FR) [1, 6, 13]. Figure 1 shows the XRD patterns of PZT-PMnN-PSN with Zr/Ti ratio at 54/46 up to 46/54. Triplet peaks indicate that the samples consist of a mixture of tetragonal and rhombohedra phases.

A transition from tetragonal phase to rhombohedra phase is observed as Zr/Ti ratio increases. The multiple peak separation method was used to estimate the relative fraction of coexisting phases. The relative phase fraction was then calculated by the following equations [14]:

$$M_R = \frac{I_{R(200)}}{I_{R(200)} + I_{T(002)} + I_{T(200)}}, \quad (1)$$

$$M_T = \frac{I_{T(002)} + I_{T(200)}}{I_{R(200)} + I_{T(002)} + I_{T(200)}}.$$

With increasing Zr/Ti ratio, tetragonal relative fraction decreases and rhombohedra relative fraction increases. The analysis of the relative phase fraction in the PZT-PMnN-PSN system indicates that tetragonal and rhombohedra phases coexist in the composition range for $0.48 \leq x \leq 0.52$ as shown in Figure 2.

Figure 3 shows the SEM image of the fractured surface of PZT-PMnN-PSN ceramics at different Zr/Ti ratios. It is observed from the micrographs that the average grain size of samples are increased with the increasing amount of Zr/Ti ratio. However, when further increasing the Zr/Ti ratio to 51/49, the average grain size is reduced. These results are in good agreement with the reported in the literature [15].

3.2. Dielectric and Ferroelectric Properties

3.2.1. The Influence of Zr/Ti Ratio on the Dielectric Properties.

Figure 4 shows the temperature dependence of dielectric permittivity and dielectric loss $\tan \delta$ of PZT-PMnN-PSN system (1 kHz) with Zr/Ti ratios 46/54 up to 54/46, respectively. As shown in Figure 4, all the samples in morphotropic phase boundary region (Zr/Ti = 48/52–52/48) exhibit typical relaxor ferroelectric behavior around. The dielectric responses are characterized by diffuse dielectric peaks and a slight shift of permittivity of maximum toward higher temperature with increasing frequencies.

By comparing the curves in Figure 1, we see that the broadness of dielectric response increases with an increase in Zr/Ti ratio and the largest is at Zr/Ti = 49/51. The temperature of dielectric permittivity maximum also increases with increase of Zr/Ti ratio. All samples have a temperature called

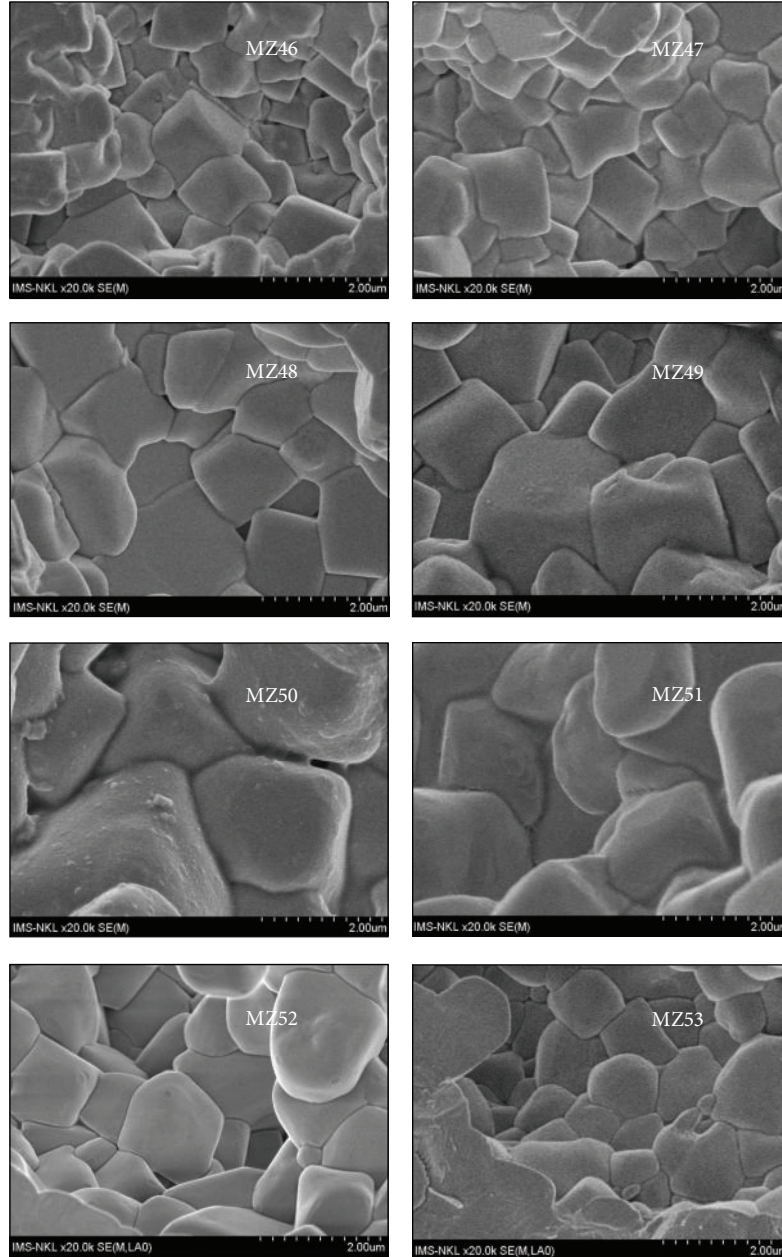


FIGURE 3: Surface morphologies observed by SEM of PZT-PMnN-PSN ceramics at various ratios of Zr/Ti.

Burn temperature at which dielectric response starts complying Curie-Weiss law and the system starts the transition into paraelectric phase.

Figure 5 shows Curie-Weiss dependence of the permittivity of the samples at temperatures start to T_B . The fitting parameters [14] are given in Table 1.

From Table 1, we can see that all the temperature values extend to decrease with the increase of Zr/Ti ratio.

3.2.2. The Influence of Zr/Ti Ratio on the Ferroelectric Properties. Figure 6 shows P - E hysteresis loops of all samples. The well-saturated hysteresis loops were observed, and the values

of remanent polarization (P_r) and coercive field (E_c) were presented in Table 2.

It's demonstrated that the hysteresis loops of all samples are of typical forms characterizing ferroelectric materials. The remanent polarization (P_r) reaches the maximum value of $49.2 \mu\text{C}/\text{cm}^2$ and The coercive field (E_c) reaches the minimum value of $10.28 \text{ kV}\cdot\text{cm}^{-1}$ at $\text{Zr}/\text{Ti} = 49/51$ (Figure 7).

4. Piezoelectric Properties

Figure 8 shows the piezoelectric and dielectric properties as a function of Zr/Ti ratio. PZT-PMnN-PSN exhibits high

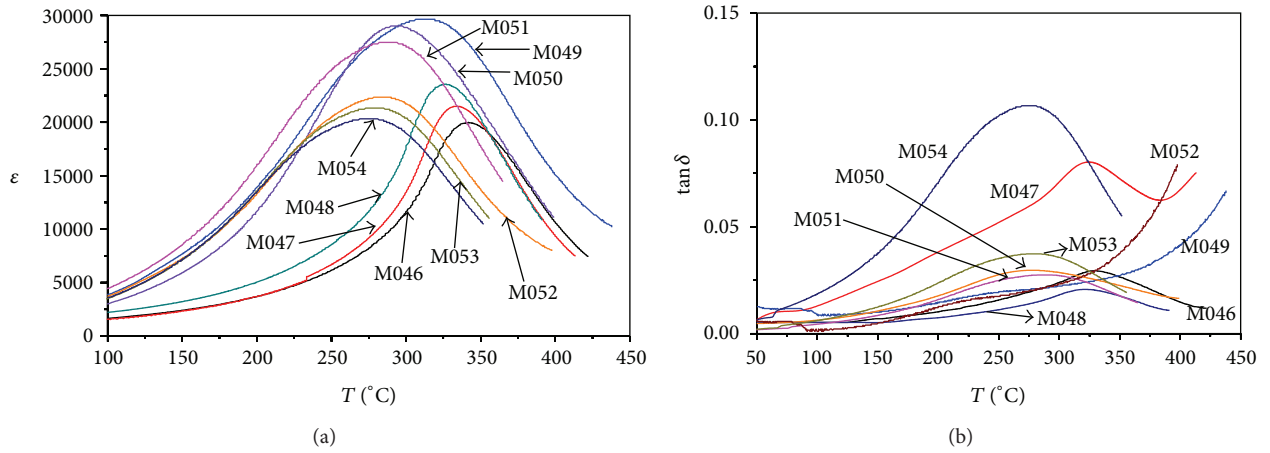


FIGURE 4: (a) Dielectric constant and (b) loss tangent of PZT-PMnN-PSN at various Zr/Ti ratios.

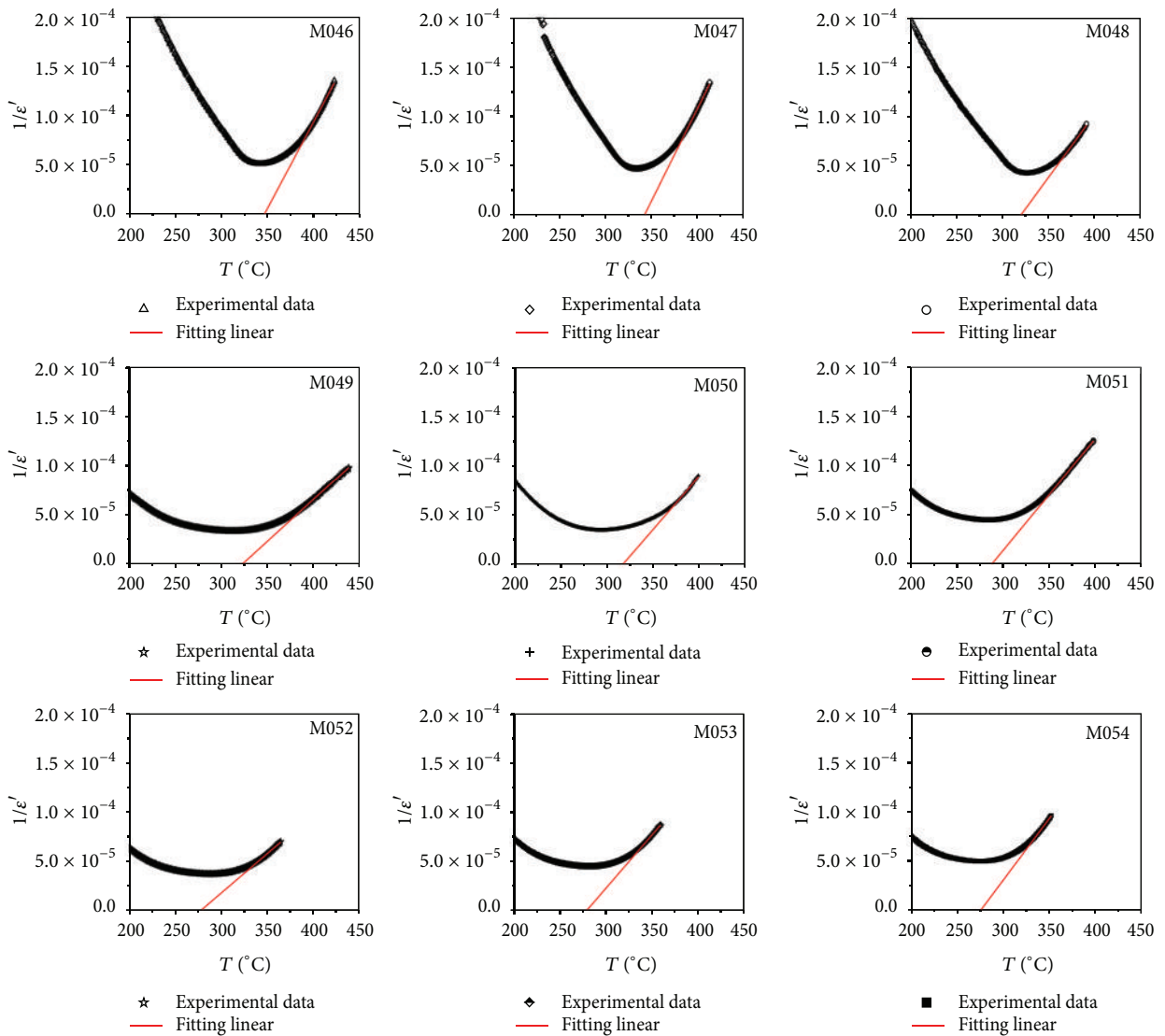


FIGURE 5: Curie-Weiss dependence of the permittivity of the samples at temperatures start to T_B .

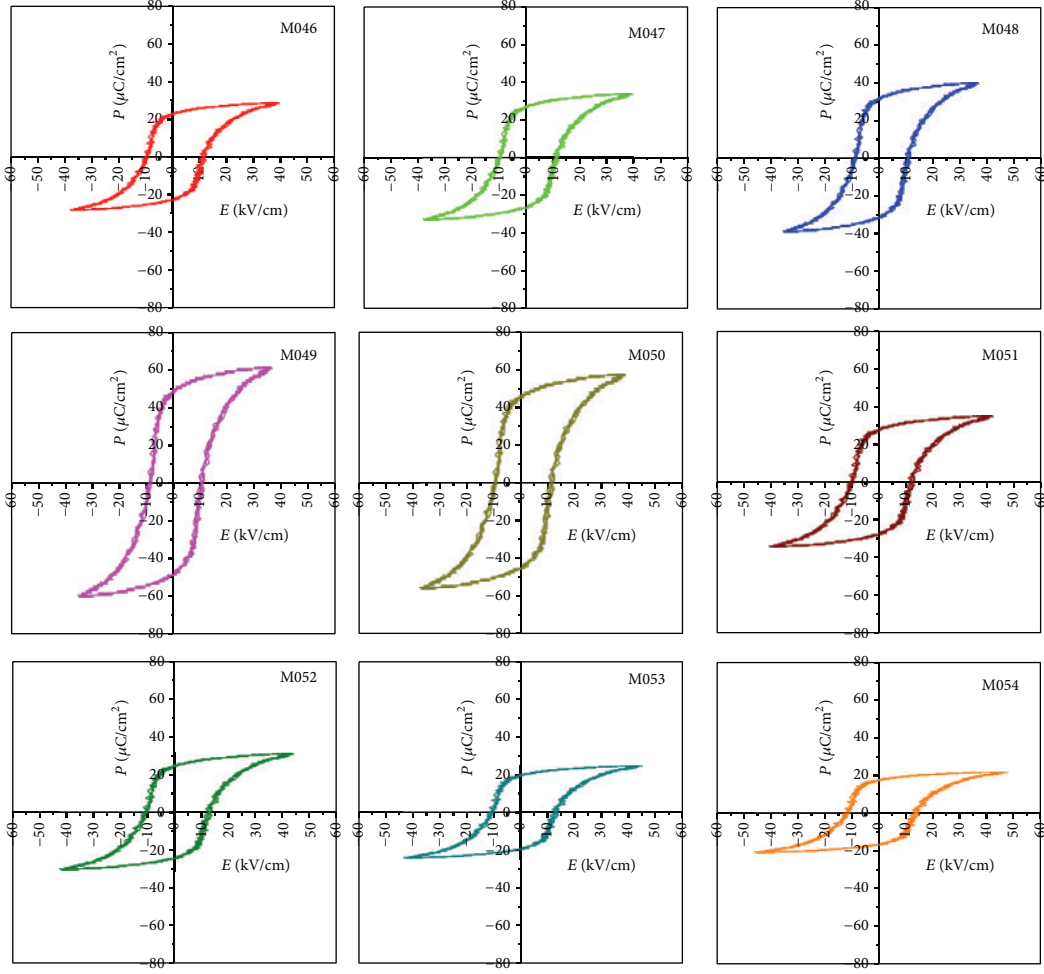
FIGURE 6: P - E hysteresis loops of PZT-PMnN-PSN samples.

TABLE 1: Dielectric properties and fitting parameters of PZT-PMnN-PSN ceramics.

Sample	ϵ	$\tan \delta$	ϵ'_{\max}	T_m ($^{\circ}\text{C}$)	T_B ($^{\circ}\text{C}$)	T_C ($^{\circ}\text{C}$)
M046	674	0.023	21343	343	390.3	347.4
M047	699	0.035	21447	337	380.2	342.3
M048	735	0.041	23050	325	375.8	330.8
M049	899	0.044	29520	312	370.4	315.5
M050	887	0.046	29018	298	366.9	304.6
M051	756	0.022	27609	289	348.3	300.1
M052	739	0.023	22348	280	342.5	292.4
M053	692	0.014	21349	271	332.7	281.9
M054	554	0.013	19875	266	325.3	274.4

TABLE 2: Calculated P_r and E_c values of samples.

Sample	E_c (kV/cm)	P_r ($\mu\text{C}/\text{cm}^2$)
M046	11.32	23.0
M047	11.07	27.0
M048	10.37	32.0
M049	10.28	49.2
M050	10.88	46.0
M051	11.85	28.0
M052	12.40	25.0
M053	12.66	19.7
M054	13.45	17.3

piezoelectric coefficient and electromechanical coupling factor around the MPB. From the trend of the variation of piezoelectricity, it reaches the maximum values of $d_{31} = -236 \text{ pC/N}$, $k_p = 0.61$ at $\text{Zr/Ti} = 49/51$.

Simple diagram phase of PZT-PMnN-PSN ceramics near MPB, which is attractive system displaying excellent piezoelectric and dielectric properties, good electrostrictive effects, and relaxation of ferroelectric phase transition is shown in Figure 9.

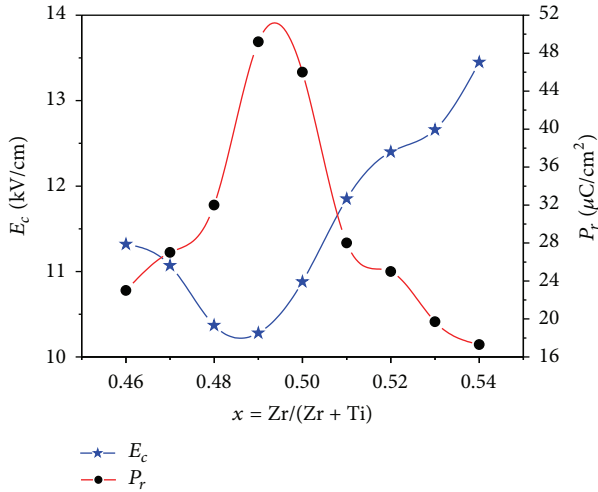


FIGURE 7: The P_r and the E_c as a function of Zr/Ti ratios.

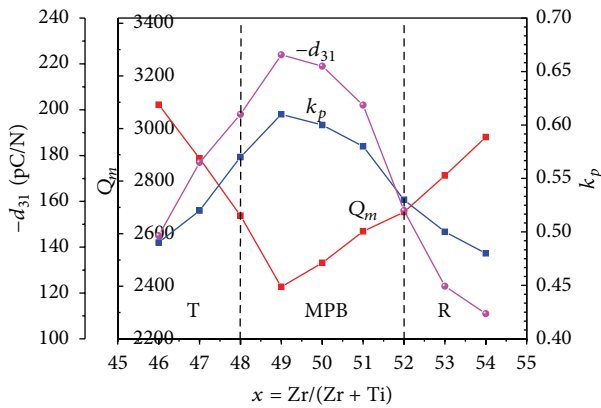


FIGURE 8: Piezoelectric properties of PZT-PMnN-PSN at various Zr/Ti ratios.

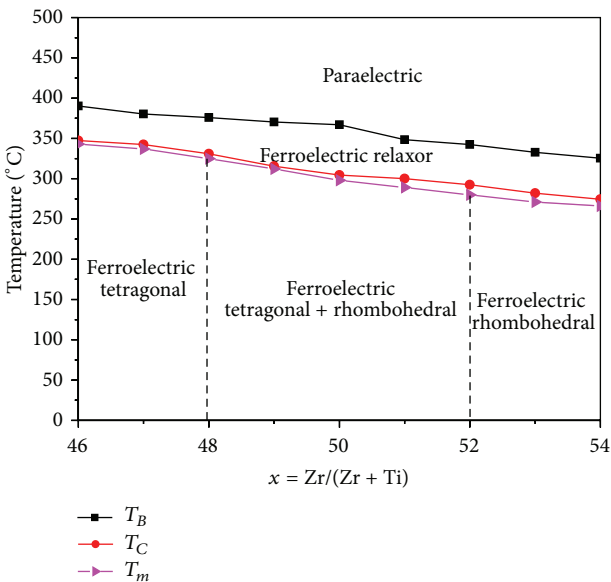


FIGURE 9: Simple diagram phase of PZT-PMnN-PSN system near MPB.

5. Conclusion

The results obtained from the experiment are as follows.

- (1) PZT-PMnN-PSN ceramics with 7% wt excess PbO were prepared by columbite method.
- (2) The structure of ceramics sintered at 1150°C shows the pure perovskite structure in all ceramics specimens; the structure of PZT-PMnN-PSN ceramics was transformed from tetragonal to rhombohedra, with Zr/Ti ratio increased in system.
- (3) The composition of PZT-PMnN-PSN ceramics near the morphotropic phase boundary obtained is the ratio of Zr/Ti = 49/51. At this ratio, the ceramic has the optimal electromechanical properties: the $k_p = 0.61$, the $\epsilon_{\max} = 29520$, the $d_{31} = -236$ pC/N, the $Q_m = 2400$, high remanent polarization ($P_r = 49.2 \mu\text{C}\cdot\text{cm}^{-2}$), and low coercive field $E_c = 10.28 \text{ kV}\cdot\text{cm}^{-1}$.
- (4) The piezoelectric ceramic with Zr/Ti ratio of 49/51 may be suitable for piezoelectric transformer applications and other high power devices.

Conflict of Interests

The authors declare that there is no conflict of interests regarding the publication of this paper.

Acknowledgment

This work is supported by the National Foundation for Science and Technology Development (NAFOSTED), no. 103.02.06.09.

References

- [1] F. Gao, L. Cheng, R. Hong, J. Liu, C. Wang, and C. Tian, "Crystal structure and piezoelectric properties of $x\text{Pb}(\text{Mn}_{1/3}\text{Nb}_{2/3})\text{O}_3 - (0.2-x)\text{Pb}(\text{Zn}_{1/3}\text{Nb}_{2/3})\text{O}_3 - 0.8\text{Pb}(\text{Zr}_{0.52}\text{Ti}_{0.48})\text{O}_3$ ceramics," *Ceramics International*, vol. 35, no. 5, pp. 1719–1723, 2009.
- [2] Z. Necira, A. Boutarfaia, M. Abba, H. Menasra, and N. Abdesslem, "Effects of thermal conditions in the phase formation of undoped and doped $\text{Pb}(\text{Zr}_{1-x}\text{Ti}_x)\text{O}_3$ solid solutions," *Materials Sciences and Applications*, vol. 4, no. 5, pp. 319–323, 2013.
- [3] Y. Xu, *Ferroelectric Materials and Their Applications*, North-Holland, London, UK, 1991.
- [4] J. Yoo, Y. Lee, K. Yoon et al., "Microstructural, electrical properties and temperature stability of resonant frequency in $\text{Pb}(\text{Ni}_{1/2}\text{W}_{1/2})\text{O}_3 - \text{Pb}(\text{Mn}_{1/3}\text{Nb}_{2/3})\text{O}_3 - \text{Pb}(\text{Zr,Ti})\text{O}_3$ ceramics for high-power piezoelectric transformer," *Japanese Journal of Applied Physics A*, vol. 40, no. 5, pp. 3256–3259, 2001.
- [5] R. Muanghlua, S. Niemchareon, W. C. Vittayakorn, and N. Vittayakorn, "Effects of Zr/Ti ratio on the structure and ferroelectric properties in PZT-PZN-PMN ceramics near the morphotropic phase boundary," *Advanced Materials Research*, vol. 55–57, pp. 125–128, 2008.
- [6] F. Kahoul, L. Hamzioui, N. Abdesslem, and A. Boutarfaia, "Synthesis and piezoelectric properties of $\text{Pb}_{0.98}\text{Sm}_{0.02}$

- $[(\text{Zr}_y, \text{Ti}_{1-y})_{0.98}(\text{Fe}^{3+}, \text{Nb}^{5+})_{0.02}]\text{O}_3$ ceramics,” *Materials Sciences and Applications*, vol. 3, pp. 50–58, 2012.
- [7] N. D. T. Luan, L. D. Vuong, and B. C. Chanh, “Microstructure, ferroelectric and piezoelectric properties of PZT–PMnSbN ceramics,” *International Journal of Materials and Chemistry*, vol. 3, pp. 51–58, 2013.
- [8] M. Kobune, Y. Tomoyoshi, A. Mineshige, and S. Fujii, “Effects of MnO_2 addition on piezoelectric and ferroelectric properties of $\text{PbNi}_{1/3}\text{Nb}_{2/3}\text{O}_3$ – PbTiO_3 – PbZrO_3 ceramics,” *Journal of the Ceramic Society of Japan*, vol. 108, no. 7, pp. 633–637, 2000.
- [9] S. J. Yoon, A. Joshi, and K. Uchino, “Effect of additives on the electromechanical properties of $\text{Pb}(\text{Zr}, \text{Ti})\text{O}_3$ – $\text{Pb}(\text{Y}_{2/3}\text{W}_{1/3})\text{O}_3$ ceramics,” *Journal of the American Ceramic Society*, vol. 80, no. 4, pp. 1035–1039, 1997.
- [10] Y. K. Gao, Y. H. Chen, J. H. Ryu, K. J. Uchino, and D. Viehland, “Eu and Yb substituent effects on the properties of $\text{Pb}(\text{ZrM}_{0.52}\text{Ti}_{0.48})\text{O}_3$ – $\text{Pb}(\text{Mn}_{1/3}\text{Sb}_{2/3})\text{O}_3$ ceramics: development of a new high-power piezoelectric with enhanced vibrational velocity,” *Japanese Journal of Applied Physics*, vol. 40, no. 2, pp. 687–693, 2001.
- [11] Z. L. Gui, L. T. Li, H. Q. Lin, and X. W. Zhang, “Low temperature sintering of lead magnesium nickel niobate zirconate titanate (PMN–PNN–PZT) piezoelectric ceramic, with high performances,” *Ferroelectrics*, vol. 101, no. 1, pp. 93–99, 1990.
- [12] Z. Yang, H. Li, X. Zong, and Y. Chang, “Structure and electrical properties of PZT–PMS–PZN piezoelectric ceramics,” *Journal of the European Ceramic Society*, vol. 26, no. 15, pp. 3197–3202, 2006.
- [13] H. Fan and H. Kim, “Perovskite stabilization and electromechanical properties of polycrystalline lead zinc niobate-lead zirconate titanate,” *Journal of Applied Physics*, vol. 91, no. 1, pp. 317–322, 2002.
- [14] A. Quintana-Nedelcos, A. Fundora, H. Amorín, and J. M. Siqueiros, “Effects of Mg addition on phase transition and dielectric properties of $\text{Ba}(\text{Zr}_{0.05}\text{Ti}_{0.95})\text{O}_3$ system,” *The Open Condensed Matter Physics Journal*, vol. 2, pp. 1–8, 2009.
- [15] L. D. Vuong, P. D. Gio, T. Van Chuong, D. T. H. Trang, D. V. Hung, and N. T. Duong, “Effect of Zr/Ti ratio content on some physical properties of the low temperature sintering PZT–PZN–PMnN ceramics,” *International Journal of Materials and Chemistry*, vol. 3, no. 2, pp. 39–43, 2013.

Research Article

Nonlinear-Electronic Transport in Fe₂O₃ Thin-Films Grown from Grain-Oriented Iron Foils

Roberto Baca Arroyo

Department of Electronics, National Polytechnic Institute, Distrito Federal, Mexico City 07738, MEX, Mexico

Correspondence should be addressed to Roberto Baca Arroyo; rbaca02006@yahoo.com.mx

Received 16 August 2013; Accepted 24 October 2013

Academic Editor: Feng Zhao

Copyright © 2013 Roberto Baca Arroyo. This is an open access article distributed under the Creative Commons Attribution License, which permits unrestricted use, distribution, and reproduction in any medium, provided the original work is properly cited.

Nonlinear-electronic transport in Fe₂O₃ thin-films grown by thermal oxidation from grain-oriented iron foils was studied by current-voltage characteristics at room temperature as a function of the oxidation temperature. Microstructure formation and its changes were investigated by atomic force microscopy and X-ray diffraction studies. X-ray diffraction has demonstrated that average grain size was weakly increased with the growth temperature. The analysis of current-voltage characteristics shows ohmic regime at low voltages and space-charge-limited regime at higher voltages. Space-charge effects resulted from the discontinuous grain growth of the foils. Further, nonlinear-electronic transport of Fe₂O₃ thin-films can be useful for the designing of adaptive oxide electronic devices.

1. Introduction

Space-charge-limited current was studied in vacuum tube technology at around 1906. Scientists had developed technologies based on vacuum tubes including high-power, signal amplifier, and military applications, due to its resistance to electromagnetic pulse. Therefore, the space charge phenomena can renew the era of solid-state-electronics in the operation principle of adaptive oxide electronic devices based on space-charge effects, which could be useful for smart devices with nonlinear characteristics [1–3].

Recently was demonstrated how changing from bulk to nanoscale materials can significantly change the material properties in transition metal oxides (TMOs) [4] and consequently their performance. Therefore, space-charge effects at the interface between small particles can result in substantial improvement of the electrical, magnetic, and optical properties [5–7].

Adaptive oxide electronic devices based on vertical structure with small area can be implemented in driver circuits for power applications [8, 9], because the current flow can be modulated by an electrode embedded in the middle of the device even for low carrier mobility of the metal oxide thin-films [7, 10]. Also, in response to the needs of ecological

concerns, low-cost, abundance, stability, nontoxicity, and environmentally, TMOs should be studied and adapted for new applications. For example, iron oxide has attracted interest of researchers [11–13]. It is well known that hematite (Fe₂O₃) has a low conductivity as well as low electron mobility at room temperature in comparison with silicon [14]. Also, it is known that activation energy for Fe₂O₃ varies nonmonotonically with temperature [15, 16].

Nonlinear-electronic transport in Fe₂O₃ thin-films produced by thermal oxidation has been investigated in this work. Microstructure formation was studied by atomic force microscopy and X-ray diffraction as a function of the growth temperature as well as the study of the nonlinear-current conduction as a function of thickness was conducted by current-voltage characteristics at room temperature.

2. Experimental Procedure

Fe₂O₃ thin-films were grown by thermal oxidation from grain-oriented iron foils. The grain-oriented iron foil is a soft magnetic material that is used as the core material in electrical transformers. In this work, grain-oriented foils were obtained from cores of low-power transformers with thickness of

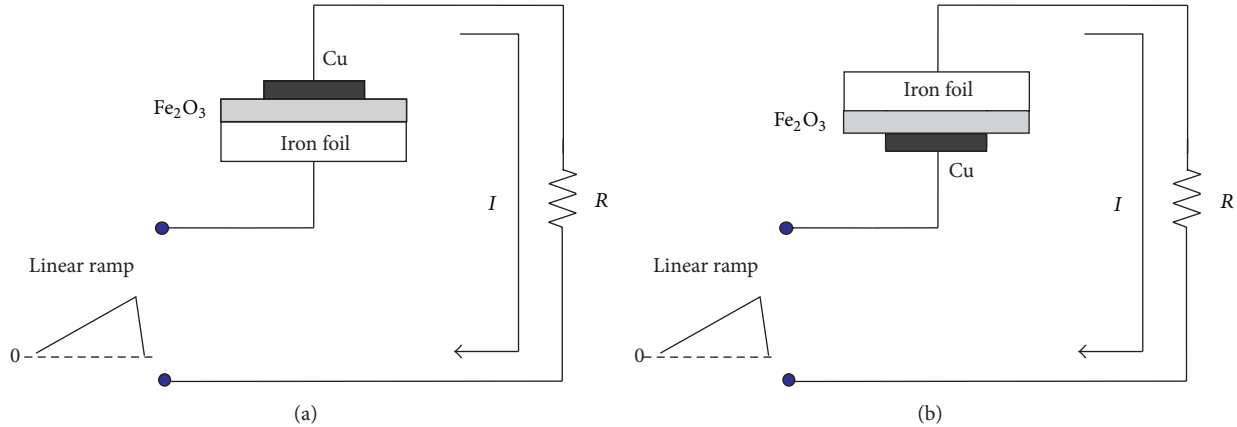


FIGURE 1: Schematic diagram of samples and series circuit under forward bias (a) and reverse bias (b).

0.18 mm. It is known that grain-oriented foils are usually coated to reduce the eddy currents and to provide resistance to corrosion. Therefore, before oxidation processes, the iron foils with cross-sectional area of 1 cm^2 were mechanically polished and cleaned using organic solvents and deionized water. After polishing, the samples were thermally oxidized under air atmosphere conditions in the temperature range from 400°C to 550°C with duration of 20 min into resistively heated quartz tube furnace. A copper electrode of square geometry of $0.1 \text{ cm} \times 0.1 \text{ cm}$ was placed on each sample as mechanical point contact as shown in the schematic diagram of Figure 1.

Microstructure formation was analyzed by both atomic force micrographs and X-ray diffraction patterns. Atomic force micrographs of the Fe₂O₃ thin-films were obtained with a Digital Instrument (Veeco) Nanoscope and X-ray diffraction patterns with a PANalytical X-ray diffractometer with $\text{CuK}\alpha$ radiation ($\lambda = 0.15418 \text{ nm}$) in the scan range $20\text{--}90^\circ$. Current-voltage characteristics of the samples were measured by using digital storage oscilloscope (Tektronix, TDS1012C). Both voltage and current signals were recorded employing a series circuit shown in Figure 1(a) under forward bias and Figure 1(b) under reverse bias. Both voltage and current signals were plotted as lissajous figures on the screen of oscilloscope. A lissajous figure gives the instantaneous values of voltage as a function of the current.

3. Results and Discussion

It is known that the oxidation process of iron oxide should be dependent on the solubility of oxygen into iron foil and energy to take an oxygen ion and form the oxide. Therefore, vacant cation sites (oxygen ions) will diffuse away from the oxide-air interface and vacant anion sites (iron ions) through the oxide during the oxidation process [17]. In the procedure presented here at intermediate temperature ($<700^\circ\text{C}$), a first monolayer of iron oxide is grown and corresponds to Fe₂O₃ phase with lattice parameter similar to grain-oriented iron foil. This phase is characterized by a Goss texture with a (110) preferred crystal orientation [18].

Then, the oxide continues to grow with this texture with strong cohesive forces [17, 19]. Structural defects can be formed into the grown oxide by discontinuous Goss grain growth, which is depending on the industrial production process of the grain-oriented iron foils.

3.1. Microstructure Formation. Microstructure formation studies are conducted to know the stability of the Fe₂O₃ thin-films grown by thermal oxidation at lower temperature than 700°C and under air atmosphere conditions. Atomic force microscopy studies were done to demonstrate the homogeneity and reproducibility of the samples controlled by diffusion process and X-ray diffraction analysis to show the polycrystalline Fe₂O₃ phase formation in the samples.

Figure 2 shows the atomic force micrographs of Fe₂O₃ thin-films at various temperatures. A noncontact mode of operation was employed between the tip and sample with scanned area of $1 \mu\text{m} \times 1 \mu\text{m}$ to provide a method to analyze the oxide formation on samples surface as a function of the roughness based on bearing algorithm from Veeco Nanoscope software.

The average roughness, R_{avg} , can be estimated with the intersection of both depth profile and bearing area plots as indicated in Figure 3 with dashed lines and is related to average grain height distribution, and their values are presented in Table 1.

It is demonstrated that a discontinuous growth mechanism favors the oxide formation and grain size in the samples as shown in Figure 3. However, at temperatures ($>500^\circ\text{C}$), a decrease of the oxide formation can be observed in Figure 3(d), because the discontinuous oxide achieves its critical thickness [17, 18, 20].

Figure 4 shows X-ray diffraction patterns of the thermally oxidized samples. Samples were processed at 400°C and 450°C with peaks located at 65.08° and 81.07° with (530) and (710) planes. Samples were processed at 500°C with peaks located at 30.06° , 35.46° , 43.02° , 65.04° , and 81.07° corresponding to (220), (311), (400), (530), and (710) planes as well as peaks positioned at 33.13° , 35.53° , 42.98° , 65.04° , and 81.07° with (310), (311), (400), (530), and (710) planes

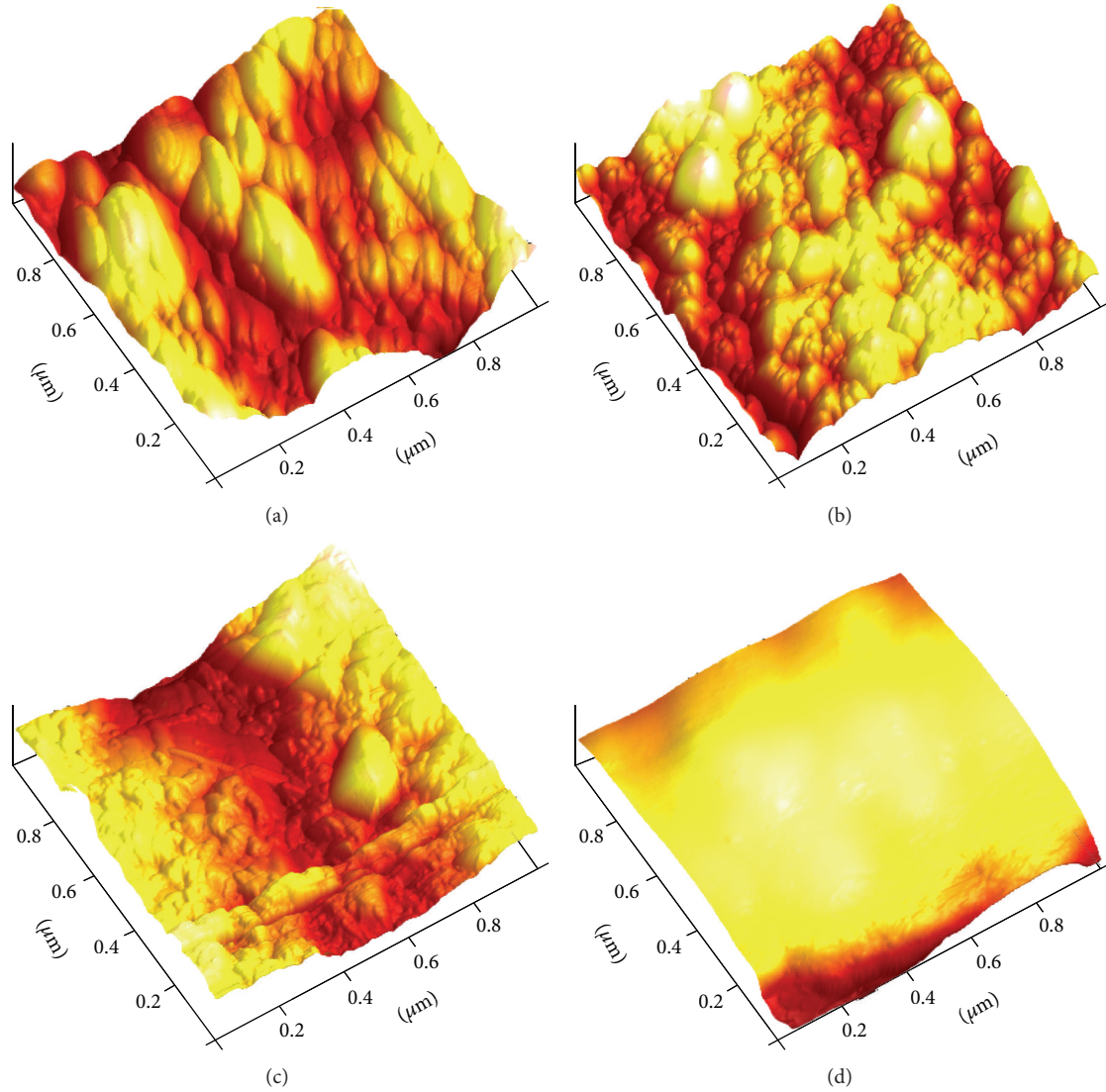


FIGURE 2: Atomic force micrographs of the oxidized samples under air atmosphere conditions.

were observed in samples processed at 550°C . All peaks correspond to the cubic Fe_2O_3 phase according to PANalytical Card no. 00-019-0629. The cubic Fe structure can be seen in all samples processed with peaks at 44.67° and 82.33° with (110) and (211) planes according to PANalytical Card no. 00-002-0426 and associated with Goss texture [18].

The thickness d of samples was measured by a Tencor profilometer. Both thickness d and average grain size D were indicated in Table 1. Average grain size was estimated with Debye-Scherrer formula based on X-ray diffraction patterns [21, 22].

According to atomic force microscopy studies of Figure 3 and X-ray diffraction analysis of Figure 4, the main scattering mechanism for carriers in Fe_2O_3 thin-films can be grain boundary scattering, which is associated with transitional regions between different orientations of neighboring crystallites. Also, potential barrier between crystallites with

lattice defects-induced trapping states can impede the carrier motion into the Fe_2O_3 thin-films. As a consequence, when the mean free path of carriers is comparable with smaller crystalline sizes, D , and critical thickness, d , the charge carrier mobility, μ , could be limited according to microstructure data of Table 1 for Fe_2O_3 thin-films.

3.2. Electronic Transport. The performance of samples was demonstrated with the schematic diagram of Figures 1(a) and 1(b). To ensure the linear response, a function generator (Matrix, MFG-8250A) was used to produce a linear ramp signal at low frequency ($f = 100\text{ Hz}$) with voltage range from 0 V to 5 V to conserve low-voltage operation and avoid magnetic transport (exchange polarization) in the samples [23, 24]. Also, a resistor of $R = 100\ \Omega$ was selected to monitor the current signal in the samples as shown in Figures 1(a) and 1(b). Current-voltage characteristics for both forward

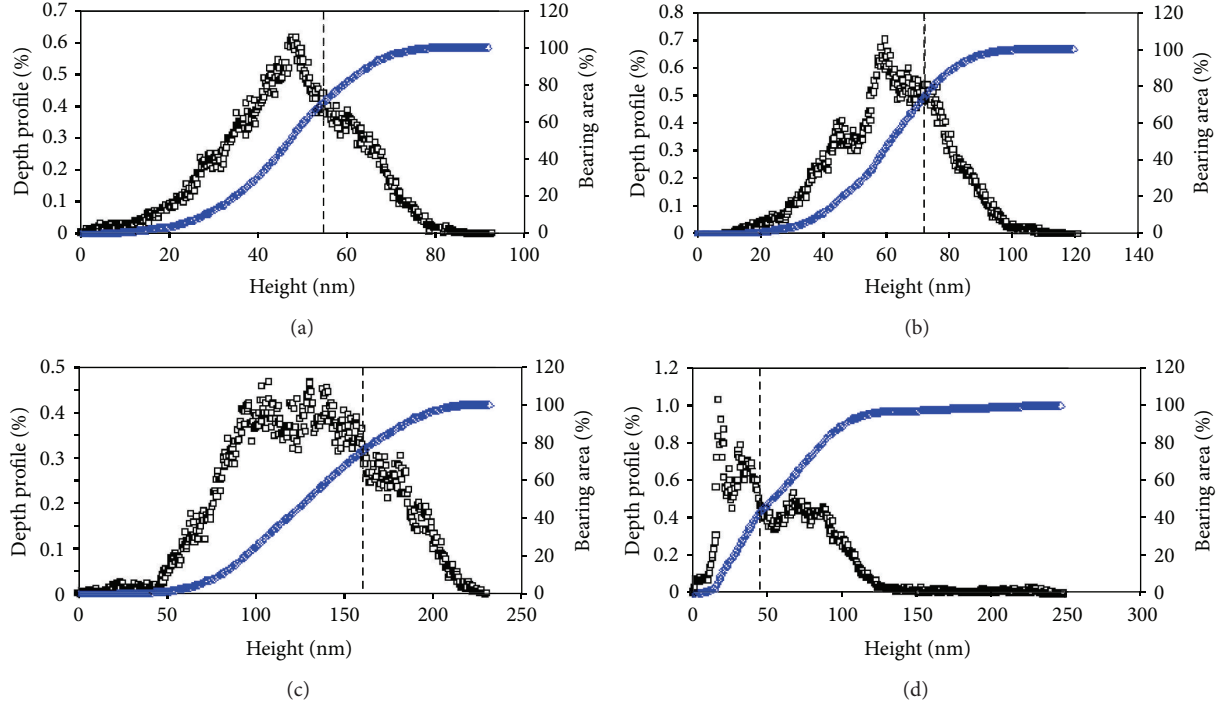


FIGURE 3: Depth profile and bearing area plots of the analyzed micrographs of Figure 2.

TABLE I: Microstructure data for Fe_2O_3 thin-films.

Sample	T ($^\circ\text{C}$)	d (nm)	R_{avg} (nm)	D (nm)
a	400	150	27.5	22.8
b	450	165	36.1	29.3
c	500	220	81.2	21.9
d	550	255	21.8	34.2

and reverse bias are shown in Figures 5 and 6. Nonlinear-electronic transport was observed on the current-voltage characteristics with two regions indicated by slopes.

To investigate the transport parameters of the samples, a model of space-charge-limited transport was proposed and given by

$$I = \frac{9}{32\pi} \epsilon \mu A_e \frac{N_c}{N_t} \exp\left(-\frac{\phi_t}{k_B T}\right) \frac{V^n}{d^3}, \quad (1)$$

where ϵ is the iron oxide dielectric constant (taken as $\epsilon = 540$ for Fe_2O_3 at low frequencies) [15], k_B is the Boltzmann constant, T is the sample temperature, μ is the charge carrier mobility, A_e is the effective cross-sectional area ($A_e = 1 \text{ cm}^2$), N_c is the density of the states available ($N_c = 1.35 \times 10^{19} \text{ cm}^{-3}$) [14], N_t is the density of traps, ϕ_t is the energy level of the traps, V is the applied voltage, and d is the thickness of the Fe_2O_3 thin-films.

The trap concentration, N_t , was estimated from the current-voltage characteristics, with the voltage which is related to slope change and that intersects to the potential drop, V_{TFL} , across the films as indicated in both Figures 5 and 6 [25]. As shown in Figures 5 and 6, ohmic regime $I \propto V$

was observed at low voltages ($0 < V < V_{\text{TFL}}$), while at higher voltages ($V_{\text{TFL}} < V < 5V$), with $I \propto V^n$ regime for $n = 1.5$ to 2. The parameter V_{TFL} corresponds to voltage associated with trap-filled limit with charge carriers and can be linked with the following relation:

$$N_t = \frac{\epsilon}{6e} \frac{V_{\text{TFL}}}{d^2}. \quad (2)$$

Nonlinear behavior on current-voltage characteristics was observed in Figures 5 and 6, which can be associated with collision-free transport at low voltages and collision-dominated transport at higher voltages [26]. It is known that collision-free transport associated with low-field transport is influenced by weak thermal vibrations and charge carrier mobility, μ , independent of the field because carries and lattice are in equilibrium. However, under transport at higher voltages, the collision-dominated transport becomes a nonlinear function of carries with the field and charge carrier mobility, μ , into Fe_2O_3 thin-films [27].

Due to the fact that the charge carrier mobility in the space-charge-limited regime, μ_{SCL} , is connected to nonlinear-electronic transport of the samples, the value of μ_{SCL} should be evaluated for the designing of adaptive electronic devices. μ_{SCL} can be estimated from $\Delta I = ne\mu A_e \Delta V d^{-1}$ as

$$\mu_{\text{SCL}} = \frac{d}{N_t e A_e} m, \quad (3)$$

where m is first slope (ohmic region) on the current-voltage characteristics of Figures 5 and 6 and was extracted using $m = \Delta I / \Delta V$, with ΔI as the differential change of current and ΔV as the differential change of voltage, respectively.

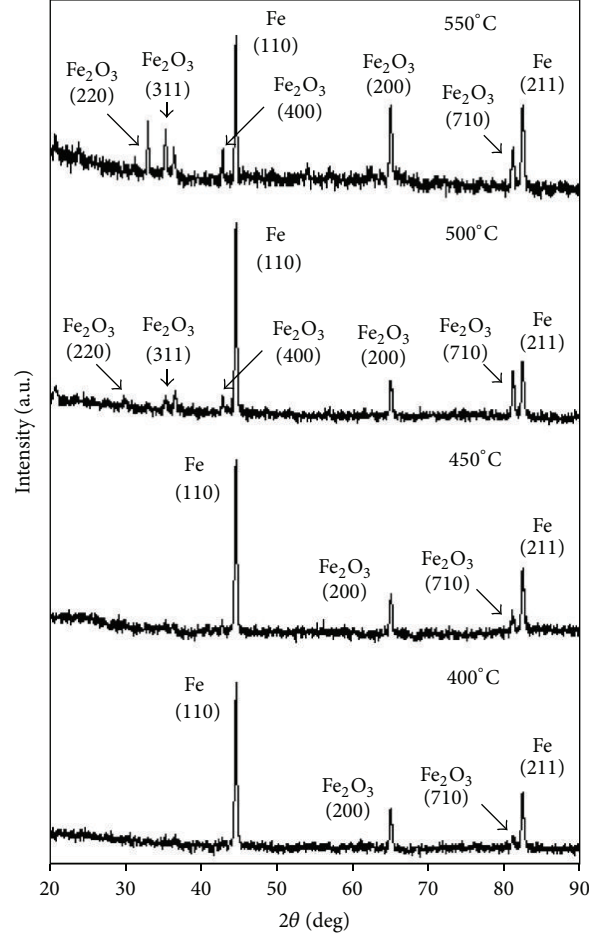


FIGURE 4: XRD patterns of the oxidized samples under air atmosphere conditions.

TABLE 2: Transport parameters under forward bias.

Sample	V_{TFL} (V)	N_t (cm ⁻³)	m	μ_{SCL} (cm ² V ⁻¹ s ⁻¹)	α	ϕ_t (eV)
a	1.2	2.4×10^{15}	6.5×10^{-3}	0.26×10^{-3}	1.5×10^{-3}	0.36
b	0.8	1.3×10^{15}	7.5×10^{-3}	0.59×10^{-3}	3.3×10^{-3}	0.37
c	1.1	9.9×10^{14}	5.7×10^{-3}	0.78×10^{-3}	2.7×10^{-3}	0.37
d	1.6	1.1×10^{15}	3.4×10^{-3}	0.48×10^{-3}	1.1×10^{-3}	0.36

It is assumed in (3) that m can be extracted from ohmic region because low-field transport is used in characterizing semiconductor films to determine the concentration of thermally excited carriers, n , and its charge carrier mobility, μ , [26]. Thus, under space-charge-limited regime, $N_t \gg n$ and (3) with $n = N_t$ was solved.

The space-charge-limited regime obeys to $I = \alpha V^n d^{-3}$, where α is a scaling factor which depends on ϵ , μ , and N_c/N_t ratio. According to (1), α is expressed by

$$\alpha = \frac{9}{32\pi} \epsilon \mu A_e \frac{N_c}{N_t} \exp\left(-\frac{\phi_t}{k_B T}\right). \quad (4)$$

Therefore, transport parameters of the Fe₂O₃ thin-films were extracted solving (2), (3), and (4) and using MATLAB

program. Parameter α was estimated based on nonlinear behavior of Figures 5 and 6 and energy level of traps, ϕ_t , was calculated from (4). Finally, transport parameters were listed for both forward and reverse bias in Tables 2 and 3, respectively.

From Tables 2 and 3, it was demonstrated that activation energy, ϕ_t , for Fe₂O₃ layers varies nonmonotonically with temperature. The V_{TFL} parameter was different for the samples, because slope changes were observed into the current-voltage characteristics, which is related to traps concentration changes, N_t , during the formation of discontinuous Fe₂O₃ thin-films. Contact effects of both Fe/Fe₂O₃ and Fe₂O₃/Cu interfaces may also influence device performance, because grain boundary scattering related with lattice defects-induced

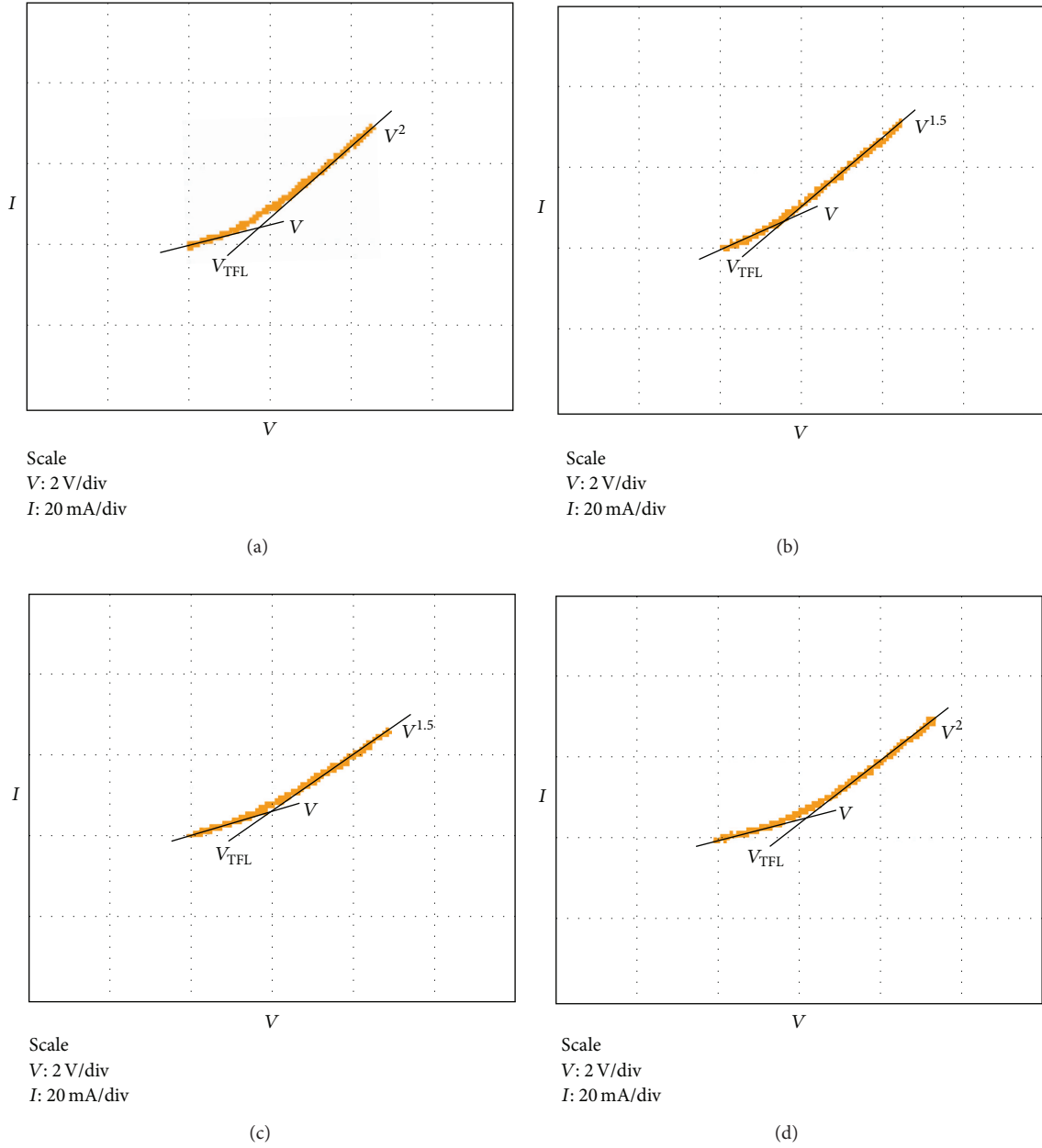


FIGURE 5: Current-voltage characteristics under forward bias.

TABLE 3: Transport parameters under reverse bias.

Sample	V_{TFL} (V)	N_f (cm^{-3})	m	μ_{SCL} ($\text{cm}^2 \text{V}^{-1} \text{s}^{-1}$)	α	ϕ_t (eV)
a	0.8	1.5×10^{15}	2.5×10^{-3}	0.15×10^{-3}	3.0×10^{-3}	0.34
b	1.6	2.7×10^{15}	3.0×10^{-3}	0.11×10^{-3}	1.0×10^{-3}	0.34
c	1.8	1.6×10^{15}	3.1×10^{-3}	0.26×10^{-3}	9.6×10^{-3}	0.35
d	1.1	7.7×10^{14}	3.7×10^{-3}	0.77×10^{-3}	2.8×10^{-3}	0.36

trapping states near to the interface impedes the charge carrier motion by space-charge phenomena.

Nonlinear-electronic transport in samples with lower critical thickness of 250 nm varies monotonically with the low charge carrier mobility, μ_{SCL} , in the space-charge-limited

regime [8, 25]. The low charge carrier mobility in Tables 2 and 3 was affected by bias because the Fe_2O_3 phase provides strong cohesive forces with iron foil and allows a carriers transport with increase of μ_{SCL} under forward bias. However, because structural defects are formed into Fe_2O_3 thin-films

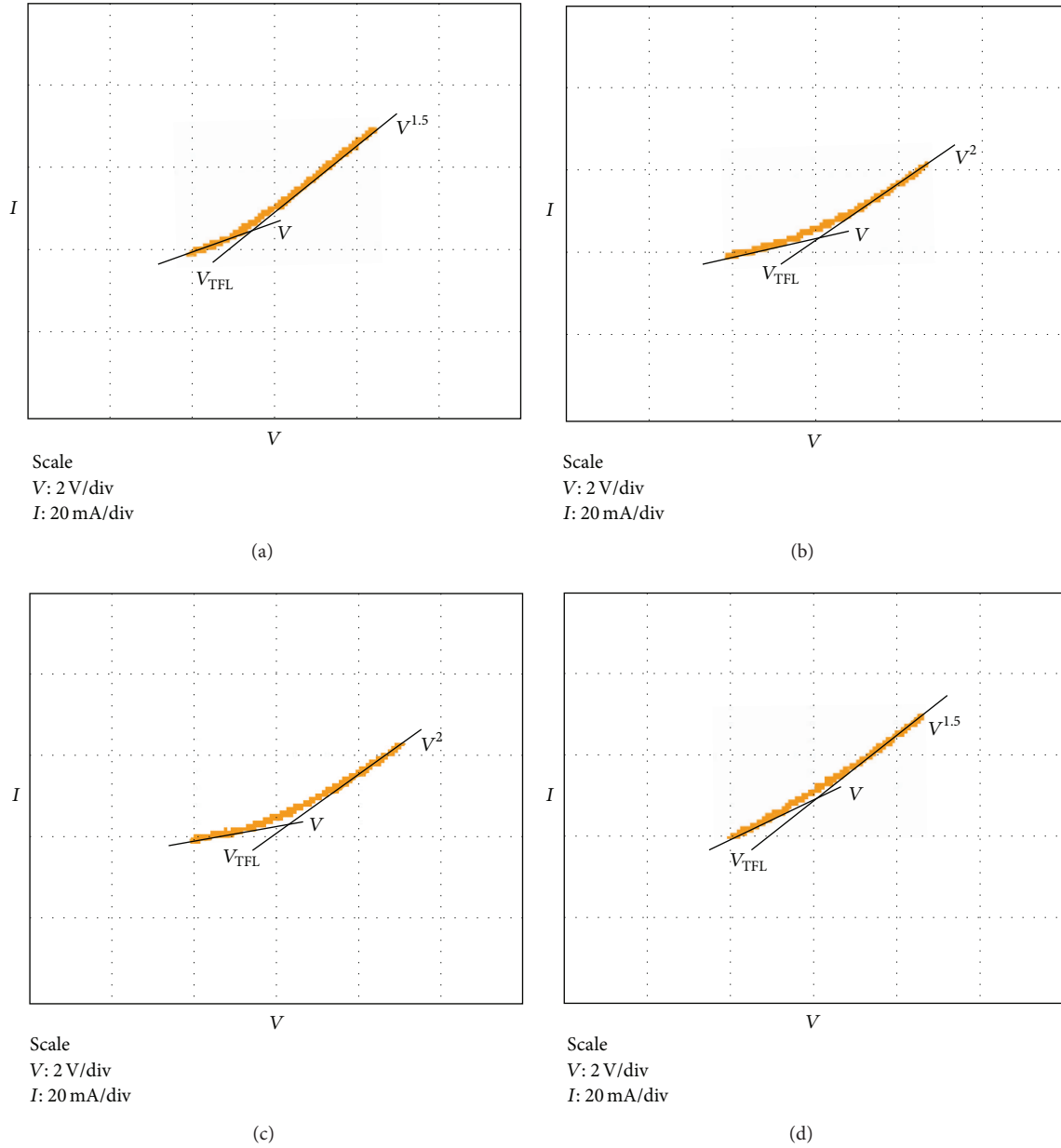


FIGURE 6: Current-voltage characteristics under reverse bias.

during the oxidation process, weak cohesive forces between Fe_2O_3 phase and copper contact allow a carriers transport with decrease of μ_{SCL} under reverse bias. Finally, increase of average roughness, R_{avg} , and smaller crystalline size, D , in correlation with changes of charge carrier mobility, μ_{SCL} , is a consequence of space-charge-limited transport in Fe_2O_3 thin-films.

4. Conclusion

Nonlinear-electronic transport from Fe_2O_3 thin-films was studied by current-voltage characteristics as a function of the oxidation temperature. Both average roughness and grain

size were demonstrated by atomic force microscopy and X-ray diffraction studies. Transport parameters were evaluated for all samples at room temperature. Space-charge effects were related to the formation of discontinuous oxide based on discontinuous grain growth during the oxidation process at intermediate temperatures. Analysis of current-voltage characteristics shows ohmic regime at low voltages and space-charge-limited regime at higher voltages.

Further, the iron oxide samples with lower critical thickness of 250 nm can be useful for the designing of adaptive oxide electronic devices, because the current flow in the Fe_2O_3 thin-films with low carrier mobility and low energy level of the traps, can be gradually modulated.

Conflict of Interests

The author declares that there is no conflict of interests, such as financial gain, but there is a direct interest regarding the publication of this paper to share knowledge in this area.

Acknowledgments

The process and results obtained in this work have been possible thanks to the previous support of Dr. Ramón Peña Sierra from CINVESTAV-IPN and Dr. Juan Vicente Méndez Méndez from CNMN-IPN, Mexico.

References

- [1] Y.-C. Chao, M.-C. Ku, W.-W. Tsai et al., "Polymer space-charge-limited transistor as a solid-state vacuum tube triode," *Applied Physics Letters*, vol. 97, no. 22, Article ID 223307, 2010.
- [2] S. Brimley, M. S. Miller, and M. J. Hagmann, "Field emission in air and space-charge-limited currents from iridium-iridium oxide tips with gaps below 100 nm," *Journal of Applied Physics*, vol. 109, no. 9, Article ID 094510, 2011.
- [3] J. Kim, K. No, and C. J. Lee, "Growth and field emission of carbon nanotubes on electroplated Ni catalyst coated on glass substrates," *Journal of Applied Physics*, vol. 90, no. 5, pp. 2591–2594, 2001.
- [4] J. Cao and J. Wu, "Strain effects in low-dimensional transition metal oxides," *Materials Science and Engineering R*, vol. 71, no. 2–4, pp. 35–52, 2011.
- [5] C.-Y. Chen, Y.-C. Chao, H.-F. Meng, and S.-F. Horng, "Light-emitting polymer space-charge-limited transistor," *Applied Physics Letters*, vol. 93, no. 22, Article ID 223301, 2008.
- [6] A. S. Aricò, P. Bruce, B. Scrosati, J.-M. Tarascon, and W. Van Schalkwijk, "Nanostructured materials for advanced energy conversion and storage devices," *Nature Materials*, vol. 4, no. 5, pp. 366–377, 2005.
- [7] P. LeMinh, H. Gokcan, J. C. Lodder, and R. Jansen, "Magnetic tunnel transistor with a silicon hot-electron emitter," *Journal of Applied Physics*, vol. 98, no. 7, Article ID 076111, 2005.
- [8] P. Kumar, A. Jain, M. Shukla, and S. Chand, "Space charge limited current in Schottky diode with single level traps," *Indian Journal of Pure and Applied Physics*, vol. 49, no. 6, pp. 406–409, 2011.
- [9] L. Dulau, S. Pontarollo, A. Boimond, J.-F. Garnier, N. Giraudo, and O. Terrasse, "A new gate driver integrated circuit for IGBT devices with advanced protections," *IEEE Transactions on Power Electronics*, vol. 21, no. 1, pp. 38–43, 2006.
- [10] S. A. Moiz, M. M. Ahmed, K. S. Karimov, F. Rehman, and J.-H. Lee, "Space charge limited current-voltage characteristics of organic semiconductor diode fabricated at various gravity conditions," *Synthetic Metals*, vol. 159, no. 13, pp. 1336–1339, 2009.
- [11] A. Cotton and G. Wilkinson, *Advanced Inorganic Chemistry*, John Wiley & Sons, New York, NY, USA, 4th edition, 2008.
- [12] R. Baca, "Structural characterization of the chromium-iron alloy formed by thermal diffusion processes," *Advanced Materials Research*, vol. 651, pp. 284–288, 2013.
- [13] P. Liao and E. A. Carter, "Hole transport in pure and doped hematite," *Journal of Applied Physics*, vol. 112, pp. 1–13, 2012.
- [14] R. F. G. Gardner, F. Sweett, and D. W. Tanner, "The electrical properties of alpha ferric oxide—II. Ferric oxide of high purity," *Journal of Physics and Chemistry of Solids*, vol. 24, no. 10, pp. 1183–1186, 1963.
- [15] F. J. Morin, "Electrical properties of α -Fe₂O₃," *Physical Review*, vol. 93, no. 6, pp. 1195–1199, 1954.
- [16] P. Liao, M. C. Toroker, and E. A. Carter, "Electron transport in pure and doped hematite," *Nano Letters*, vol. 11, no. 4, pp. 1775–1781, 2011.
- [17] N. Cabrera and N. F. Mott, "Theory of the oxidation of metals," *Reports on Progress in Physics*, vol. 12, no. 1, pp. 163–184, 1949.
- [18] D. Dorner, S. Zaeferrer, L. Lahn, and D. Raabe, "Overview of microstructure and microtexture development in grain-oriented silicon steel," *Journal of Magnetism and Magnetic Materials*, vol. 304, no. 2, pp. 183–186, 2006.
- [19] A. S. Grove, *Physics and Technology of Semiconductor Devices*, John Wiley & Sons, New York, NY, USA, 1st edition, 1967.
- [20] G. Ertl, "Thermodynamics of gas-surface interactions," *Pure & Applied Chemistry*, vol. 61, no. 6, pp. 1001–1007, 1989.
- [21] P. F. Fewster, *X-Ray Scattering from Semiconductors*, Imperial College Press, Singapore, 2nd edition, 2003.
- [22] H. Kashani, "Structural, electrical and optical properties of zinc oxide produced by oxidation of zinc thin films," *Journal of Electronic Materials*, vol. 27, no. 7, pp. 876–882, 1998.
- [23] S. Blundell, *Magnetism in Condensed Matter*, Oxford University Press, Oxford, UK, 2nd edition, 2008.
- [24] E. Y. Tsymbal and I. Zutic, *Handbook of Spin Transport and Magnetism*, CRC Press/Taylor & Francis Group, Boca Raton, Fla, USA, 1st edition, 2012.
- [25] J. J. O'Dwyer, *The Theory of Electrical Conduction and Breakdown in Solid Dielectrics*, Clarendon Press Oxford, 1st edition, 1973.
- [26] M. Lundstrom, *Fundamentals of Carrier Transport*, Cambridge University Press, New York, NY, SA, 2nd edition, 2000.
- [27] D. H. Zhang and H. L. Ma, "Scattering mechanisms of charge carriers in transparent conducting oxide films," *Applied Physics A*, vol. 62, no. 5, pp. 487–492, 1996.

Research Article

Application of Macrofiber Composite for Smart Transducer of Lamb Wave Inspection

Gang Ren and Kyung-Young Jhang

School of Mechanical Engineering, Hanyang University, Seoul 133-791, Republic of Korea

Correspondence should be addressed to Kyung-Young Jhang; kyjhang@hanyang.ac.kr

Received 4 October 2013; Accepted 20 October 2013

Academic Editor: Kean Aw

Copyright © 2013 G. Ren and K.-Y. Jhang. This is an open access article distributed under the Creative Commons Attribution License, which permits unrestricted use, distribution, and reproduction in any medium, provided the original work is properly cited.

Macrofiber composite (MFC) has been developed recently as a new type of smart material for piezoelectric transducers. It shows advantages over traditional piezoelectric ceramic materials (PZT) including the method of application, sensitivity, and cost. It can be embedded on the structure, which provides the possibility to monitor the structural health in real time. In this paper, the feasibility of this transducer for the Lamb wave inspection has been experimentally explored. A pair of MFC patches is bonded on a 2 mm thick aluminum plate, and it has been demonstrated that the dispersive characteristics of S0 and A0 modes, generated and detected by MFC patches, agreed well with the theory. The influence of the bonding condition of the transducer was also tested to show that rigid bonding is required to assure a high amplitude signal. In order to illustrate the performance of defect detection, an artificial defect fabricated on the surface of a specimen was inspected in the pitch-catch mode. The results showed that the MFC transducer is a promising Lamb wave transducer for nondestructive testing (NDT) and structural health monitoring (SHM).

1. Introduction

With a view to enhance the safety and reliability in non-destructive evaluation (NDE), the development of highly efficient techniques for nondestructive damage detection or structural health monitoring is of vital significance [1]. Such SHM requires small, lightweight, cheap, and sensitive smart transducers to be embedded on the surface of the structure at affordable cost, especially in the aerospace field. In addition, the traditional PZT is not suitable for this situation because of limitations such as being monolithic, inflexible, and brittle.

In order to make up for these limitations, a series of smart material transducers was developed in the past two decades. Piezoelectric films (PVDFs) have been used in SHM system [2–4]. Compared to the traditional PZT transducers, they have some advantages of durability and flexibility, but due to poor electromechanical coupling efficiency, they need greater actuation power in generation and heavy amplification in detection [5]. There are other transducers, including active fiber composites (AFCs) and macrofiber composites (MFCs) developed at NASA Langley Research Center, and these transducers avoid some of the limitations of PVDFs.

AFCs and MFCs are composed of thin piezoceramic fibers sandwiched between layers of adhesive, electrodes, and a polyimide film [6]. These types of transducers produce higher force and strain than the typical monolithic piezoceramic materials [7, 8]. The main advantage of MFCs over AFCs is the reduced manufacturing cost, owing to the fibers being sliced into rectangular shapes for MFCs, while the circular AFC fibers are manufactured through a very costly extrusion process [9].

Thus, the developed MFC patch is a promising alternative to the traditional brittle PZT. Also, it is appealing for SHM due to its advantages of flexibility, durability, sensitivity, and reliability. Many researchers have engaged in applying this kind of composite transducer to the nondestructive evaluation field, such as welding defect detection, pipeline inspection, and structural health monitoring [1, 3, 10, 11].

In this paper, we focused on the feasibility of using MFC patches for the Lamb wave inspection. For this, a pair of MFC patches was bonded onto a 2 mm thick aluminum plate, and the Lamb wave was transmitted and received. The influence of bonding condition of the MFC patch on the Lamb wave signal was also investigated, including the poorly adhered

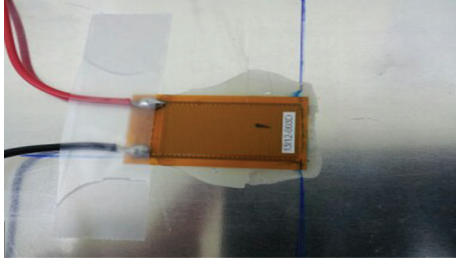


FIGURE 1: MFC Type P1 M2814 (made by Smart Material Corp.).

TABLE 1: Properties of MFC Type P1 M2814.

Operational voltage	-500 V~1500 V
Active dimensions	28 mm × 14 mm
Overall dimension	38 mm × 20 mm
Capacitance	0.61 ppm
Free strain	1550 ppm
Thickness	300 μ m
Actuator bandwidth	0 Hz~700 KHz
Sensor bandwidth	0 Hz~1 MHz

and the correctly adhered bonding conditions and the use of two kinds of couplants (longitudinal wave couplant and shear wave couplant). In order to illustrate the performance of defect detection, an artificial defect was fabricated on the surface of the specimen which was inspected in the pitch-catch mode.

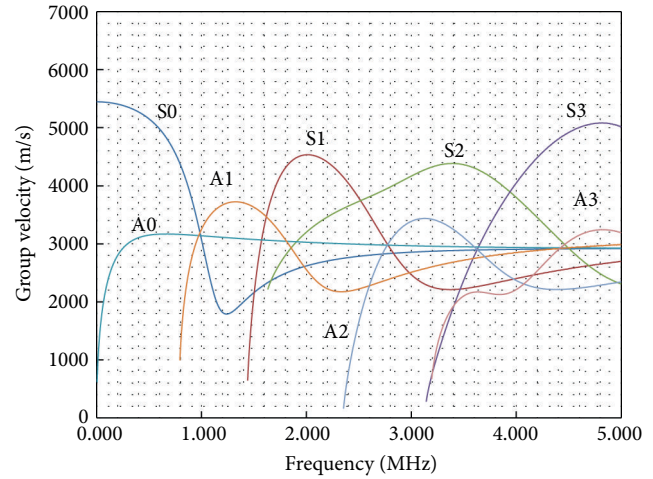
2. MFC Transducer

The typical type of MFC transducer tested in this paper is an M2814-P1 (Smart Material Corp.), which is shown in Figure 1. This type of MFC, which is available in d33 operational mode, actuates and senses along the length of the MFC patch. The specific information is listed in Table 1.

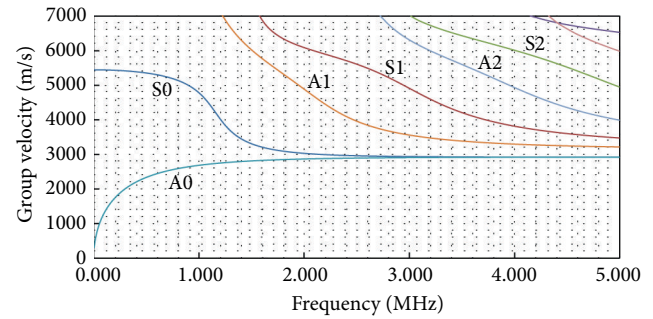
3. Experiments and Results

3.1. Dispersion Curves. In our study, a 2 mm thick aluminum alloy plate was used as specimen. Initially, the theoretical dispersion curves of the relevant Lamb waves were calculated. These are presented, in terms of phase velocity and group velocity, in Figures 2(a) and 2(b). S_i and A_i indicate the symmetric and antisymmetric modes ($i = 0, 1, 2, \dots$), respectively. They will be used for mode identification and to predict the time of flight of a specific mode.

3.2. Excitation and Detection of the Lamb Wave Using MFC Patches. Figure 3 shows the experimental set-up to demonstrate the performance of MFC patches to excite and detect the Lamb waves. A pair of MFC patches was bonded on the surface of the plate; one MFC patch was used as an actuator to generate the Lamb waves and the other was used as a



(a)



(b)

FIGURE 2: (a) Group velocity dispersion curves. (b) Phase velocity dispersion curves.

sensor to receive the wave signal. A high power tone-burst signal generator (Ritec RAM 5000, USA) was used to drive the actuator. A pulser receiver (Panametrics PR500, USA), which was connected to the sensor, was used to receive the wave signal for the pitch-catch mode inspection.

In order to determine which frequency range was suitable for the embedded MFC patches to generate and detect the Lamb waves, the input signal frequency was varied from 0.1 MHz to 0.6 MHz at 0.05 MHz intervals. This frequency range was chosen because the upper frequency limit of the MFC actuator was 0.7 MHz. From the experimental signals shown in Figure 4, it is apparent that the S_0 mode is readily detectable within the range from 0.25 MHz to 0.45 MHz, while A_0 mode is detectable between 0.2 MHz and 0.35 MHz. From these results, the 0.3 MHz frequency was selected for the input frequency to use for both of S_0 and A_0 modes.

Figure 5 shows an example of the detected signal in a time domain, and we can see that the S_0 and A_0 modes are clearly observed. This signal was short-time-Fourier transformed and overlapped on the theoretical group velocity dispersion curves to verify the Lamb wave modes. The experimental results agree closely with the theoretical dispersion curves at 0.3 MHz for both modes.

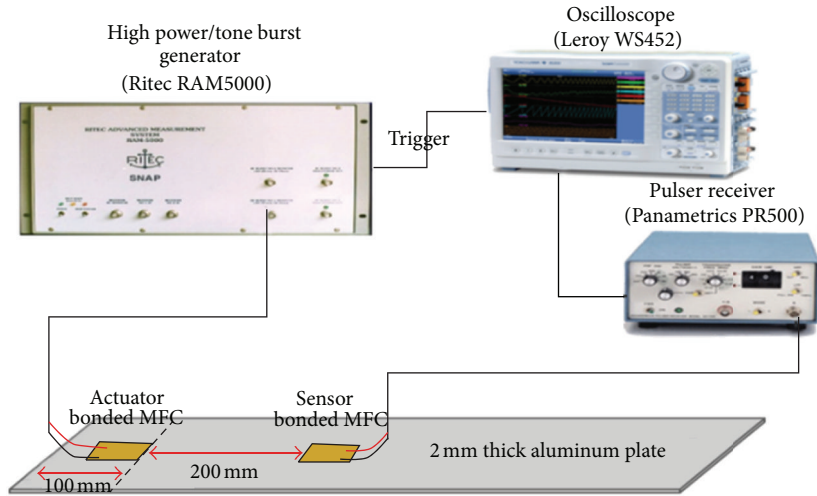


FIGURE 3: Pitch-catch measurement experiment set-up.

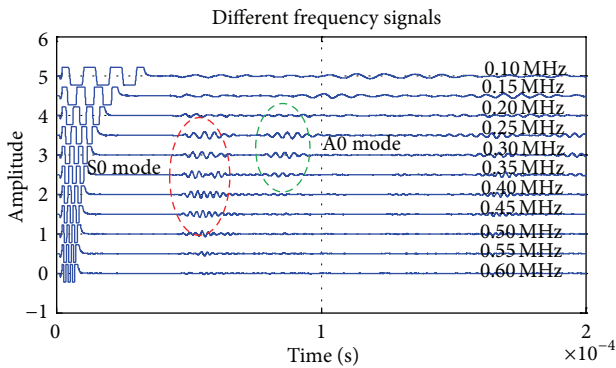
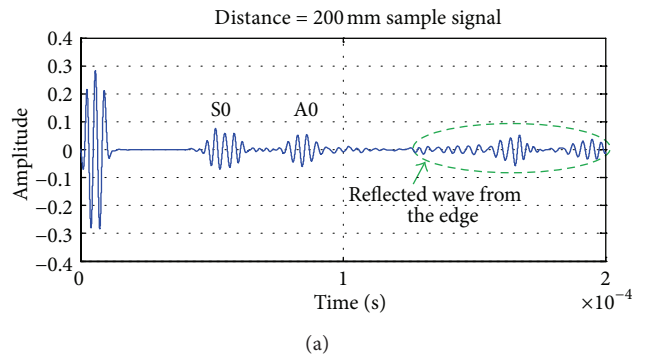
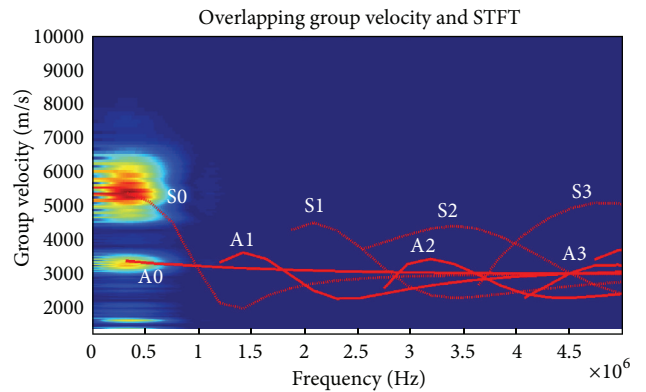


FIGURE 4: Received signals from various frequencies at 0.05 MHz intervals.



(a)



(b)

FIGURE 5: (a) The signal generated and received by MFC patches. (b) Overlapping the group velocity with STFT.

3.3. *Influence of the Bonding Condition.* As the bonding condition of MFC patch may affect the effectiveness of the actuation and sensitivity of the sensing, the quality of the bond is an important consideration in the performance of the system [12]. In order to investigate the influence of the bond quality, we tested several different bonding conditions: couplant-bonded, poorly adhered, and correctly adhered. For the correctly adhered condition, an epoxy adhesive (3M Scotch-Weld) was used, which is composed of two parts. The poorly adhered condition was obtained by using only one part of the epoxy, causing degradation in the shear and longitudinal stiffness compared to that of the mixed two-part epoxy adhesive [13].

Figure 6 shows the envelope of detected signals for each bonding condition, where the envelope of signal was obtained by using the Hilbert transform. We can see that the sensor with the correctly adhered condition produced a significantly larger output than those with poorer bonding, and thus proper bonding is very important to ensure the maximum sensitivity of the MFC patch.

3.4. *Defect Detection.* In order to further verify the performance of an MFC Lamb wave actuator sensor system for defect detection, an artificial defect on the surface of the specimen was inspected. The defect was a circular groove with diameter of 20 mm, as shown in Figure 7. We used the pitch-catch method.

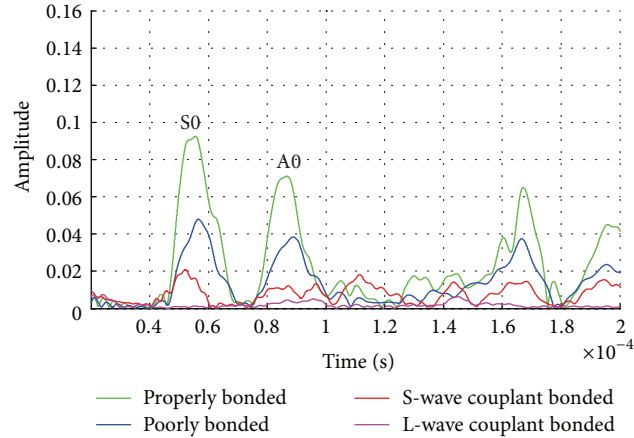


FIGURE 6: The envelope of signals obtained from different bonding conditions.

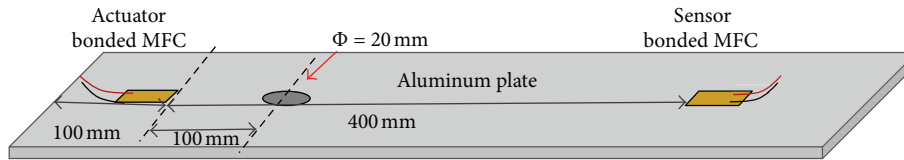


FIGURE 7: The specimen with circular defect and bonded MFC patches locations.

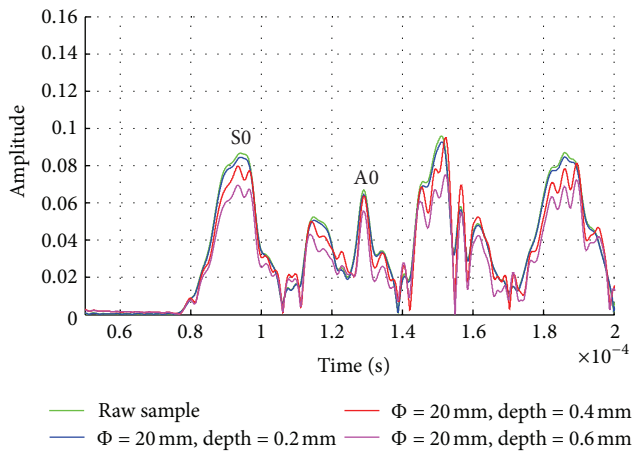


FIGURE 8: Envelope of each signal obtained from each case.

The pitch-catch method can be used to inspect structural degradation that occurs between the actuator and sensor. The main performance of the detection is to compare the Lamb wave's amplitude and time of flight with a pristine case. Due to the dispersive characteristics of the Lamb waves, which are easily influenced by the small changes in the thickness of plate, this method is suitable to detect variations in thickness.

Three different depths of defects, 0.2 mm, 0.4 mm, and 0.6 mm, were tested. In order for an easy comparison of the signal amplitude with the baseline, we processed the signals by using the Hilbert transform, which provides the envelope of signal. Figure 8 shows the results. With an increasing of the defect depth, the Lamb wave amplitude decreased

consistently. When the defect depth was 0.2 mm, which was 10% of the plate thickness, the amplitude reduction was relatively small. However, when the defect depth was 20% and 30% of the plate thickness, the amplitude was substantially reduced.

4. Conclusions

The feasibility of MFC patch transducers for structural health monitoring using the Lamb wave was experimentally demonstrated. For the experiment, a pair of MFC transducers was bonded on a 2 mm thick aluminum plate specimen. The Lamb waves were well generated and received by this pair of transducers, and the Lamb wave modes were identified by comparing with the theoretical dispersion curves. The bonding quality affected the actuation and the sensitivity of the sensing, so correct bonding is required for the MFC patch to be used for an effective application. Lamb wave inspection, using MFC patch transducer in pitch-catch mode, was also useful to detect the defect of thickness reduction. A 20% reduction of thickness was detectable. From these results, we can conclude that MFC patch transducers can be effectively used for structural health monitoring using the Lamb waves.

Acknowledgment

This work was financially supported by the National Research Foundation of Korea (NRF), Grant funded by the Korean government (NRF-2013M2A2A9043241).

References

- [1] A. B. Thein, G. Park, and C. R. Farrar, "Health monitoring of pipeline systems using macro-fiber composite active-sensor," *Steel Structures*, vol. 7, pp. 33–48, 2007.
- [2] S. B. Kim and H. Sohn, "Instantaneous reference-free crack detection based on polarization characteristics of piezoelectric materials," *Smart Materials and Structures*, vol. 16, no. 6, pp. 2375–2387, 2007.
- [3] V. Giurgiutiu, "Tuned Lamb wave excitation and detection with piezoelectric wafer active sensors for structural health monitoring," *Journal of Intelligent Material Systems and Structures*, vol. 16, no. 4, pp. 291–305, 2005.
- [4] H. A. Sodano, G. Park, and D. J. Inman, "An investigation into the performance of macro-fiber composites for sensing and structural vibration applications," *Mechanical Systems and Signal Processing*, vol. 18, no. 3, pp. 683–697, 2004.
- [5] M. Barbezat, A. J. Brunner, P. Flueler, C. Huber, and X. Kornmann, "Acoustic emission sensor properties of active fibre composite elements compared with commercial acoustic emission sensors," *Sensors and Actuators A*, vol. 114, no. 1, pp. 13–20, 2004.
- [6] <http://www.smartmaterials.com/>.
- [7] Q. Q. Zhang, S. J. Gross, S. Tadigadapa, T. N. Jackson, F. T. Djuth, and S. Trolier-McKinstry, "Lead zirconate titanate films for d33 mode cantilever actuators," *Sensors and Actuators A*, vol. 105, no. 1, pp. 91–97, 2003.
- [8] X. Lin and F. G. Yuan, "Diagnostic Lamb waves in an integrated piezoelectric sensor/actuator plate: analytical and experimental studies," *Smart Materials and Structures*, vol. 10, no. 5, pp. 907–913, 2001.
- [9] R. B. Williams, G. Park, D. J. Inman, and W. K. Wilkie, "An overview of composite actuators with piezoceramic fibers," in *Proceedings of the 20th International Modal Analysis Conference*, pp. 421–427, Los Angeles, Calif, USA, February 2002.
- [10] H. M. Matt and F. L. di Scalea, "Macro-fiber composite piezoelectric rosettes for acoustic source location in complex structures," *Smart Materials and Structures*, vol. 16, no. 4, article 064, pp. 1489–1499, 2007.
- [11] A. B. Thien, H. C. Chiamori, J. T. Ching, J. R. Wait, and G. Park, "The use of macro-fibre composites for pipeline structural health assessment," *Structural Control and Health Monitoring*, vol. 15, no. 1, pp. 43–63, 2008.
- [12] F. L. di Scalea, H. Matt, I. Bartoli, S. Coccia, G. Park, and C. Farrar, "Health monitoring of UAV wing skin-to-spar joints using guided waves and macro fiber composite transducers," *Journal of Intelligent Material Systems and Structures*, vol. 18, no. 4, pp. 373–388, 2007.
- [13] http://solutions.3m.com/wps/portal/3M/en_US/Adhesives/Tapes/Products/~3M-Tape-and-3M-Adhesives/Structural-Adhesives?N=5024768&rt=c3.

Research Article

Effect of Magnesium Sulphate on Self-Compacting Concrete Containing Supplementary Cementitious Materials

Aiad Hassan,¹ Hilmi Bin Mahmud,¹ Mohd. Zamin Jumaat,¹
Belal ALsubari,¹ and Aziz Abdulla²

¹ Department of Civil Engineering, University of Malaya Malaysia, Kuala Lumpur, Malaysia

² Departments of Civil Engineering, Tikrit University, Tikrit, Iraq

Correspondence should be addressed to Aiad Hassan; ayaadhamed@yahoo.com

Received 15 August 2013; Revised 22 September 2013; Accepted 25 September 2013

Academic Editor: Kean Aw

Copyright © 2013 Aiad Hassan et al. This is an open access article distributed under the Creative Commons Attribution License, which permits unrestricted use, distribution, and reproduction in any medium, provided the original work is properly cited.

The length change is negligible and can be attributed to the normal distension of concrete. On the other hand, concrete suffering from mass loss gives a good indicator about the durability of SCC. Permeability of concrete is an important factor in classifying its durability generally; concrete with low Permeability will afford better protection of the reinforcement within it than concrete with high Permeability. In this paper, the assessment of magnesium sulphate (MS) attack on concrete containing various ratios of the supplementary cementitious materials (SCM) was investigated for concrete containing FA, RHA, and GGBS with cement replacement levels of 15%, 10%, and 5%, respectively, based on the selected samples from the concrete to the statement of the effect of magnesium on some of the characteristics of concrete such as compressive strength, height, and weight compared with similar samples but under laboratory conditions dry and moist water treatment. Test results showed that the SCC content SCM appear to have higher strength values than those stored in water and air sample; the highest value of mass loss is recorded for the control mixture compared with concrete content SCM, and the change in length in curing concrete is much less relative to the change for concrete immersed in MS.

1. Introduction

The external attack of sulphate salts is considered as one of the major problems affecting concrete durability. Sulphates are highly soluble salts in the form of sodium sulphate (Na_2SO_4), calcium sulphate (CaSO_4), potassium sulphate (K_2SO_4), and magnesium sulphate (MgSO_4). Sulphate attack is a process in which sulphates react with various phases of hydrated cement paste leading to deterioration of the concrete matrix through spalling, softening, and mass loss, which may lead to expansion and loose strength and elasticity. It is recognized as a complex process due to the effect of numerous controlling factors [1, 2].

It has been reported that the addition of mineral admixtures to concrete would enhance its resistance to sulphate attack [2]. One of the most promising mineral admixtures is the rice husk ash (RHA), rice husk is an agricultural residue from the rice milling process. According to the FAO annual report of the United Nations [3], the annual world rice production in 2007 was estimated to be 649.7 million tons,

of which the husk constitutes approximately 20 wt% thereof. Burning the husk at the controlled temperature below 800° can produce ash with silica mainly in amorphous form [4–6]. Based on previous studies RHA has not been utilized yet in the construction industry with the exception of repair works at the Bowman Dam in northern California's Sierra Nevada Mountains, USA; it showed positive results in a dry-mix shotcrete [7]. The reason for not utilising this material is probably due to the lack of understanding of the characteristics of the RHA blended concrete. Many researchers have already published articles about the properties of the blended RHA concrete, such as strength and durability; nonetheless, the effect of RHA on concrete resistance to sulphate attack with SCC was investigated limitedly.

Fly ash is divided into two classes: Class-F and Class-C. Class-F fly ash is normally produced from the burning of anthracite or bituminous coal and has pozzolanic properties but little or no cementitious properties. Class-C fly ash is normally produced from the burning of lignite or subbituminous coal and has some autogenous cementitious

TABLE 1: Specific gravity and water absorption of coarse and fine aggregate.

Aggregate	Specific gravity			Absorption (%)
	Oven-dry	SSD	Apparent	
Granite	2.40	2.61	3.04	1.43
Fine aggregate (river sand)	2.31	2.39	2.50	2.38

TABLE 2: Chemical composition of binder materials.

Constituents (wt %)	OPC	RHA	(FA)	GGBS
SiO ₂	16.5	90.55	41.29	35
Fe ₂ O ₃	3.633	0.91	12.36	0.52
CaO	69.43	1.23	1.0	40
MgO	1.29	0.44	2.62	8
K ₂ O	0.489	5.52	2.49	0.46
SO ₃	4.23	0.81	3.0	2.09
Al ₂ O ₃	3.65	0.67	23.59	11.72
LOI	2.14	2.62	6	1.42
Physical properties				
Specific surface area (m ² /kg)	320	350	570	450
Specific gravity	3.14	2.15	2.6	2.1

properties [8]. However, most fly ashes that are being used in concrete production are Class-F. The use of fly ash influences compressive strength, workability, heat of hydration, sulphate resistance, permeability, and the alkali-silica reaction of concrete [9].

Ground granulated blast furnace slag (GGBS) is a waste product in the manufacture of pig iron, in which about 300 kg of slag is produced for each tonne of pig iron [10]. When this slag is rapidly quenched and ground, it will possess latent cementitious properties. After processing, the material is known as GGBS. The hydraulic properties may vary and can be separated into grades according to ASTM C989 [11].

The objectives of this paper are to assess and find the best indicator for concrete deterioration due to accelerated sulphate attack and to investigate the effect of RHA, FA, and GGBS on concrete resistance to sulphate attack. The chemical properties of SCM and control mix using OPC were investigated. Mixture proportioning was performed to produce high workability concrete (600–700 mm slump flow) with target strength of 40 MPa for the control mixture. A total of four concrete mixtures were immersed in the MS solution. The sulphate attack for the concrete specimens was assessed by the subsequent testing of the changes in the compressive strength, length, and mass.

2. Constituent Material

2.1. Aggregates. The maximum size of coarse aggregate used was 14 mm. The results of the specific gravity and absorption for the normal coarse aggregate and normal sand are presented in Table 1.

2.2. Ordinary Portland Cement. Locally manufactured ordinary Portland cement conforming to MS 522: Part1: 2003 Typel was used for all mixtures.

2.3. Rice Husk Ash (RHA). The detailed chemical analysis is summarized in Table 2 for RHA. It contains 87–97% of silica with small amounts of alkali and other trace elements [12].

2.4. Fly Ash (FA). The replacement of cement by fly ash in the production of concrete is possible up to 50% [9]. The fly ash used in this experiment meets the requirement of BS EN 450 : 1995. It was used as 15% replacement of cement, which leads to an improvement in the strength of concrete to more than 40 MPa as shown in Table 2.

2.5. Ground Granulated Blast Furnace Slag (GGBS). Details of the chemical analysis are summarized in Table 2 for (GGBS). The fineness of GGBS is usually greater than 350 m²/kg and occasionally in excess of 500 m²/kg; the specific gravity is 2.9 [11]. In this study, the GGBS fineness of 450 m²/kg was used. The raw material for GGBS, raw slag, is usually obtained from a predetermined steel plant, which ensures the stability of the raw material. The chemical composition and physical properties of the binder are illustrated in Table 2.

2.6. Superplasticizer. The superplasticizer used in this study was (SP-1600). It is an aqueous solution of modified polycarboxylate copolymers that meets the requirements of ASTM C494-86 Type G and BS 5075: Part 3. It facilitates extreme water reduction, excellent flowability with optimal cohesion, and strong self-compacting concrete. It did not contain chlorides or other ingredients that promote steel corrosion.

3. Experimental Programme

In this experiment, four parameters were investigated, SCC with ordinary Portland cement (OPC), fly ash (FA), rice husk ash (RHA), and ground granulated blast furnace slag (GGBS). In the SCCOPC, three mixes with different quantities of cement were used.

Three percentages were used for the experiments with FA, RHA, and GGBS. Details of the above-mentioned experimental work plan are shown in Figure 1.

3.1. Mix Design. The Japanese concept of design of SCC is based on a method proposed by Okamura and Ozawa [13]. The authors proposed a simple mix-proportioning system assuming a general supply from ready-mixed concrete plants. In this paper, the mix design proposed included the following.

- (1) Coarse aggregate content which was fixed at 45% of the solid volume.
- (2) Fine aggregate content which was fixed at 55% of the mortar volume.

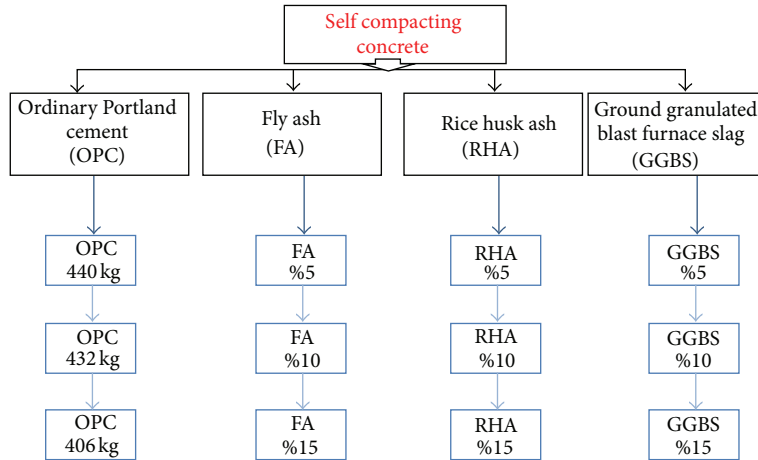


FIGURE 1: Mix proportions of various mixes.

TABLE 3: Selected mix proportion of SCC with various supplementary material ratios.

Mix. No.	W/p %	Cement (kg)	F.A (kg)	C.A (kg)	Water (kg)	S.P (kg)	Pozzolanic materials (FA,RHA,GGBS)
SCCOPC	0.53	406	895	732	215	2	0
SCCFA (15%)	0.53	349	895	732	201	2	57
SCCRHA (10%)	0.53	368	895	732	201	2	38
SCCGGBS (5%)	0.53	388	895	732	201	2	18

C.A: coarse aggregate, F.A: fine aggregate, SP: superplasticizer.

- (3) Water-powder ratio in volume was assumed as 1.2 to 2.0 depending on the properties of the powder and cement.
- (4) Superplasticizer dosage and the final water-powder ratio were determined so as to ensure the self-compactability.

Table 3 depicts the properties of the mix proportion and selected mix proportion of SCC for the final mix.

4. Methodology

A magnesium sulphate hydrate dissolved in water with a content of 5 wt% was used in the study as a salt. All the specimens that were subjected to sulphate attack were initially cured in water for 7 days after remoulding. They were then immersed in the magnesium sulphate solution. The sulphate treatment was done in three cycles; each cycle consisted of 30 days of sulphate immersion followed by 7 days of air drying and tests were conducted at the end of each cycle. The sulphate solution was replaced every 15 days in each cycle.

The length and mass changes were monitored on three concrete cube specimens of 100 × 100 × 100 mm. For length change measurements, four readings were taken from each specimen at the end of each immersion cycle. The average length was then recorded and the results were expressed as a percentage with respect to the length changes, with the other samples left in the curing tank at the same age and during the drying age.

5. Fresh Concrete Properties

The fresh properties are given in Table 4 for all concrete mixtures incorporating RHA, FA, and GGBS; no bleeding or segregation was detected. The fresh density was in the range of 2280–2440 kg/m³, which characterizes all the relevant workability aspects and hence each mix was tested with different method for the different workability parameters. The slump flow test was used to assess the horizontal free flow of SCC in the absence of obstructions. Time $T_{50\text{cm}}$ is the secondary indicator of the flow funnel; it indicates the tendency for segregation, wherein the funnel can be refilled with concrete and left for 5 minutes to settle. The L-box test was used to determine the passing ability. The results could be estimated according to the limits of the standard for SCC concrete.

6. Results and Discussion

6.1. Comparing the Effect of MS with Curing Condition on SCC. The results illustrated in Table 5 and Figure 2 explain the compressive strength between the concrete immersed in MS and the standard curing of the concrete. The figures show the improvement of the strength immersed in MS relative to the strength of curing with water on all concrete mixed with the SCM products, such as FA, RHA, and GGBS. This can be attributed to the formation of the expansive ettringite in the presence of tricalcium aluminate inside the cement paste

TABLE 4: Results of workability fresh SCC containing SCM.

Mix.no.	V-funnel (sec)	T ₅₀ (sec)	Slump flow (mm)	L-BOX %	Segregation %	J-ring (mm)
SCCOPC	5	4	610	85	4%	10
SCCFA15	7	5	610	89	6%	10
SCCRHA10	9	5	630	81	7%	13
SCCGGBS5	8	6	650	82	15%	15

TABLE 5: Effect of MS on the strength with curing SCC.

Mix. no.	Compressive strength/MPa						Relative strength % (a/b)		
	Magnesium sulphate (a)			Water curing (b)			44 d	81 d	118 d
	44 d	81 d	118 d	44 d	81 d	118 d			
SCCOPC	42	44	48	40	42	46	1.05	1.05	1.04
SCCFA15	52	53	54	50	52	53	1.04	1.02	1.02
SCCRHA10	51	53	56	41	43	46	1.24	1.23	1.22
SCCGGBS5	52	53	54	47	48	49	1.11	1.10	1.10

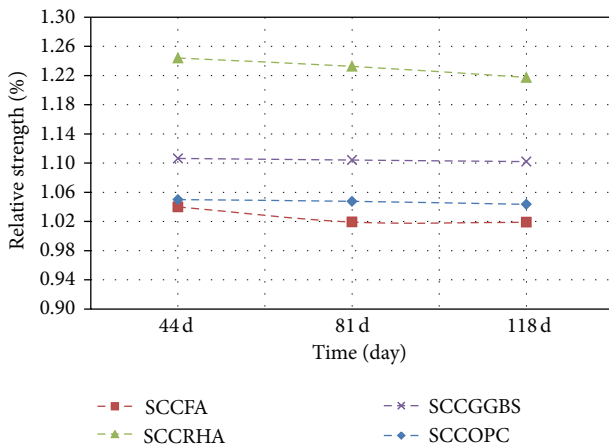


FIGURE 2: Effect of MS on the strength with curing water SCC.

matrix and the infiltrated SO_4^{+} ion, which resulted in filling the voids, thus increasing the concrete maturity [14].

In this study, it can also be observed from the compressive strength results that all concrete specimens immersed in MS up to the third cycle (111d of sulphate exposure) containing FA exhibited higher values than others types of concrete containing RHA and GGBS because the SO_4^{+} ion contents in FA are higher than for the RHA and GGBS, which causes the voids to be filled look better and the strength to develop quicker, as explained in Table 2.

6.2. Comparison between Magnesium Sulphate and Air Drying Strength SCC. For the values of the compressive strength for the hardened concrete mixtures immersed in sulphate, “the control drying specimens” along with the relative compressive strength when tested at the same age are shown in Table 6. It can be observed that the relative strength of the concrete immersed in sulphate compared to those air dried increased with concrete containing SCM, such as FA, RHA, and GGBS in less time. For example, the relative strength for the 15 FA mixtures was 16% at the first cycle (37 days of sulphate exposure). However, in the third cycle (111 days), the

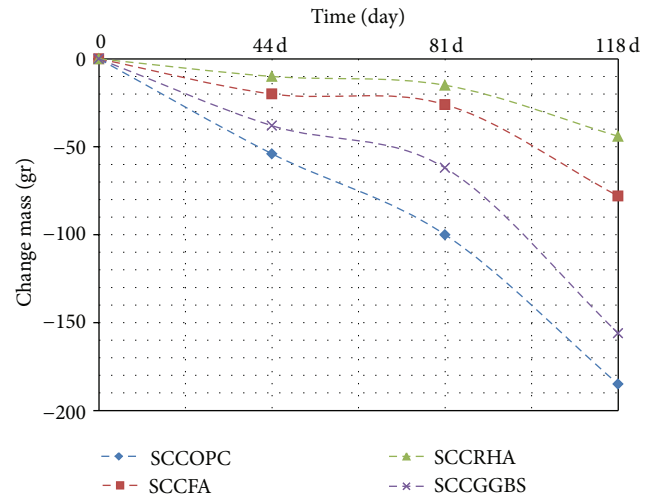


FIGURE 3: Effect of change in mass between MS and water curing.

value was reduced to 8%. In addition, the value of the relative strength also decreased for 10 RHA and 5 GGBS. Because increase the binder material and need to be treated with water causing incomplete interaction between the components of the concrete, causing shrinkage of concrete and thus affected to the durability of concrete [15].

The effect of the MS attack on the cement paste showed that specimens immersed in the MgSO_4 solution at room temperature exhibited a higher compressive strength than specimen’s air dried for up to 120 days. At later ages, the adverse effect of sulphate on strength was dominant [15].

6.3. Effect of Magnesium Sulphate on Change in Mass. The change in mass for the concrete exposures to sulphate up to 118 days compared with the mass stored in water and drying specimens in the laboratory taken at the same ages is given in Figures 3 and 7. The results show that the highest value of mass loss is recorded for the control mixture, which has a loss of mass at the curing case in the third cycle of display. In as much as the loss of mass for the 10 RHA, 15 FA and

TABLE 6: Effect of MS on the strength with air drying SCC.

Mix. no.	Compressive strength (MPa)						Relative strength %		
	Sulphate solution			Air dried			44 d	81 d	118 d
	44 d	81 d	118 d	44 d	81 d	118 d			
SCCOPC	42	44	48	39	41	44	1.08	1.07	1.09
SCCFA15	52	53	54	45	46	50	1.16	1.15	1.08
SCCRHA10	51	53	56	44	45	49	1.16	1.18	1.14
SCCGGBS5	52	53	54	43	45	47	1.21	1.18	1.15

TABLE 7: Effect of MS on the mass with air drying SCC.

Mix. no.	Mass (gr)						Curing water		
	Magnesium sulphate			Air dried			44 d	81 d	118 d
	44 d	81 d	118 d	44 d	81 d	118 d			
SCCOPC	2220	2240	2240	2222	2206	2202	2274	2340	2425
SCCFA15	2460	2414	2402	2334	2332	2320	2480	2440	2480
SCCRHA10	2365	2353	2342	2272	2265	2200	2375	2368	2386
SCCGGBS5	2332	2320	2242	2246	2266	2280	2370	2382	2398

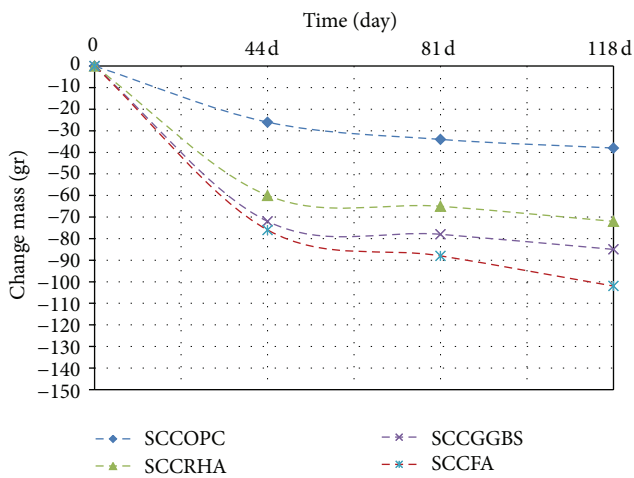


FIGURE 4: Effect on MS with air dried at SCC containing SCM.

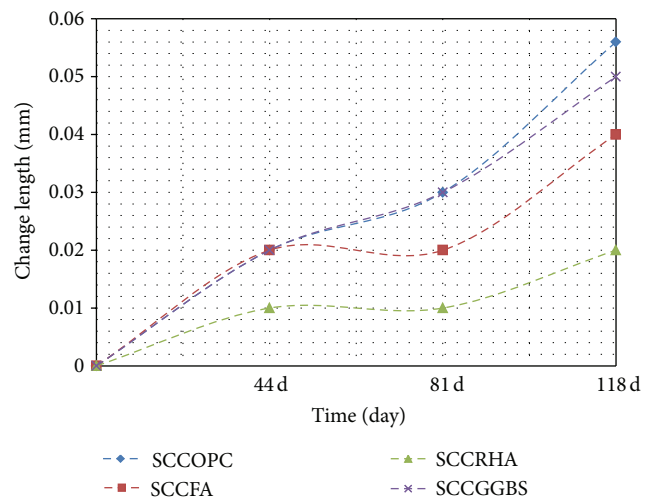


FIGURE 6: Length affected by MS and air dried in SCC.

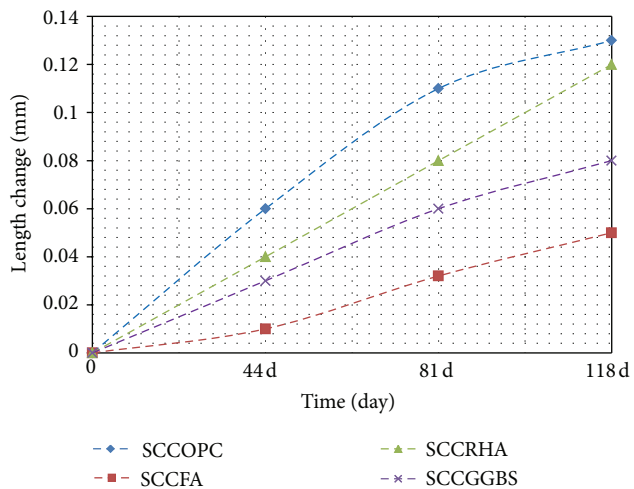


FIGURE 5: Length affected by the addition of MS and curing ages at SCC.

5GGBS were less than the control mix; the RHA blended cement concrete results in better resistance to sulphate attack; therefore, the mass loss can be a measure of sulphate attack due to the gypsum formation. Polviska postulated/reported that the loss of mass is the best indicator to assess the degree of deterioration compared to changes in length and strength [16].

In the drying test, for all mixes the reduction in weight can be attributed to the formation of gypsum on the concrete surface which also results in the softening and spalling of the concrete surface. In addition, the presence of SCM leads to more shrinkage in FA, GGBS, and RHA, respectively compared with control mix. The reason it surface area of these materials and thus leads to reduce the weight (see Figure 4, Table 7).

The drying shrinkage tends to decrease in SCC since a very small amount of free water is available in the system.

TABLE 8: Length affected by the addition of MS and curing ages at SCC.

Mix. no.	Magnesium sulphate			Length at (mm)			Air dried		
				Curing age					
	44 d	81 d	118 d	44 d	81 d	118 d	44 d	81 d	118 d
SCCOPC	100.400	100.37	100.36	100.46	100.48	100.49	100.40	100.40	100.39
SCCFA	100.36	100.36	100.34	100.37	100.39	100.39	100.38	100.38	100.38
SCCRHA	100.38	100.34	100.34	100.42	100.42	100.46	100.4	100.37	100.39
SCCGGBS	100.39	100.39	100.34	100.42	100.45	100.42	100.40	100.40	100.39



(a) SCCFA



(b) SCCRHA



(c) SCCOPC



(d) SCCGGBS

FIGURE 7: Optical observation of the concrete exposed to MS, water and the drying age of SCC containing various SCM.

Also, SCC has minimum empty voids on the concrete surface that are largely responsible for drying shrinkage [17].

6.4. Effect of Magnesium Sulphate on Length Change at SCC.

The percentage of expansion for the concrete exposed to sulphate for up to 118 days compared with the length at curing and drying for the same ages is given in Figures 5 and 6, respectively. It can be observed that the values of expansion are low and comparable with the concrete immersed in magnesium sulphate. Thus, concrete expansion may be attributed to the normal swelling of concrete. Kalousek and Benton [18]

proved experimentally that no correlation exists between the amount of ettringite precipitated and expansion, and it may be assumed that ettringite deposits in voids, and, therefore, exerts very little or no expansion.

The results illustrated in Table 8 and Figure 5 show the change in the length between the concrete immersed in magnesium sulphate and concrete stored in water. It is observable that the change in length in this case is much less relative to the change for concrete immersed in magnesium sulphate. The experimental consequences revealed that the concrete containing SCM grade 40 exhibits less swelling in the volume of the concrete sample. The reason for the FA,

RHA, and GGBS mixes is because it closes the voids to look better than the control mix OPC. This is due to the variation in the degree of fineness, which causes the expansion to exhibit different behaviour as the swelling of the concrete is dependent on the particle size and fineness degree of SCM. It is generally agreed that shrinkage increases with the increase in the cement content because this results in a large volume of hydrated cement paste, which is liable to shrink [10]. In addition, the changes in the length of concrete through air drying compared with the concrete immersed in magnesium sulphate exhibited the same behaviour, as shown in Figure 6.

6.5. Identify Concrete Deterioration due to Sulphate Attack. Throughout this study, it was possible to evaluate the effect of sulphate attack on concrete mixes by testing the changes in strength, height, and mass, in addition to observing the optical appearance of the test samples, as shown in Figure 7. It is acknowledged that the best indicator to evaluate the degradation of concrete is to measure the mass change and monitor the visual appearance of the test samples. The RHA, FA, and GGBS mixtures show the pozzolanic reaction which continues to increase and reduce the infiltration of SO_4^{+} ions within the concrete. A major impact to improve the durability properties of concrete effect in sulphate magnesium, and shows more accurate in all the mixes by using SCM.

7. Conclusion

The following conclusions can be drawn based on the results of the current study.

- (1) For the third cycle of exposure to sulphate attack, the concrete SCC contents 15FA, 10RHA, and 5GGBS appear to have higher strength values than those stored in water and air sample.
- (2) The highest value of mass loss is recorded for the control mixture, which has reduced the mass at the curing case at third cycle of exposures. In the drying test, the mass loss for all mixes is attributed to the formation of gypsum on the concrete surface in addition to the presence of SCM, which leads to more shrinkage and, consequently, a decrease in mass.
- (3) The change in length in curing concrete is much less relative to the change for concrete immersed in MS. In addition, the change in the length of concrete through air drying compared with the concrete immersed in MS exhibited the same behaviour because the values of expansion are low and comparable. Thus, concrete containing SCM, such as FA, RHA, and GGBS, exhibited expansion, which may be attributed to the normal swelling of concrete with consequent increase in length.
- (4) Generally, adding FA, RHA, and GGBS to SCC improves its resistance to sulphate attack. Increasing the SCM fineness will enhance its resistance, which is due to the increased pozzolanic activity.

Acknowledgments

The authors wish to acknowledge the support provided by the Science Fund (13-02-03-3092) entitled “Exploring the Potential of Malaysian Palm Oil Fuel Ash in Developing Durable Self-Compacting Concrete” and also the support from the University of Malaya.

References

- [1] M. H. Shehata, G. Adhikari, and S. Radomski, “Long-term durability of blended cement against sulfate attack,” *ACI Materials Journal*, vol. 105, no. 6, pp. 594–602, 2008.
- [2] T. H. Wee, A. K. Suryavanshi, S. F. Wong, and A. K. M. Anisur Rahman, “Sulfate resistance of concrete containing mineral admixtures,” *ACI Structural Journal*, vol. 97, no. 5, pp. 536–549, 2000.
- [3] FAO, *World Paddy Production for, Food and Agriculture Organization of the United Nations*, 2008.
- [4] S. Chandrasekhar, K. G. Satyanarayana, P. N. Pramada, P. Raghavan, and T. N. Gupta, “Processing, properties and applications of reactive silica from rice husk—an overview,” *Journal of Materials Science*, vol. 38, no. 15, pp. 3159–3168, 2003.
- [5] D. V. Reddy and B. S. Marcelina, “Marine durability characteristics of rice husk ash-modified reinforced concrete,” in *Proceedings of the 4th LACCET International Latin American and Caribbean Conference for Engineering and Technology*, p. 134, San Juan, Puerto Rico, USA, 2006.
- [6] M.-H. Zhang and V. M. Malhotra, “High-performance concrete incorporating rice husk ash as a supplementary cementing material,” *ACI Materials Journal*, vol. 93, no. 6, pp. 629–636, 1996.
- [7] D. Talend, *The Best-Kept Secret to High-Performance Concrete*, The Aberdeen Group, Boston, Mass, USA, 1997.
- [8] H. Y. Wang and K. C. Tsai, “Engineering properties of lightweight aggregate concrete made from dredged silt,” *Cement and Concrete Composites*, vol. 28, no. 5, pp. 481–485, 2006.
- [9] W. E. Ellis Jr., “For durable concrete, fly ash does not “replace” cement,” *Concrete International*, vol. 14, no. 7, pp. 47–51, 1992.
- [10] A. M. Neville, *Properties of Concrete*, England Longman, 4th edition, 1995.
- [11] ASTM, *Specification for Ground Granulated Plats-Furnace Slag for Use in Concrete and Mortars*, Book of ASTM Standards: Concrete and Aggregates, American Society for Testing and Materials, Philadelphia, Pa, USA, 2006.
- [12] C. S. Prasad, K. N. Maiti, and R. Venugopal, “Effect of substitution of quartz by rice husk ash and silica fume on the properties of whiteware compositions,” *Ceramics International*, vol. 29, no. 8, pp. 907–914, 2003.
- [13] H. Okamura and K. Ozawa ; “Mix design for self-compacting concrete,” *Concrete Library of JSCE*, no. 25, pp. 107–120, 1995.
- [14] G. A. Habeeb, H. B. Mahmud, and N. B. A. A. Hamid, “Assessment of deterioration in RHA-concrete due to magnesium sulphate attack,” *International Journal of Minerals, Metallurgy and Materials*, vol. 17, no. 6, pp. 691–696, 2010.
- [15] E. E. Hekal, E. Kishar, and H. Mostafa, “Magnesium sulfate attack on hardened blended cement pastes under different circumstances,” *Cement and Concrete Research*, vol. 32, no. 9, pp. 1421–1427, 2002.
- [16] M. Polivka and E. H. Brown, “Influence of various factors on sulfate resistance of concrete containing pozzolans,” *Proceedings—American Society for Testing Materials*, vol. 58, 1995.

- [17] D. Cusson and T. Hoogeveen, "Internal curing of high-performance concrete with pre-soaked fine lightweight aggregate for prevention of autogenous shrinkage cracking," *Cement and Concrete Research*, vol. 38, no. 6, pp. 757–765, 2008.
- [18] G. L. Kalousek and E. J. Benton, "Mechanism of seawater attack non cement paste," *Journal of American Concrete Institute*, vol. 67, no. 2, pp. 187–192, 1970.

Research Article

Electromechanical Characterization and Locomotion Control of IPMC BioMicroRobot

Martin J.-D. Otis

Applied Sciences Department, REPARTI Center, University of Quebec at Chicoutimi, Chicoutimi, QC, Canada G7H 2B1

Correspondence should be addressed to Martin J.-D. Otis; martin_otis@uqac.ca

Received 22 June 2013; Accepted 6 September 2013

Academic Editor: Kean Aw

Copyright © 2013 Martin J.-D. Otis. This is an open access article distributed under the Creative Commons Attribution License, which permits unrestricted use, distribution, and reproduction in any medium, provided the original work is properly cited.

This paper presents the electromechanical characterization of Nafion-Pt microlegs for the development of an insect-like hexapod BioMicroRobot (BMR). BMR microlegs are built using quasi-cylindrical Nafion-Pt ionomeric polymer-metal composite (IPMC), which has 2.5 degrees of freedom. The specific manufacturing process using a laser excimer for one leg in three-dimensional configurations is discussed. Dynamic behavior and microleg characteristics have been measured in deionized water using a laser vibrometer. The use of the laser vibrometer shows the linear characteristics between the duty cycle of square wave input and displacement rate of the actuator at multiple frequencies. This linearity is used to design a servo-system in order to reproduce insect tripod walking. As well, BMR current consumption is an important parameter evaluated for each leg. Current passing throughout the IPMC membrane can result in water electrolysis. Four methods are explained for avoiding electrolysis. The hardware test bench for measurements is presented. The purpose of this design is to control a BMR for biomedical goals such as implantation into a human body. Experimental results for the proposed propulsion system are conclusive for this type of bioinspired BMR.

1. Introduction

Microrobotic development in submillimeter size has really appeared with MEMS (Microelectromechanicals systems), using the MUMP process (Multiuser MEMS processes) and microfabrication process with excimer laser and LIGA (*Lithographie, Galvanoformung, and Abformung*) microfabrication technology [1]. Several designers and researchers in micro- and nanorobotics hope their robots will perform biomedical applications. Currently, these robots are in the early stages of development, and the objectives to be reached are spread out over several decades [2]. Micro- and nanorobotics are an important area covering the knowledge of science and applied science in robotics and microsystems. Natural law explains that the smaller a living organism is, the harder it is to kill it. BioMicroRobot is designed with this simple rule. If the control of micro- and nanotechnology is possible, it will be also possible to easily help or to kill living organisms (cancer, bacteria, etc.), as well as organic or inorganic substances (kidney stones).

Many microactuators are in development for insect-like microrobot legs, such as bimorph cantilever structures acting

as thermal actuators coupled or not with photonic band gap (PBG) materials, piezoelectric, electrostatic, magnetostrictive, shape memory alloy (SMA) and electroactive polymer (EAP) such as ionic polymers to name a few [3]. Some approaches are very interesting, but in biomedical applications, greater problems involve material biocompatibility. This constraint limits the use of some inert materials, largely used in human body like platinum, NiTi (Nitinol), some stainless steels, ceramic alumina, and some polymers. Materials from a biological source are interesting for microrobotic applications. This material should work overall in robot mission time without degradation, corrosion, or wear in the chemical environment (enzyme, pH, and under lymphocyte action). Of course, this material must not be toxic to the host system [4].

BioMicroRobot (BMR) is a microrobot used to help living organisms such as the human body in its metabolism and to resolve health problems like kidney stones. It can be used to understand, explore, change, or control biological systems. BMR with biosensors can replace medical instrumentation for monitoring and measuring physiological events such as an *in vivo* glucose biosensor with hydrogel.

BMR propulsion needs specific studies considering its many constraints. In this order of size and magnitude, it is necessary to study the context of its use and the BMR environment (aqueous medium, its conductivity and velocity, ambient temperature, pressure, etc.). Manufacturing is also an important challenge because of three dimensional handling of independent microparts. With the power supply being limited, it is necessary to reduce current consumption while optimizing mechanical properties of the actuator (force and velocity).

This paper covers all IPMC actuator parameters to be optimized for use on a BMR. Based on the choice made for the design of the microleg, it will be possible to manufacture it. The first part of the paper presents the chemical and mechanical manufacturing process of the microleg, which is critical for good quality and electromechanical properties. A failure in the procedure and bad handling could damage actuators and decrease performance. Indeed, metal electrode distribution particles added at the membrane surface are very sensitive to the chemical conditions of treatment, impregnation, and reduction. Second, for reducing some disadvantaged electromechanicals properties, a detailed model is carried out. Lastly, this paper recommends a central pattern generator for locomotion control using the actuator model. Displacement rate according to pulse width modulation (PWM) duty cycle and the resonance frequency coupled with a fluid according to the length is presented. This relationship will be very important for the design of a bioinspired servosystem in order to control the BMR like an insect in two- or three-dimensional environments.

1.1. Previous Work. Microrobot projects coming from Shuxiang Guo's laboratory are particularly advanced in designing microrobot with IPMC actuator. Recently, they study the position accuracy using 8 legged-locomotion using an IPMC model for one motion direction (using two electrodes on each surface) [5]. Also, other studies relates IPMC position control [6, 7] and in-pipe microrobot [8]. However, these microrobots are designed in order to move along a plane and to float in suspension without maneuverability in three-dimension.

This paper proposes a BMR similar to an insect with six microlegs. In order to move the body in a three-dimensional environment, each leg has to move in at least three axes (three degrees of freedom or 3 DOF). Since the robot is limited in size, power consumption, and manufacturing complexity, this paper suggests to design a leg which has one axis of movement coupled with the others two. Therefore, this configuration is considered as a minimum, which correspond to 2.5 degrees of freedom motion. This configuration allows driving the BMR as an insect tripod. However, with a lower DOF, the use of the *push-slip* method is also a design option such as piezoceramic actuation on a plane surface [9], but this propulsion reduces the application to a rigid surface. Higher DOF is better when the propulsion surface is deformed and many obstacles are present. To avoid obstacles, microlegs must leave the surface, which explained the need for 2.5 DOF per microleg.

Moreover, the actuator must have sufficient dimensions to support a microrobot of millimeter-length size. Along

these lines, previous paper was devoted to the manufacturing process of tubular and fiber IPMC [10, 11]. A clear explanation on the manufacturing process of the four electrode microlegs using a laser is provided to allow actuation with several degrees of freedom. Starting with some samples, it will be possible to measure the electromechanical characteristics quantitatively.

1.2. BioMicroRobot Geometry and Design. The BMR micro-actuator consists of six (6) quasi-cylindrical Nafion-Pt ion-omeric polymer-metal composites (IPMC), and one tubular IPMC connected to a micropump enabling thrust vector control. IPMC has three (3) components: an ion-exchange membrane (IEM) like the perfluorosulfonic acid polymer, some cations, and at least two electrodes. Using a 6-legged locomotion is generally used to improve the stability of the microrobot during a displacement on a flat surface such as the cockroach tripod walking. However, some applications where more complex maneuvers in fluid such as obstacle avoidance and trajectory following require navigation in three dimensions enabling swimming capabilities. In this situation, it would be possible to use a thrust vector controlled by a tubular IPMC. First, a micropump installed on the back of the robot pushes the ambient fluid in a tubular IPMC. The curved tube directs the fluid jet generating a thrust (force) vector located at the IPMC anchored point which push microrobot following Newton's laws of motion. The use of a micropump is however necessary with the tube, which still represents a significant technological challenge. The characterization of this system (micropump, IPMC, and tubular fluid density) is not a part of this paper.

IEM consists of a cross-linked ionomer matrix with relatively uniform distribution of ion-active sites (cluster network) throughout the structure. The effects of different types of cations, electrode-membrane interfacial areas, and surface electrode resistance on performance are well known [12–14].

Each IPMC component has an effect on the electromechanical characteristics. IPMC works on two principles. First, the electroosmosis in the ionomer moves the cation and water to the cathode side by the electrostatic force when an electric field is applied. The osmotic pressure inside the polymer creates a bending that produces a corresponding displacement [15]. The second principle is the pumping effect of the cations. It would be the dominant contribution in the case of hydrophobic cations. It seems that the superposition effect works with different cation types, such as the ammonium form and alkali cations [16].

Our BMR design is presented in Figure 1. A vision system is also currently being evaluated, which is designed like an echosounder. Since the leg design should move in 2.5 degrees of freedom, the microleg tip movement could be represented by Figure 2. The motion of the microleg is composed of two gait phases: swing phase (recovery phase) and stance phase (support the weight body). The anterior transition point (transition from swing to stance) is called the anterior extreme position (AEP), and the posterior transition point is called the posterior extreme position (PEP).

This electroactive polymer or IPMC actuator has many advantages over all others; it has a quick response to low

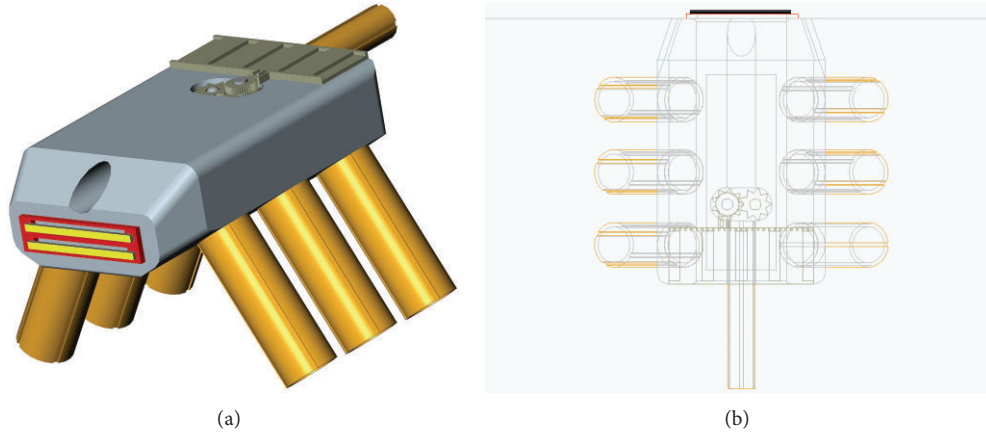


FIGURE 1: BioMicroRobot geometry using IPMC micropump and six IPMC microlegs.

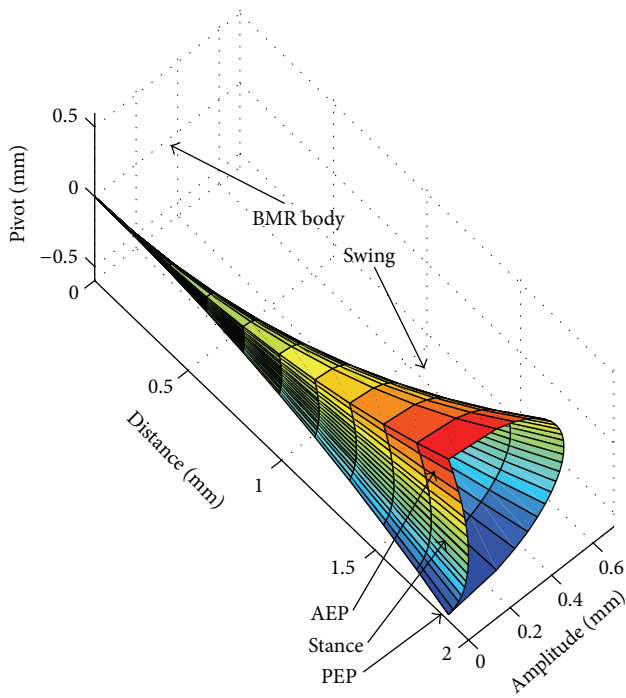


FIGURE 2: Ideal microleg tip movement in 2.5 DOF.

voltage, bends more than 100 K times, generates distributive deformation, has a low weight, can be downsized easily, and can be used in water [17]. It seems to be safe in the human body [18] if no water electrolysis is produced. It can be driven at low voltage, less than 2 volts. However, as described in Figure 3, we have measured a step transient response showing high instantaneous current consumption with Nafion-Pt and Lithium counter ion.

Water electrolysis and current consumption are two major IPMC disadvantages for microrobot applications. In part of this paper, we will demonstrate how to avoid electrolysis of Nafion-Pt IPMC with Li^+ . Platinum dissolution is also an inevitable consequence of metal use in the stimulation regime. Dissolved platinum is toxic in living organisms [19].

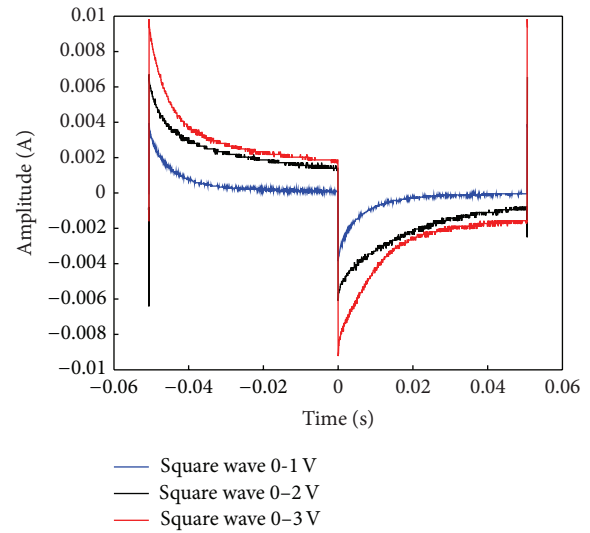


FIGURE 3: Current response to different squares waves voltage input.

2. Materials and Methods

In previous studies, we have used the tubular Perma Pure Inc. TT-030 Nafion [10] for the micropump design. Actuator movement is adjusted to orient the fluid direction. For a microleg design, the tubular shape generates too small displacement for this application. In another application, Nafion tube will be used to create an implantable inductive coil for BMR telemetry and power supply. In fact, the use of Nafion N-117 (DuPont) fiber (quasi-cylindrical cross section) is better for the displacement rate and current consumption [11]. The size of this new microactuator is about $200 \mu\text{m} \times 200 \mu\text{m}$. Its length L is about $4,000 \mu\text{m}$ for the actuator characterization. Expected final microleg length on the BMR body is about $1,500 \mu\text{m}$.

2.1. IPMC Manufacturing. This method can be done using any ionomer membrane. Ion exchange membrane (IEM) is a hydrophilic ionic polymer, which swells up about 10% in water at room temperature. The membrane N-117 is cut into

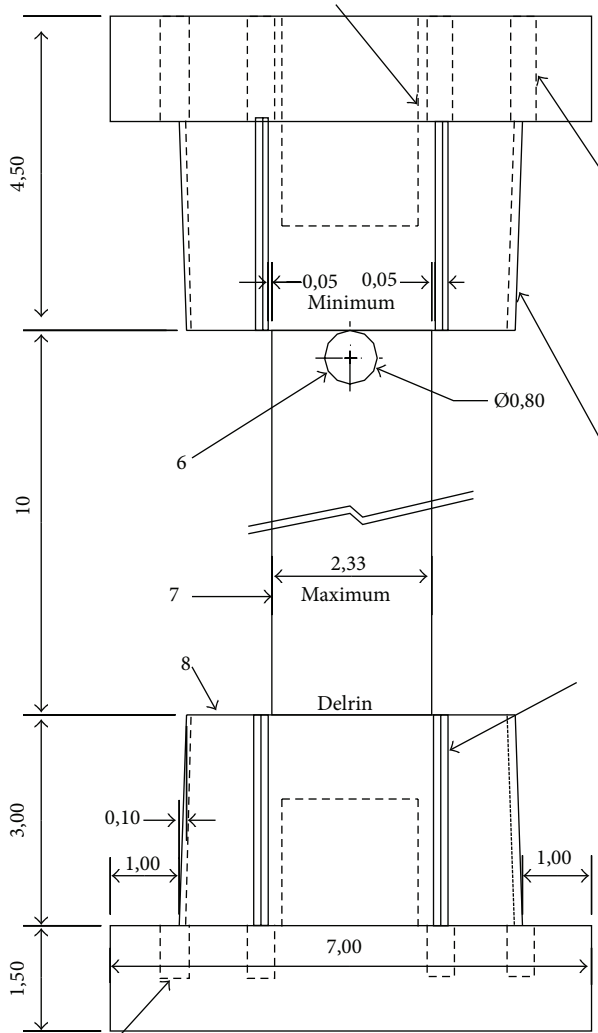


FIGURE 4: Six fiber holders for the manufacturing process.

fibers of $187\ \mu\text{m}$ with a sliding microtome LEICA SM 2500. The speed of microtome blade is set to $0.5\ \text{mm/second}$ with an angle of attack set at about -2 degrees. Next, the six fibers are attached to a homemade support as shown in Figure 4.

The ionomer is cleaned in an ultrasonic water bath and boiled in HCl and water for about 30 minutes each. The ionomer is chemically plated with platinum using the impregnation and reduction (IR) process [20] as shown in Figure 5. Ion exchange (absorption in Figure 5(a)) and ion reduction (Figure 5(b)) are repeated up to two times to make $3\ \mu\text{m}$ thick porous platinum layers (Figure 6). Li^+ cations are used on all IPMC to obtain faster responses.

2.2. Excimer Laser Process. The electrodes on the tube and fiber are cut into four sections using an excimer laser process. The laser beam removes the plated surface in order to form four sections around the IPMC. These four sections drive the IPMC in 2.5 degrees of freedom. Figure 7 shows the micropump propulsion using tubular IPMC while Figure 8 represents one microleg. Both Figures are resulting from the

laser process. This configuration around the IPMC should allow eight directions of motion labeled as S_1 to S_8 . This technical process is also used to build up the BMR body and induction coil for the power supply.

2.3. Hardware Test Bench. In order to obtain the dynamic behavior of microlegs under electrical solicitation, a scanning laser vibrometer is used to measure the tip (free end) speed of displacement as a function of both frequency and the electrical current induced. The effect of microleg length on the first vibration mode is also inspected in a fluid.

The beam formed by the actuator is clamped at one end and is acting freely in $18\ \text{M}\Omega$ deionized water at room temperature (Figure 9). The laser beam goes through an optical window and reaches the microleg perpendicular to its neutral plane. Refraction of light has not been taken into account in the related measurements.

The applied voltage is a periodic PWM signal programmed as an arbitrary waveform generator-like model HP33120A. The waveform consists of a 1024-point signal where half the points form a positive PWM and the other half a negative one. Instantaneous speed was measured at the tip of the actuator and stored for all duty cycles used in the PWM signals of the waveform. The waveform has a 3 V peak-to-peak and is applied at 10 and 20 Hz.

The current is measured using two types of instruments. The first type is a current probe that measures the electromagnetic field around the cable (Tektronix P6042). The second type is a transimpedance amplifier (with gain set at 100 using the resistor) placed in serial with H-Bridge MOSFET and IPMC. The isolation circuit using H-bridge MOSFET for the stimulus circuit is placed to drive opposite electrodes on IPMC microlegs. This circuit is used with the microcontroller parallel output port to drive all six microlegs and one vector control propulsion (this represents a total of 28 electrodes).

These measurements were done far away from the first resonance of the mechanical system: a modal analysis of the microleg using a randomly applied voltage and scanning capability of the vibrometer revealed an initial natural frequency of 180 Hz. This frequency takes into account the coupling between the fluid and the structure.

3. Microleg Model

Our previous paper demonstrates three-dimensional microleg movements with mathematical equations and simulation for the actual electrode configuration [10, 11]. Two voltage amplitudes were simulated. This section presents all results for the frequency response and includes theoretical explanations and an analysis of each result.

3.1. Analog Electrical Stimulus. Microlegs will be driven by a voltage-controlled CMOS technology. It is important to know these stimulation effects on the current consumption at any frequency.

The current transient step response shows a major current peak that decreases rapidly (Figure 3). A negative peak is also produced when the square wave stimulus return to zero. This

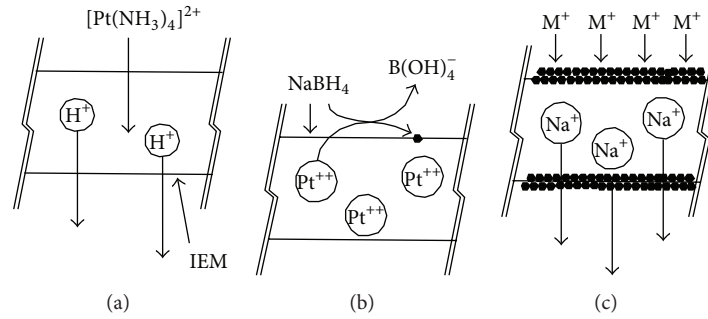


FIGURE 5: Chemical process of Nafion plating with platinum [20].

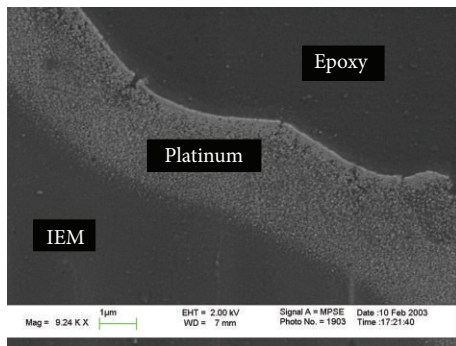


FIGURE 6: IPMC cross section.

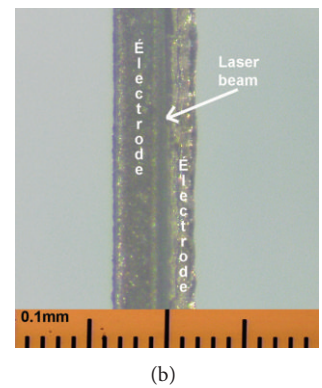
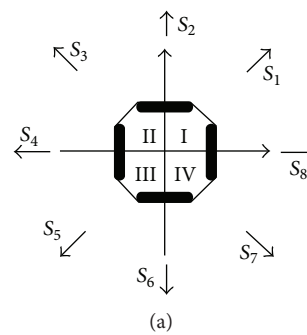


FIGURE 8: Square section of the microleg.

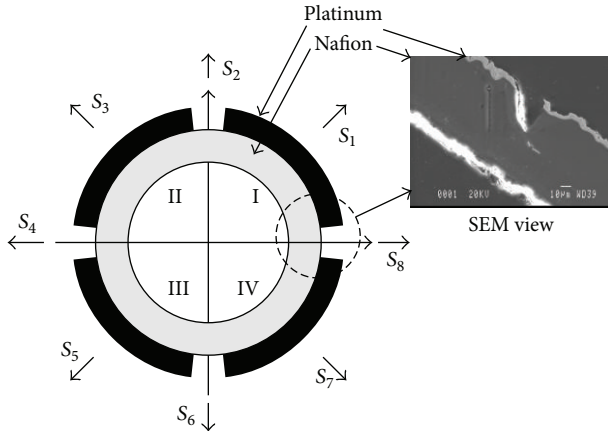


FIGURE 7: Tubular IPMC for the micropump propulsion.

phenomenon is explained by a serial resistance-capacitance ($2R_s + C_{dl}$) network introduced via the electrode-electrolyte interface (Figure 10).

Capacitance is due to double-layer capacitance C_{dl} . If the voltage is increased, C_{dl} increases until the electron transfer occurs at the electrode/solution interface. The continuous current remains in steady state, which shows a nonlinear resistive element R_F through the IPMC parallel to RC network [21]. This reaction was analyzed previously for different IPMC and cations types [22]. Normally, electroneutrality is maintained across the interphase, but it may be leaky, allowing some faradic current to flow across it, explained

by faradic resistance R_F . R_F may behave as simple ohmic resistance, but it also can be a hyperbolic or an exponential function of potential, depending on the range of overpotential considered. C_{dl} also is a complex function of potential, although it may not vary as much as R_F [23].

Analysis of microleg electromechanical characteristics does not need to include an analysis of Warburg impedance and absorbing pseudocapacitance due to the limitation of mass transport by the diffusion and transfer process of charge. However, it is important to note that Warburg impedance adds a constant phase of -90° between current and voltage, which may influence transient or frequency analysis as seen in Figure 11(b). Only C_{dl} is treated as pure capacitance, in the physical sense.

Electrode surface resistance, R_{SS} , can be represented and explained by low conductivity, insufficient electrode thickness, microscopic cracks and the heterogeneous deposition of metal particles. The cyclic deformations in traction and contraction during cyclic movement of the IPMC can cause fatigue and an increase in this resistance [24, 25]. The network $R_F // (2R_s + C_{dl})$ is an approximation of the proposed model.

In steady state, two regions have been defined for the microleg: the linear zone below the decomposition voltage (sum of metal overpotential used as the electrodes and standard equilibrium potential or standard electrode potential) and nonlinear exponential zone above decomposition voltage (Figure 12).

The frequency response shows interesting particularity. Measurements are taken using the sinusoid 2 V peak-to-peak.

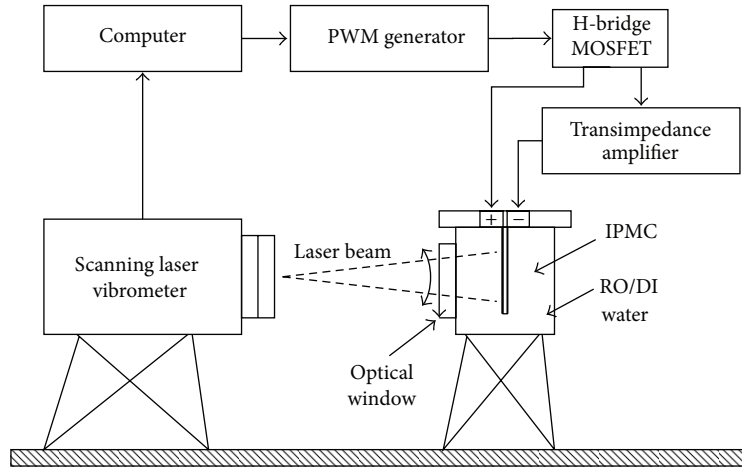


FIGURE 9: Experimental setup for microleg speed measurement.

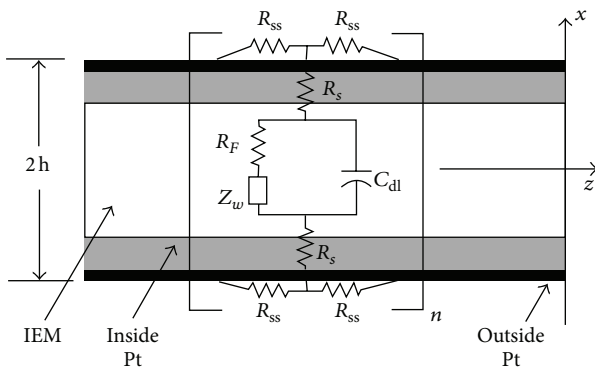


FIGURE 10: IPMC electrical model [24].

The current amplitude response has a gain of -10 dB/decade between 5 and 100 Hz and cut-off frequency near 45 Hz. As well, linear characteristics are associated with the phase frequency response.

This characteristic shows that current is out of phase from voltages between -100° and -180° . It can be explained by the presence of absorbing pseudocapacitance and Warburg impedance.

3.2. Mechanical Displacement Analysis with PWM. Analysis carried out until now does not make it possible to control the IPMC bending angle using CMOS technology. RISC microcontroller architecture does not support analog output at the 8-bit parallel port [26]. Adding a digital-to-analog converter (D/A) is a cumbersome solution for MEMS and/or microproduction. Although the IPMC microleg can be modeled using a $R//RC$ network, the use of PWM modulation can adjust the quadratic mean of the electric tension V_{RMS} . Next, the bending angle can be controlled if a relationship exists between the IPMC bending angle and PWM duty cycle.

However, the first step is to check whether a certain dependence or correlation exists between the duration of PWM impulse and microleg displacement. The scanning

laser vibrometer cannot directly measure displacement, because it can only analyze dynamic structure. Therefore, it is necessary to study the dynamic behavior in a cantilevered beam configuration, that is, microleg tip displacement rate function of the PWM duty cycle. The waveform generator provided with scanning laser vibrometer requires programming the desired signal.

For the experiments, the IPMC is supplied periodically on each one of its electrodes. This periodic signal vibrates the structure within two degrees of freedom. This implies the periodic generation of the standardized signal. Parameter adjustment (frequency of the signal and the voltage amplitude) on the standardized signal makes it possible to obtain excitation signals used for the experiments. The signal is adjusted with a value of a 6-volt peak-to-peak for two frequencies: 10 and 20 Hz.

Figure 13 shows the tip microleg displacement rate in a cantilevered beam configuration for 10 Hz and 20 Hz for the odd PWM duty cycle. Figure 14 shows a mean maximum speed for each PWM duty cycle over the 30 measurements taken from data as found in Figure 13. Experimental results may be expressed as linear characteristics. The next analysis shows the degree of correlation between the mean maximum speed movement and PWM duty cycle.

The correlation coefficient r calculation provides an estimate of the correlation degree between two random variables of even population. The value obtained for r must be checked to ensure that it does not differ significantly from 0, which probably indicates a linear absence of the correlation between the variables observed. A significance threshold of 0.05 and a population of ten (10) samples for the mean maximum are used for the analysis. The variation of vibration function of frequency is distributed according to Student Law (bilateral case) with 8 degrees of freedom. Since the value of r^2 is high (0.982 and 0.986), as shown in Figure 14, the straight line adjustment at the experimental points is a good quality. It is obvious that this study cannot show cause-to-effect between the two variables. However, predictable actuator mechanical and physical behaviors make it possible to validate that there is a cause-to-effect between

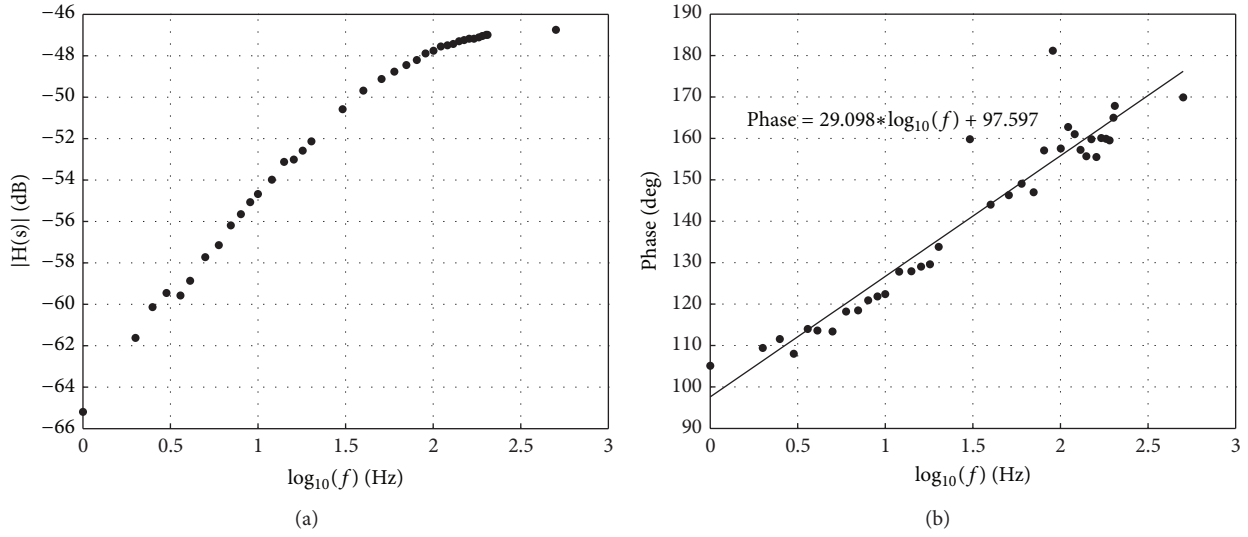


FIGURE 11: Current amplitude (a) and phase (b) response ratio of voltage amplitude function of frequency.

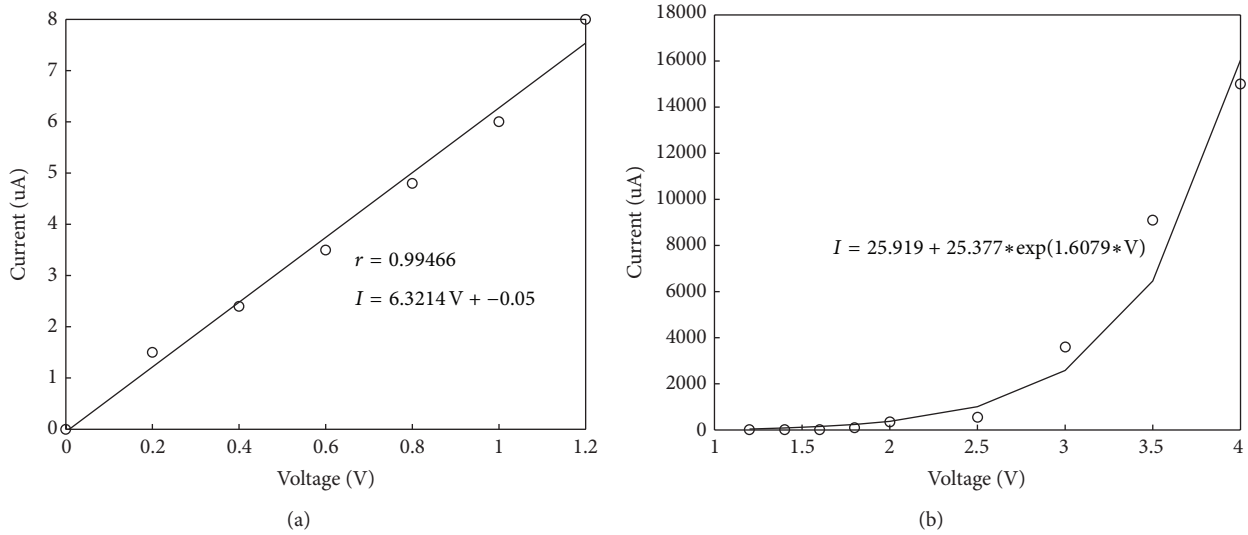


FIGURE 12: Steady state current function of voltage in (a) linear and (b) nonlinear regions.

the two independent variables: the variations of one variable involve the variations of the other without an unspecified attribution of an external common cause variation.

3.3. *Frequency Analysis Using FFT.* Starting from these results, it is possible to investigate more IPMC properties in the frequency domain. A structure of this type has particular modes of resonance that can be used in the propulsion of the robot as a strategy for reaching optimal motion. It was shown that IPMC dimensions vary its natural frequency: the natural frequency decreases when its length increases in a similar way to a cantilever beam [27].

The distributed systems have an infinite number of degrees of freedom and natural frequencies. Each natural frequency has a single mode, which is known to be like a normal function. A transitory vibration forced or in a steady operation will generally excite several or all the frequencies

and modes in combination. The clear response in a point can be expressed in their terms according to the superposition principle. The first mode is that associated with the weakest frequency [28]. The use of the first vibration mode will be probably advantageous for moving the robot at its optimal speed in terms of current consumption versus velocity. Thus, it is necessary to theoretically and experimentally analyze the IPMC first modes in the cantilever beam configuration.

In the case of the IPMC microleg, free end tip mass is negligible. Next, the resolution of theoretical equation provides all the proper frequency f_n using [29]

$$f_n = \frac{1}{2\pi} \frac{k_n^2}{L^2} \sqrt{\frac{EI}{\rho S}}, \quad S = 2lh, \quad (1)$$

where L is the IPMC length, lh product is the IPMC cross section (0.2 mm × 0.2 mm), I is the inertia, and E the Young

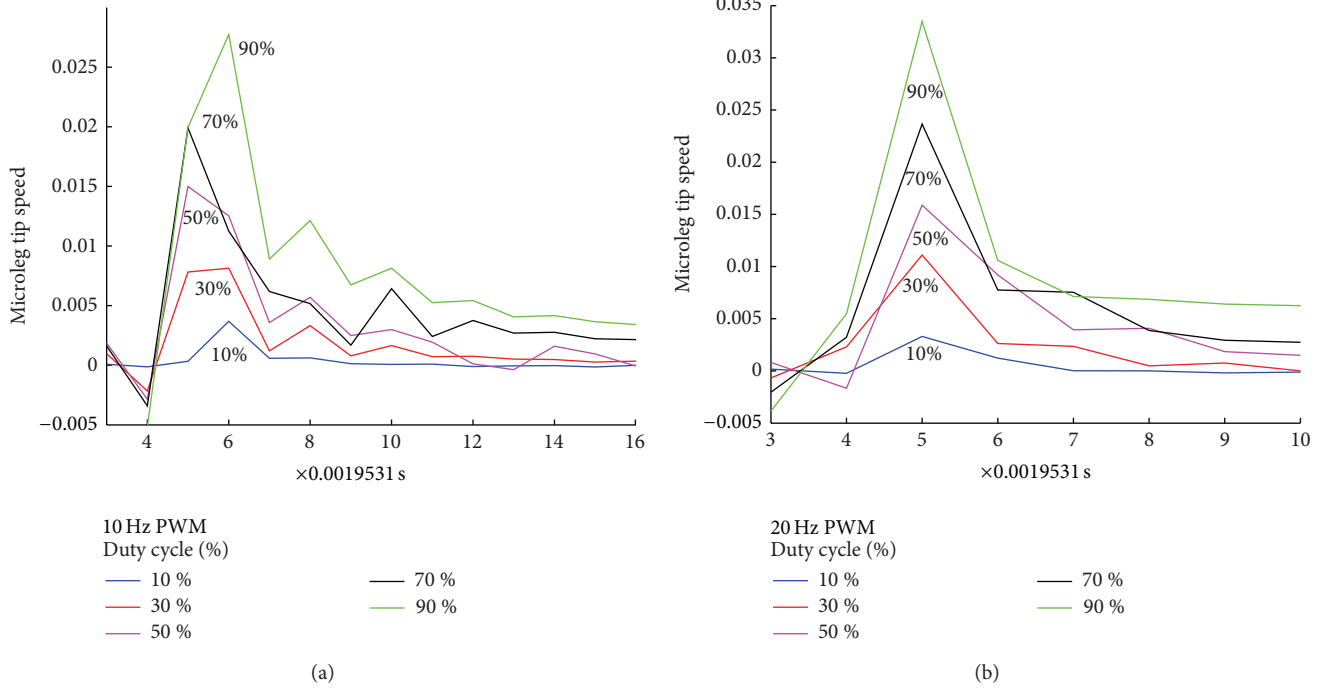


FIGURE 13: Tip microleg displacement rate in function of multiple PWM duty cycle at PWM period of (a) 10 Hz and (b) 20 Hz.

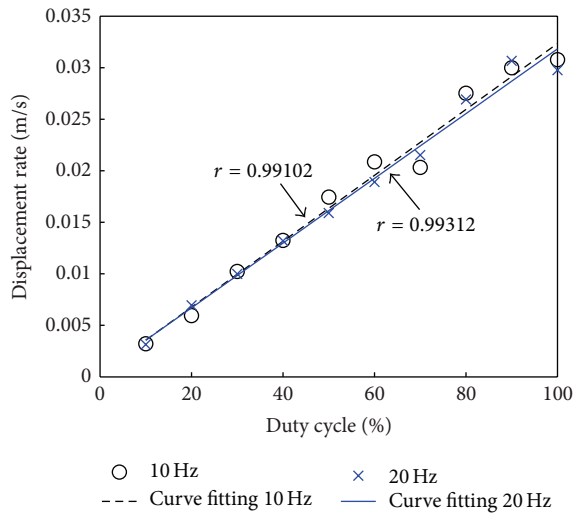


FIGURE 14: Mean of maximum tip speed as a function of PWM duty cycle.

modulus. k_n comes from the resolution of characteristic equation:

$$1 + \cos(k_n) \cosh(k_n) = 0. \quad (2)$$

However, this equation is not valid within the water environment. It is necessary to consider the behavior of a fluid-structure coupled system. In general, it should be checked whether the fluid is incompressible. In this case, the effect of fluid is then purely inertial. Using the representation of added mass makes, it possible to find a simple formula to

evaluate the natural frequency of the coupled system. When the structure vibrates in water, it induces water acceleration, producing an additional force on the structure, in addition to the force of trail fluidic-dynamics. This added force can be suitably modeled as the product of hypothetical water mass and structure acceleration. This implies that the structure in water vibrates at a natural frequency weaker than the frequency in a vacuum. By replacing inertial I of a circle of radius a and its surface S in (1) of the eigen frequencies f_n , the result is given by

$$I = \frac{\pi(2a)^4}{64} = \frac{\pi(a)^4}{4},$$

$$S = \pi a^2, \quad (3)$$

$$f_n = \frac{1}{2\pi} \frac{ak_n^2}{2L^2} \sqrt{\frac{E}{(\rho_c + C_m \rho_w)}}.$$

The equation describing a vibrating beam in water should comprise both the structure density of the beam described in (1) and that of water, which corresponds to a coupled system in density. The coefficient of added mass C_m defined as the ratio of the added mass to that of water moved by the cylinder makes it possible to couple the structure with water according to

$$f_n = \frac{1}{2\pi} \frac{ak_n^2}{2L^2} \sqrt{\frac{E}{(\rho_c + C_m \rho_w)}}. \quad (4)$$

A simulation of (3) and (4) is shown in Figure 15. To prove this theory, modal analysis was carried out with the

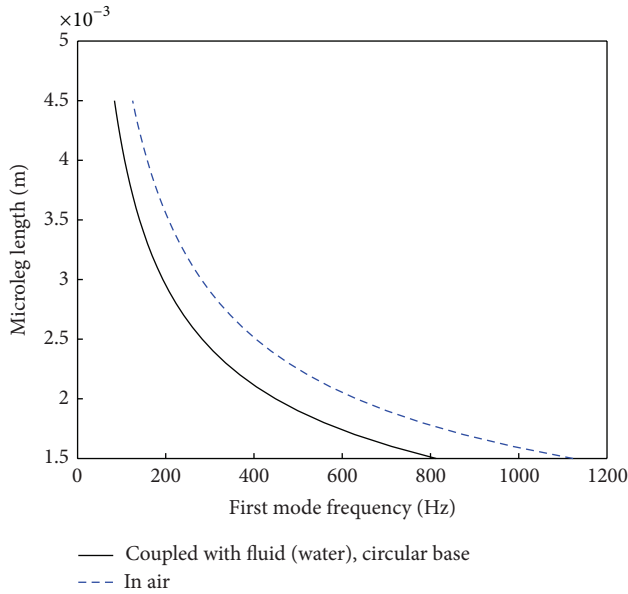


FIGURE 15: Simulation of the microlegs first mode frequency functions of its length.

scanning laser vibrometer using a pseudorandom excitation voltage (Gaussian white noise) of 6 V peak-to-peak. This analysis makes it possible to find the first mode vibrating frequency F_{r1} at about 180 Hz for a 4-millimeter microleg length (Figure 16). This frequency takes into account the coupling between heavy fluid (deionized water) and the structure. A digital simulation is used to find a frequency close to that found with the laser. Moreover, it is interesting to compare the tension/current cut-off frequency (about 45 Hz from Figure 11(a)) with the maximum frequency F_{MAX} at about 50 Hz. Note that frequency response fluctuates according to the applied voltage and according to resistance R_F and capacitance C_{dl} values.

4. Water Electrolysis

Many other IEM membranes can be used for this experiment, such as Flemion or Aciplex. Flemion-Au IPMC, with its dendrite inside ionomer, is known to have a higher ion exchange capacity, higher surface electrical conductivity, higher hydration capacity, and higher longitudinal rigidity than Nafion-Pt. These conclusions provide Flemion-Au with a better curvature angle for the same applied voltage without relaxation [30]. Gold can be also envisaged given its advantages: stable in acid, ductile, good electrical conductor, and less reactive in electrochemical reactions [31, 32]. Gold has also an overpotential higher than Pt. It allows using higher voltages to produce bending curvature without water electrolysis.

This section presents different ways to avoid water electrolysis. Currently, cation type and electrode metal have demonstrated some useful characteristics for avoiding back-relaxation when stimulus is applied and for avoiding water electrolysis. First, an overview of cation and electrode characteristics is presented. Second, a new way to avoid electrolysis

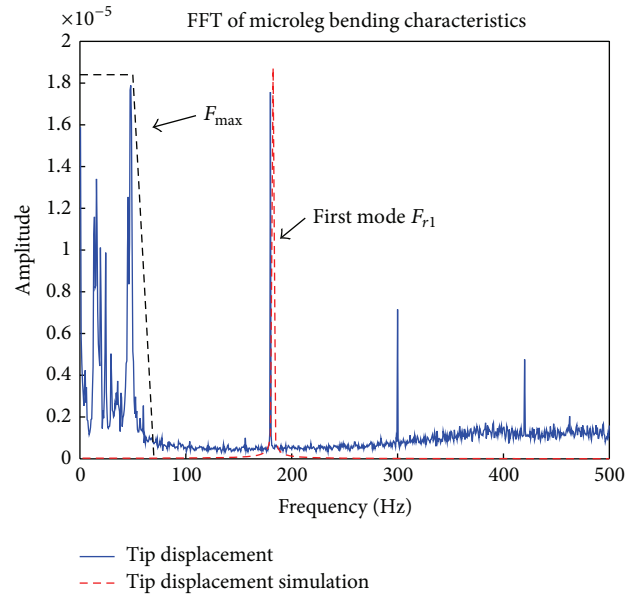


FIGURE 16: Modal analysis with laser vibrometer in frequency with FFT.

is introduced with signal waveform and frequency applied as the stimulus.

4.1. Cation Type. Cations can be divided into three classes: *A*, *B*, and *C*. These classes are categorized by water ionic conductivity and water state inside IEM. The *A* class contains small hydrophilic alkali and some alkaline-earth metal (Li^+ , Cu^{2+} , Na^+ , K^+ , Rb^+ , and Cs^+). The *B* class is formed by hydrophobic alkyl ammonium ions ($(\text{CH}_3)_4\text{N}^+$, $(\text{C}_2\text{H}_5)_4\text{N}^+$, $\text{NH}_{4-m}(\text{CH}_3)_m^+$, and $\text{NH}_{4-m}(\text{C}_2\text{H}_5)_m^+$). Lastly, class *C* includes the large hydrophobic cations, such as TBA (tetrabutylammonium⁺) and TPrA (tetrapropylammonium) [33].

Water displacement volume inside polymers causes contractions and dilations, which involves asymmetrical pressure distribution. Thus, internal stresses produce temporary polymer deformation. For small cations, like Li^+ , the displacement response is fast. However, if tension is maintained, the polymer will not keep its shape with a Nafion-Pt composite [22]. From another perspective, for bulkier cations, like tetra-*n*-butylammonium⁺ (TBA), the response is slower, but there will be a little relaxing. The relaxation time depends on the water leakage in the polymer interstices.

Relaxation probably occurs since the cations transport more water molecules than there should be in an equilibrium state. Relaxation will finish when equilibrium has been reached between the osmotic water pressure (dilution of the ions types) induced by electrical voltage, interfacial polymer-solvent, and polymer internal elastic energy (limitation of polymer chain elongation) [34]. No further relaxation is observed with TBA cation type. It can be caused by the possibility that the cations block the channels and prevent water leakage or by the possibility that the concentration of cations requires more water than it moved. No relaxation

occurs with Flemion-Au IPMC for all cation types. Instead, the displacement rate drops without moving back [22].

If ammonium size increases, IPMC displacement rate will go down, because of the slower molecule mobility inside the ionomer. However, the IPMC curving angle will be more pronounced, and relaxation by water leakage will decrease gradually. Moreover, ammonium's slower mobility eliminates electrochemical reactions like water electrolysis [35].

4.2. Electrode Characteristics. Electrode polarization, by electrical current, should alter half-cell potential. Half-cell variation (difference between observed half-cell potential and equilibrium zero current half-cell potential) is known as overpotential. The element chosen for electrode composition is directly associated with IPMC performance such as ductility and electrical conductivity. Electrodes must be also stable in electrochemical reactions like noble metals. Of course, overpotential should be very large for a higher decomposition potential. This section explains the effects of overpotential.

Electrodes made with noble metal, such as platinum and gold, have a behavior similar to perfectly polarizable electrodes. Both platinum and palladium have extremely small overpotentials for hydrogen evolution. Gold has a significantly larger overpotential. As well, gold does not appreciably absorb hydrogen, and this factor together with its larger overpotential for hydrogen evolution makes gold the metal of choice [21]. Such a relatively inert electrode is difficult to oxidize and dissolve. The best reaction for IPMC is characterized by a displacement current (no actual charge crosses the electrode-electrolyte interface) and the electrode behaves as though it were a capacitor. In this case, the majority of the overpotential is a result of concentration overpotential (ion concentration variation at the interface) [36].

Frequency and waveform have a direct influence on ion mobility inside IEM. The next section explains frequency and waveform influence on the displacement current at the interface to approach IPMC behavior as a capacitor without a resistive element.

4.3. Frequency and Waveform. Visual observations of microleg displacement show that the movement is greater in the nonlinear region. This result is not interesting for many biomedical applications. However, it is possible to drive the microleg with a charge-balanced waveform.

Control of the charge density and charge balance are essential for avoiding electrolysis and to provide a chemically reversible reaction (or safe stimulation). Waveforms can be symmetrical or asymmetrical. Symmetrical refers to biphasic stimuli in which the magnitude of the current density in the first pulse of the biphasic pair is the same as in the second pulse. The use of biphasic stimulus waveforms with zero net charge flow does not guarantee that toxic electrochemical reaction products will not be produced [37].

Considering the IPMC electrical model, a minimum frequency is necessary for eliminating water electrolysis. The electrochemical technique of cyclic voltammetry can delineate an operational potential window between hydrogen and oxygen evolution. This technique is applied to find minimum

frequency of symmetrical stimuli because water electrolysis decreases thermodynamic efficiency and consumes power.

Figure 17 shows three hysteresis curves for the frequency 10, 30, and 180 Hz. Signal amplitude applied to system is 5 V peak-to-peak in order to produce water electrolysis. To read current amplitude, divide ΔY , on this figure, by 100, which is the transimpedance amplifier gain. Water electrolysis is shown by concave form at two hysteresis extremity. It is clear that increasing frequency decreases power consumption and eliminates water electrolysis.

A study could be carried out to characterize the mechanical reactions during stimulation with a current source instead of a voltage source. The use of a current source would make it possible to control the quantity of charge flow injected by varying amplitude and/or the width of the pulse phase with any IPMC impedance. Maximum charge density being able to be injected is according to the surface of the electrodes.

5. Locomotion Model and Control

A very special design will be developed and explained to allow BMR to move in all directions within the constraints of the actuators and the eight-bit parallel port of the microcontroller [26]. In this vein, the first part of this section is devoted to the study of the dynamics of an insect gait. This study highlights the main parameters to be considered in order to operate the microleg. Among other things, the types of locomotion are covered. The type of locomotion is important because it depends on the speed of the insect and hardware constraints of the microcontroller. The analysis of the movement of the leg and the movement of an insect with six legs, like ants, leads the design of the control system. It will also be necessary to understand the functioning of the physiognomic locomotion in the central nervous system for a robust adaptive algorithm.

5.1. Insect Locomotion. At this time, many works have studied the decentralized and central control systems involved in locomotion. The combination of behavioral and electrophysiological experimental data shows that locomotion is the result of both central and decentralized mechanisms [38]. This implied that each leg has an autonomous sensitive element controlled independently.

The RISC microcontroller architecture used in this application has only one eight-bit parallel port [26]. This strong internal constraint only lets us use the central control. In fact, decentralized locomotion control would require a 28-output bits on one parallel port (6 legs \times 4 electrodes per leg, plus the micropump using thrust vectoring control) from the microcontroller to drive each BMR leg independently without sensitive input and reflex. Next, this paper is based essentially on central systems. With this bus width, a simple neural network architecture called Walknet, a biologically inspired network for controlling six-legged walking, can be used from a cellular nonlinear approach [39, 40]. The central command developed here coordinates BMR movements with a higher stereotypy and less adaptivity. A feedback loop acts as a reflex to adjust the leg displacement. This reflex can move one leg to another position to avoid or to climb over an obstacle.

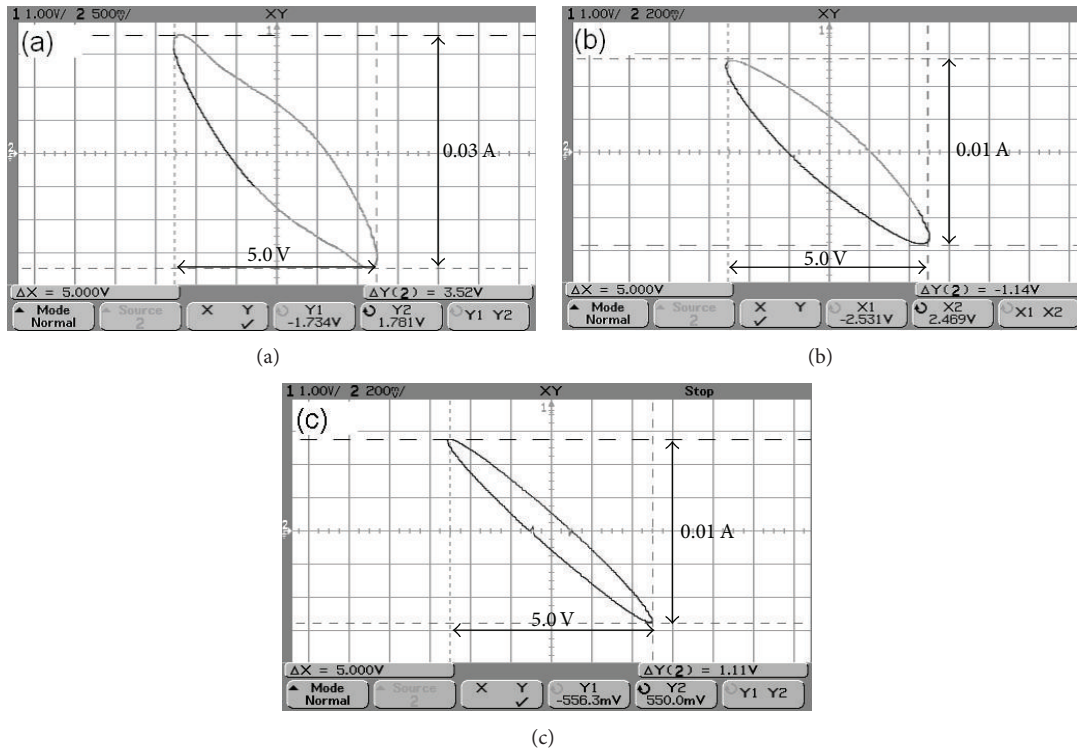


FIGURE 17: Hysteresis of current response for (a) 10 Hz, (b) 30 Hz, and (c) 180 Hz sinusoid voltage for the same voltage amplitude applied.

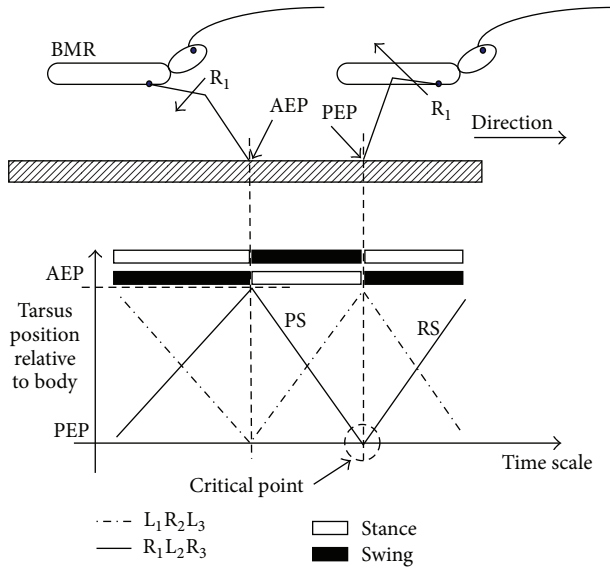


FIGURE 18: The cyclic movement of a leg and the tripod (fastest gait) walking stepping pattern.

5.2. Hexapod Insect Walking. The cyclic movement of a walking leg consists of two parts (shown in Figure 18), the power stroke (PS, also stance or support phase that propels the body) and the return stroke (RS, also swing or recovery phase).

The anterior transition point (transition from swing to stance) is called the anterior extreme position (AEP), and

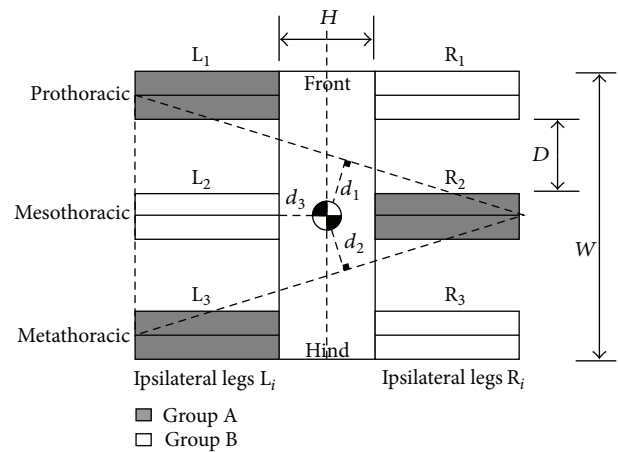


FIGURE 19: Top view of microrobot. Two legs groups (A, B) must be used. The tripod of support is represented by the dash triangle.

the posterior transition point is called the posterior extreme position (PEP). The most critical point to maintain the robot's stability is the transition from PS to RS [41]. Next, an interesting location for the feedback sensor could be used to detect PEP movement.

Two conditions must be met to maintain the robot's stability during all locomotion phases. The center of gravity of the body must lie within the triangle of support as shown in Figure 19. As well, three feet must always be on the ground simultaneously. The body is supported alternatively, for equal

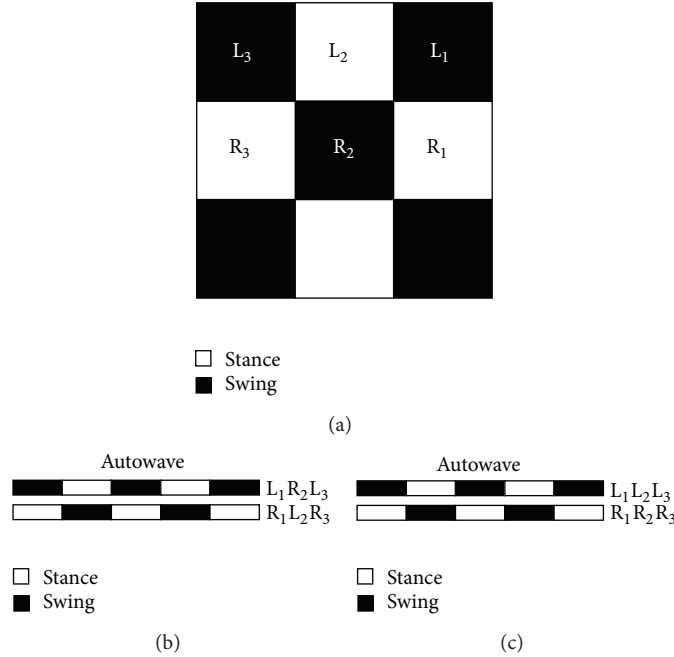


FIGURE 20: (a) Checkerboard Turing pattern corresponding to tripod gait locomotion. (b) Insect fast-gait pattern. (c) Insect swimming pattern.

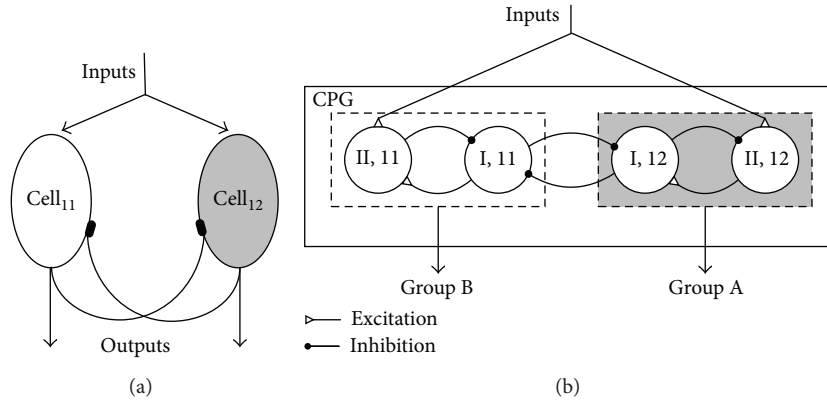


FIGURE 21: (a) Reciprocal inhibition network consisting of two similar neurons (or two populations of neurons). (b) CPG CNN design with reciprocal inhibition network.

periods of time, by one of the two groups of legs (tripod gait): A (L₁R₂L₃) or B (R₁L₂R₃).

The stability margin is defined as the shortest distance (d_1 , d_2 , and d_3) from the center of mass to the edge of the tripod of support. Many insects closely conform to this pattern when moving quite rapidly [42, 43]. Two main strategies are known to allow the insect to turn: increasing step frequency or step length of legs on one side of the body versus the other [44].

5.3. Central-Pattern Generator Paradigm. The central nervous system (CNS) must produce specific patterns of motor neuron impulses during coordinate locomotion or movement. The central hypothesis purports that rhythmic movements or basic motor programs in walking are driven by the central-pattern generator (CPG) located in the CNS. The

CPG includes subnetworks of command neurons (CNs) and local pattern generating neurons (LPGNs). The neurons of LPGN are called motoneurons (flexors and extensors neurons) [45, 46]. The impulse in nerve membrane is modeled using the nonlinear reaction-diffusion partial differential equation (RD-PDE), which can be represented by autowaves with cellular neural networks (CNN). Its capacity to generate plateau potentials or oscillations is a key issue for rhythm generation, but also for driving the transition among various types of locomotion like walking, running, and swimming [47].

Taking into consideration the biological aspects of locomotion, reaction-diffusion CNN (RD-CNN) is made up of two parts: one is devoted to generating autowaves (Figures 20(b) and 20(c)) and the other is responsible for specific

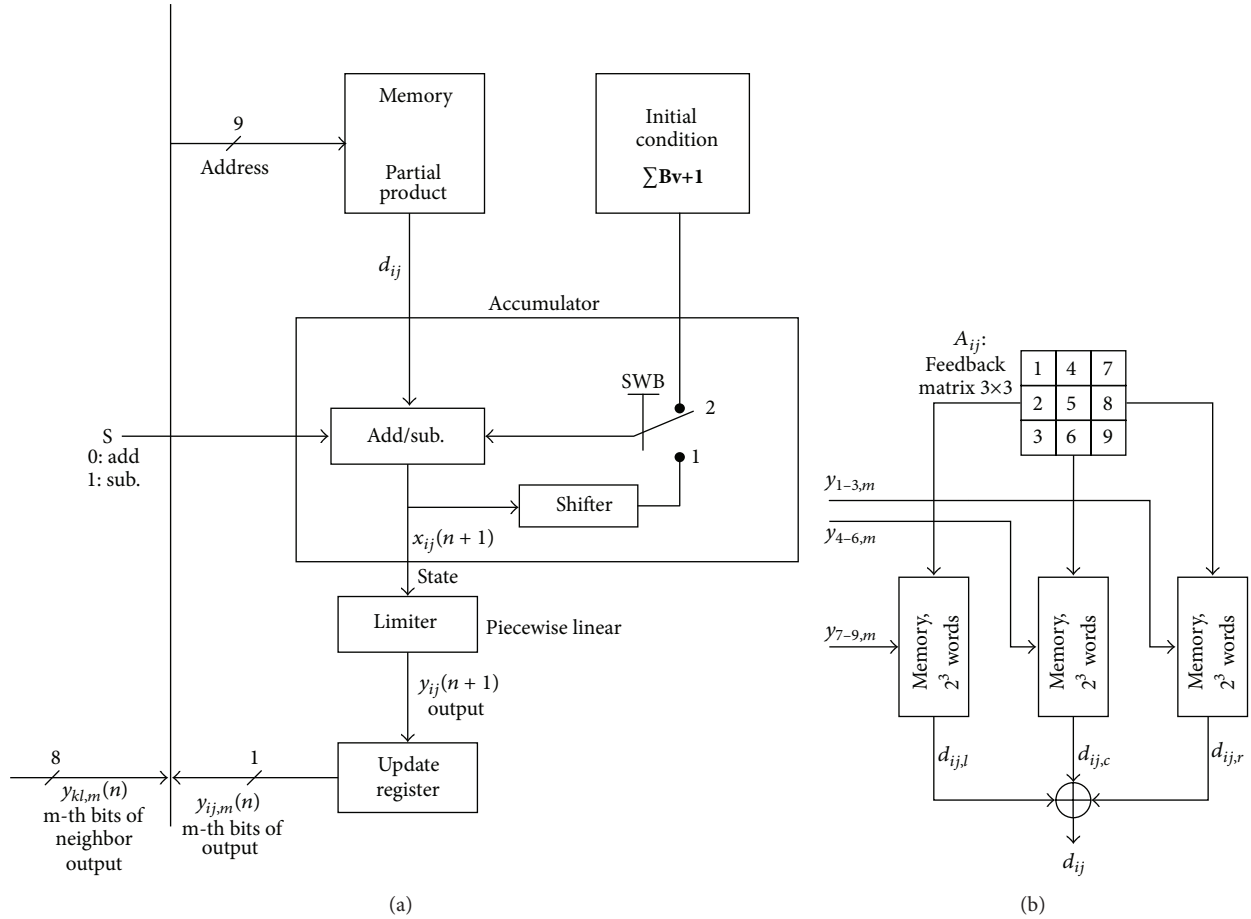


FIGURE 22: (a) Block diagram of DTCNN cell. (b) Memory partitioning scheme.

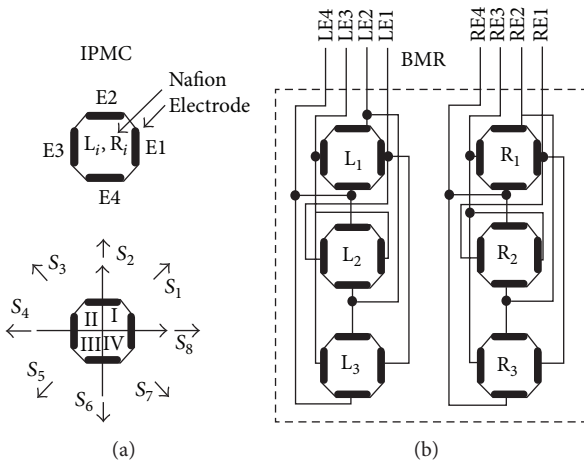


FIGURE 23: (a) Leg cross section with four electrodes in Cartesian coordinates. The states S_i generate bending moments and the associated direction movement. (b) BMR body hardware.

types of locomotion obtained with a stable checkerboard Turing pattern configuration (Figure 20(a)) [48]. Multitemplate approach (MTA) is an extension of the model used in RD-CNN-based hexapod robot. CPG implementation is based

on the principle that the same group of neural cells can be reorganized by changing the synaptic connection [49].

For implementation purposes, CNN can be classified as continuous-time (CT) [50] and discrete-time (DT) models [51]. CNN is composed of basic nonlinear dynamic circuits known as a cell, where each unit is connected only as a set of adjacent cell neighbors to form an array $M \times N$. In this way, the 3×3 checkerboard Turing pattern needs a 1-neighborhood (Figure 22(b)). The CNN structure can form in any dimensions, but, in our application, we need only two-dimensional arrays to reproduce autowaves for the tripod locomotion pattern.

An analogically programmable CNN in CMOS technology is reported with MOS transistor. This implementation is based on operational transconductance differential amplifier (OTA) stage. The cell resistor is approximated by the MOS transistor and its current-voltage relationship is nonlinear [52]. Moreover, digital architecture for the discrete-time CNN based on the combination of bit-serial computation of distributed arithmetic (DA) is presented. The system using DA has some advantages over all others: small memory size, shared memory contents, and reduced bus width. It can be implemented on an FPGA chip for reconfigurability, and a digital CMOS VLSI chip for high integration. The digital approach has the advantage of simplicity and expandability

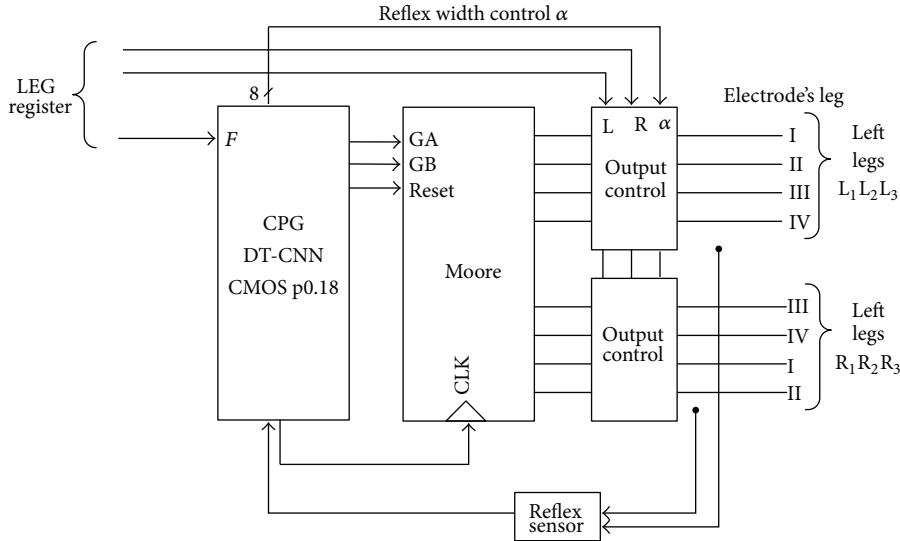


FIGURE 24: Hexapod walking system.

compared with the analog approaches, but the disadvantages of hardware complexity and bus width [53].

6. CMOS DT-CNN Implementation

The whole system has been designed on BMR as follows [54]. The proposed design is a simplified version of the CPG (Figure 21). This design corresponds to the fact that in most CPGs, the majority of interconnections between neurons are inhibitory [46]. The output saturation of the activation function corresponds to the maximum IPMC actuation (bending angle).

The CPG CNN structure shown in Figure 21 is built for the insect tripod gait. Each population of neurons is connected to a group of legs (A or B). Thus, the first one controls the first tripod ($L_1R_2L_3$) and the second controls the other tripod ($R_1L_2R_3$). This pair of mutually inhibited cells, with a suitable choice of the synaptic weights, is characterized by an antiphase synchronization of the activities of the two cells. The cells are implemented on FPGA using DA (Figure 22) with the architecture proposed in [54].

Each memory contains only the partial products for three coefficients. This configuration reduces storage by 95% in the direct implementation. The accumulator in DA performs add and shift operations.

7. Control System

The BMR body is the support for the current microlegs. The leg configuration on the body is an important consideration for driving the robot in any direction (Figure 23). In particular, the electrical configuration of the connections shown in Figure 23(b) of the legs is designed so as to produce a walking pattern. Experimental results show that the half-period of stance does not need any power consumption, while the other legs are in swing period (maximal current consumption). IPMC elasticity propels the BMR body. The

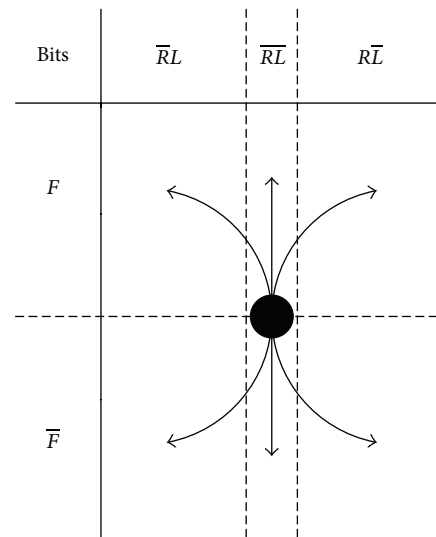


FIGURE 25: BMR possible direction control by PWM modulation.

bending angle decreases or increases the stance, and the swing time produces the BMR turn.

DT-CNN architecture for CPG has been included in the previous BMR control system to improve adaptability to this environment. The DT-CNN module controls the moore finite state machine (FSM) with GA and GB bits, the two tripod groups. DT-CNN has two inputs and five outputs. FSM is designed with eight states, and the output is controlled by the PWM as depicted in Figure 24. The MSB bits, R (right) and L (left), control the PWM width, while the ten bits, including LSB α bits, are proportional to the bending angle of the fiber IPMC actuator.

The BMR will move forward when R and L are set to zero. PWM width will be the same for the left and right legs as shown in Figure 25. In addition, it can turn the same way as an insect when the width of the PWM is changed for the left

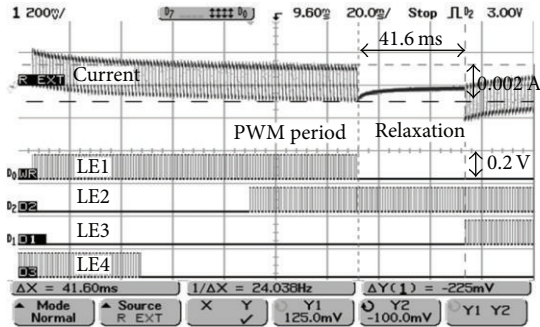


FIGURE 26: Applied PWM for LE1 to LE4 and current consumption for LE1 and LE3.

or right legs. Only three bits, stored in the microcontroller LEG register, are used to control the direction of the robot. Only these bits can be modified by user algorithms.

The overall system is coded as a driver in VHDL and is tested on FPGA. Currently, the PWM period is fixed in the PWM module. Experimental results show that a frequency of 763 Hz and 24 Hz for PWM and FSM, respectively, can drive one BMR leg. A half-period of stance is calculated at about 0.042 seconds (maximum bending to relaxation position). Figure 26 shows the FSM signal from the FPGA and current consumption with timing parameters. In future work, the module will be included in the microcontroller.

8. Conclusion

Microleg fabrication is an important challenge. It requires microscopic handling and specific instrumentation. Also, a failure in the procedure and a bad handling could damage the IPMC surface. Indeed, the distribution of the metal particles added on the IEM is very sensitive to the conditions of treatment, impregnation, and reduction. Microleg dimensions, according to the new manufacturing process worked out in this paper, make it possible to carry out a millimeter-size microrobot. Furthermore, the configuration of the electrodes confers 2,5 degrees of freedom. Thus, a hexapod robot will have 15 degrees of freedom unlike insects, which have at least 18 degrees of freedom. Using a micropump with a trust vector control improves maneuverability of the BMR.

Thereafter, several essential IPMC physical properties were given to drive 15 DOF hexapod BioMicroRobots. To measure these characteristics adequately, a very particular assembly was carried out. Inter alia, it was possible to show, without any doubt and using a laser vibrometer, that there is a linear relationship between the IPMC displacement rate and PWM report/ratio of cycle (duty cycle). It was also possible to measure the resonance frequency coupled with a heavy fluid. The minimum frequency for eliminating water electrolysis when the voltage is higher than the decomposition potential was also studied. The four methods for reducing water electrolysis explained in this paper are as follows:

- (1) Using alkyl ammonium like TBA allow decreasing electrolysis and the relaxation effect with the Nafion membrane;

- (2) keeping frequency higher than 30 Hz, the limit of molecule diffusion through the electrode membrane;
- (3) obtaining a high overpotential with better electrodes or keeping applied voltage lower than the decomposition potential;
- (4) using bipolar current source to control the charge density and charge balance injected inside IPMC. It may be done by active and passive waveforms for the two phases of asymmetrical biphasic stimuli.

The evidence of linearity between the PWM displacement rate and the PWM duty cycle is a relationship, which will be very important for controlling the BMR in all directions like an insect. Moreover, the electromechanical characteristics provided in this paper will allow developing a control method for each microleg. In effect, power consumption and leg degree of freedom numbers are two of the many restrictive characteristics to be observed at the time of system design for autonomous robots.

Obviously, other interesting applications can benefit from the process, which will be developed. It is possible to envisage active electrodes for the mechanical stimulation in human implant prostheses. Indeed, these electrodes could stimulate the sensitive receivers not only electrically, but also mechanically.

Lastly, a new artificial locomotion servo-system with discrete time cellular neural networks (DT-CNN) has been developed for a bioinspired hexapod BMR. Using a state machine and PWM modulation to drive the actuators, the robot can move in any direction similarly to an insect. An overview of the robot central pattern generator (CPG) in accordance with the insect displacement principle has been demonstrated. MTA is used to perform a particular locomotion type with autowave generation. The control system can be structured as a digital control system done by CNNs generating the tripod locomotion pattern. Leg displacement is controlled by CPG as a function of the reflex sensor and the user algorithm in the microcontroller.

Acknowledgments

This work was partly supported by Groupe d'acoustique et vibrations de l'Université de Sherbrooke (GAUS) and Institut des Matériaux et des Systèmes Intelligents (IMSI). The author would like to thank Pierre Magny and Irène Levesque for their advice and suggestions for taking SEM images of the composite. As well, The author would like to thank Magella Tremblay and Patrice Masson for the use of their laboratory instrumentations.

References

- [1] A. Bourjault and N. Chaillet, *La Microrobotique*, Hermes Sciences Publication, Paris, France, 2002.
- [2] K. E. Drexler, *Engines of Creation: The Coming Aera of Nanotechnology*, Anchor Press/Doubleday, Garden City, NY, USA, 1990.
- [3] A. Bonvilain and N. Chaillet, "Fabrication and experiment of microlegs for an insect-like microrobot," in *Microrobotics and*

- Microassembly III*, vol. 4568 of *Proceedings of SPIE*, pp. 163–174, Boston, Mass, USA, October 2001.
- [4] J. Enderle, S. Blanchard, and J. Bronzino, *Introduction to Biomedical Engineering*, Academic Press, San Diego, Calif, USA, 1999.
 - [5] S. Guo, L. Shi, N. Xiao, and K. Asaka, “A biomimetic underwater microrobot with multifunctional locomotion,” *Robotics and Autonomous Systems*, vol. 60, no. 12, pp. 1472–1483, 2012.
 - [6] K. K. Ahna, D. Q. Truong, D. N. C. Nam, J. I. Yoon, and S. Yokotac, “Position control of ionic polymer metal composite actuator using quantitative feedback theory,” *Sensors and Actuators A*, vol. 159, no. 2, pp. 204–212, 2010.
 - [7] L. Shi, S. Guo, and K. Asaka, “Modeling and experiments of IPMC actuators for the position precision of underwater legged microrobots,” in *Proceeding of the IEEE International Conference on Automation and Logistics*, pp. 420–425, Zhengzhou, China, August 2012.
 - [8] M. Vahabi, E. Mehdizadeh, M. Kabganian, and F. Barazandeh, “Modelling of a novel in-pipe microrobot design with IPMC legs,” *Proceedings of the Institution of Mechanical Engineers I*, vol. 225, no. 1, pp. 63–73, 2011.
 - [9] S. Martel, A. Saraswat, and I. Hunter, “Fundamentals of piezoceramic actuation for micrometer and sub-micrometer motions for the NanoWalker robot,” in *Microrobotics and Microassembly II*, vol. 4194 of *Proceedings of SPIE*, pp. 82–93, Boston, Mass, USA, November 2000.
 - [10] M. Otis, M. Jarry, R. Bernier, R. Fontaine, H. Ménard, and P. Masson, “3D Modelization of an hexapod BioMicroRobot propulsion system with IPMC actuators,” in *Proceeding of the ReSMiQ's 1st Northeast Workshop on Circuits and Systems (NEWCAS 2003)*, Montreal, Canada, June 2003.
 - [11] M. Otis, R. Bernier, Y. Pasco et al., “Development of an hexapod BioMicRorobot with nafion-Pt IPMC microlegs,” in *Proceedings of the 25th Annual International Conference of the IEEE Engineering in Medicine and Biology Society*, pp. 3423–3426, Cancun, Mexico, September 2003.
 - [12] K. Onishi, S. Sewa, K. Asaka, N. Fujiwara, and K. Oguro, “The effects of counter ions on characterization and performance of a solid polymer electrolyte actuator,” *Electrochimica Acta*, vol. 46, no. 8, pp. 1233–1241, 2001.
 - [13] K. Onishi, S. Sewa, K. Asaka, N. Fujiwara, and K. Oguro, “Morphology of electrodes and bending response of the polymer electrolyte actuator,” *Electrochimica Acta*, vol. 46, no. 5, pp. 737–743, 2000.
 - [14] M. Shahinpoor and K. J. Kim, “Effect of surface-electrode resistance on the performance of ionic polymer-metal composite (IPMC) artificial muscles,” *Smart Materials and Structures*, vol. 9, no. 4, pp. 543–551, 2000.
 - [15] Y. Bar-Cohen, *Electroactive Polymer (EAP) Actuators as Artificial Muscles, Reality, Potential, and Challenges*, SPIE Press, Washington, DC, USA, 2001.
 - [16] G. Xie and T. Okada, “Pumping effects in water movement accompanying cation transport across nafion 117 membranes,” *Electrochimica Acta*, vol. 41, no. 9, pp. 1569–1571, 1996.
 - [17] R. Kanno, S. Tadokoro, T. Takamori, and K. Oguro, “3-dimensional dynamic model of ionic conducting polymer gel film (ICPF) actuator,” in *Proceedings of the IEEE International Conference on Systems, Man and Cybernetics*, vol. 3, pp. 2179–2184, Beijing, China, October 1996.
 - [18] S. Guo, T. Nakamura, and T. Fukuda, “Micro active guide wire catheter system,” in *Proceedings of the IEEE International Conference on Industrial Technology (ICIT '96)*, pp. 517–521, Shanghai, China, December 1996.
 - [19] S. B. Brummer and M. J. Turner, “Electrical stimulation with Pt electrodes. II. Estimation of maximum surface redox (theoretical non-gassing) limits,” *IEEE Transactions on Biomedical Engineering*, vol. 24, no. 5, pp. 440–443, 1977.
 - [20] M. Shahinpoor and M. Mojarad, “Soft actuators and artificial muscles,” US patent 6109852, 2000.
 - [21] D. T. Sawyer, A. Sobkowiak, and J. L. Roberts, *Electrochemistry for Chemists*, John Wiley & Sons, New York, NY, USA, 2nd edition, 1995.
 - [22] X. Bao, Y. Bar-Cohen, and S. Lih, “Measurements and macro models of ionomeric polymer-metal composites (IPMC),” in *Smart Structures and Materials 2002: Electroactive Polymer Actuators and Devices (EAPAD)*, vol. 4695 of *Proceedings of SPIE*, pp. 220–227, San Diego, Calif, USA, March 2002.
 - [23] S. R. Taylor and E. Gileadi, “Physical interpretation of the Warburg impedance,” *Corrosion*, vol. 51, no. 9, pp. 664–671, 1995.
 - [24] M. Shahinpoor and K. J. Kim, “Ionic polymer-metal composites: I. Fundamentals,” *Smart Materials and Structures*, vol. 10, no. 4, pp. 819–833, 2001.
 - [25] Y. Bar-Cohen, S. Sherrit, and S. S. Lih, “Characterization of the electromechanical properties of EAP materials,” in *Smart Structures and Materials 2001: Electroactive Polymer Actuators and Devices*, vol. 4329 of *Proceedings of SPIE*, pp. 319–327, Newport Beach, Calif, USA, March 2001.
 - [26] M. Jarry, M. Otis, H. Semmaoui, G. Haché, and R. Fontaine, “Core Control Circuit for Submillimeterrobot,” in *Proceedings of the 25th Annual International Conference of the IEEE Engineering in Medicine and Biology Society*, pp. 3427–3430, Cancun, Mexico, September 2003.
 - [27] K. Mallavarapu and D. J. Leo, “Feedback control of the bending response of ionic polymer actuators,” *Journal of Intelligent Material Systems and Structures*, vol. 12, no. 3, pp. 143–155, 2001.
 - [28] D. J. Gorman, *Free Vibration Analysis of Beams and Shafts*, John Wiley & Sons, Toronto, Canada, 1995.
 - [29] R. J. Gilbert, *Vibration des structures—Interaction avec les fluides—Sources d'excitations aléatoires*, Éditions Eyrolles, Paris, France, 1998.
 - [30] S. Nemat-Nasser and Y. Wu, “Comparative experimental study of ionic polymer-metal composites with different backbone ionomers and in various cation forms,” *Journal of Applied Physics*, vol. 93, no. 9, pp. 5255–5267, 2003.
 - [31] S. Sewa, K. Onishi, K. Asaka, N. Fujiwara, and K. Oguro, “Polymer actuator driven by ion current at low voltage, applied to catheter system,” in *Proceedings of the IEEE 11th Annual International Workshop on Micro Electro Mechanical Systems (MEMS '98)*, pp. 148–153, Heidelberg, Germany, January 1998.
 - [32] N. Fujiwara, K. Asaka, Y. Nishimura, K. Oguro, and E. Torikai, “Preparation of gold-solid polymer electrolyte composites as electric stimuli-responsive materials,” *Chemistry of Materials*, vol. 12, no. 6, pp. 1750–1754, 2000.
 - [33] K. Asaka, N. Fujiwara, K. Oguro, K. Onishi, and S. Sewa, “State of water and ionic conductivity of solid polymer electrolyte membranes in relation to polymer actuators,” *Journal of Electroanalytical Chemistry*, vol. 505, no. 1-2, pp. 24–32, 2001.
 - [34] A. L. Rollet, G. Gebel, J. P. Simonin, and P. Turq, “A SANS determination of the influence of external conditions on the nanostructure of nafion membrane,” *Journal of Polymer Science B*, vol. 39, no. 5, pp. 548–558, 2001.

- [35] K. Oguro, N. Fujiwara, K. Asaka, K. Onishi, and S. Sewa, "Polymer electrolyte actuator with gold electrodes," in *Smart Structures and Materials 1999: Electroactive Polymer Actuators and Devices*, vol. 3669 of *Proceedings of SPIE*, pp. 64–71, Newport Beach, Calif, USA, March 1999.
- [36] J. G. Webster, *Medical Instrumentation Application and Design*, John Wiley & Sons, Toronto, Canada, 3rd edition, 1998.
- [37] S. B. Brummer and L. S. Robblee, "Criteria for selecting electrodes for electrical stimulation: theoretical and practical considerations," *Annals of the New York Academy of Sciences*, vol. 405, pp. 159–171, 1983.
- [38] J. M. Winter, *Biomechanics and Neural Control of Posture and Movement*, Springer, New York, NY, USA, 2000.
- [39] H. Cruse, T. Kindermann, M. Schumm, J. Dean, and J. Schmitz, "Walknet—a biologically inspired network to control six-legged walking," *Neural Networks*, vol. 11, no. 7-8, pp. 1435–1447, 1998.
- [40] P. Arena, H. Cruse, L. Fortuna, M. Frasca, and L. Patané, "A cellular nonlinear approach to decentralized locomotion control of the stick insect," in *Proceedings of the IEEE International Symposium on Circuits and Systems*, pp. IV-165–IV-168, May 2002.
- [41] H. Cruse, "What mechanisms coordinate leg movement in walking arthropods?" *Trends in Neurosciences*, vol. 13, no. 1, pp. 15–21, 1990.
- [42] J. Gray, *Animal Locomotion, Great Britain, London and Beccles*, edited by R. Carrington, The World Naturalist, 1968.
- [43] L. H. Ting, R. Blickhan, and R. J. Full, "Dynamic and static stability in hexapedal runners," *Journal of Experimental Biology*, vol. 197, pp. 251–269, 1994.
- [44] D. L. Jindrich and R. J. Full, "Many-legged maneuverability: dynamics of turning in hexapods," *Journal of Experimental Biology*, vol. 202, no. 12, pp. 1603–1623, 1999.
- [45] P. S. Stein, "Motor systems, with specific reference to the control of locomotion," *Annual Review of Neuroscience*, vol. 1, pp. 61–81, 1978.
- [46] K. G. Pearson, "Common principles of motor control in vertebrates and invertebrates," *Annual Review of Neuroscience*, vol. 16, pp. 265–297, 1993.
- [47] P. Arena and L. Fortuna, "Reaction-diffusion CNN algorithms to generate and control artificial locomotion," *IEEE Transactions on Circuits and Systems I*, vol. 46, no. 2, pp. 253–260, 1999.
- [48] P. Arena, L. Fortuna, and M. Branciforte, "Realization of a reaction-diffusion CNN algorithm for locomotion control in a hexapode robot," *Journal of VLSI Signal Processing Systems for Signal, Image, and Video Technology*, vol. 23, no. 2, pp. 267–280, 1999.
- [49] P. Arena, L. Fortuna, M. Frasca, and C. Marchese, "Multi-Template Approach to artificial locomotion control," in *Proceedings of the IEEE International Symposium on Circuits and Systems (ISCAS '01)*, vol. 2, pp. 37–40, May 2001.
- [50] L. O. Chua and L. Yang, "Cellular neural networks: theory," *IEEE Transactions on Circuits and Systems*, vol. 35, no. 10, pp. 1257–1272, 1988.
- [51] A. Rodriguez-Vazquez, S. Espejo, R. Dominguez-Castro, J. L. Huertas, and E. Sanchez-Sinencio, "Current-mode techniques for the implementation of continuous- and discrete-time cellular neural networks," *IEEE Transactions on Circuits and Systems II*, vol. 40, no. 3, pp. 132–146, 1993.
- [52] G. F. D. Betta, S. Graffi, Z. M. Kovacs, and G. Masetti, "CMOS implementation of an analogically programmable cellular neural network," *IEEE Transactions on Circuits and Systems II*, vol. 40, no. 3, pp. 206–215, 1993.
- [53] S. Park, J. Lim, and S. Chae, "Digital implementation of discrete-time cellular neural networks with distributed arithmetic," in *Proceedings of the IEEE International Conference on Neural Networks*, vol. 2, pp. 959–963, June 1997.
- [54] P. Arena, L. Fortuna, and M. Frasca, "Attitude control in walking hexapod robots: an analogic spatio-temporal approach," *International Journal of Circuit Theory and Applications*, vol. 30, no. 2-3, pp. 349–362, 2002.